Determination of Chargino and Neutralino Masses at the International Linear Collider

Yiming Li

Jesus College, University of Oxford

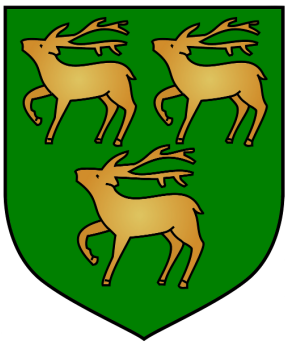

Thesis submitted in fulfilment of the requirements for the degree of Doctor of Philosophy at the University of Oxford

Hilary Term, 2011

Abstract

A feasibility study is presented which measures the masses of the chargino $\tilde{\chi}_1^{\pm}$ and neutralinos $\tilde{\chi}_1^0$ and $\tilde{\chi}_2^0$ using the processes of $e^+e^- \to \tilde{\chi}_1^+\tilde{\chi}_1^- \to \tilde{\chi}_1^0\tilde{\chi}_1^0 W^+W^-$ and $e^+e^- \to \tilde{\chi}_2^0\tilde{\chi}_2^0 \to \tilde{\chi}_1^0\tilde{\chi}_1^0 ZZ$ at the International Linear Collider. The detector simulation is based on the Silicon Detector (SiD) concept and an integrated luminosity of 500 fb^{-1} is considered at the centre-of-mass energy of 500 GeV. A template-fitting method is employed to measure the chargino and neutralino masses, which results in uncertainties of 0.16 GeV, 0.5 GeV and 1.0 GeV for the mass of $\tilde{\chi}_1^0$, $\tilde{\chi}_1^{\pm}$ and $\tilde{\chi}_2^0$ respectively.

A study on the ISIS2 sensor, a technology for the ILC vertex detector, is also presented. The characteristic of the sensors are studied for both its test structure and main array pixels. The operation conditions are optimized and the sensor successfully demonstrated its capabilities of in-situ charge storage and charge transfer. The charge transfer efficiency is measured to be better than 98%.

To the harmony of nature.

Acknowledgements

First of all I would like to thank my supervisor Andrei Nomerotski. He is the person who introduced me into the exciting field of particle physics. Without his guidance and invaluable patience, this thesis would not become possible.

I am also grateful to the LCFI collaboration and the SiD benchmarking group. I would like to thank Tim Barklow and Norman Graf from SLAC for generation of the Monte-Carlo data, and Jan Strube for his help in grid computing. Thanks to Chris Damerell, Zhige Zhang and Konstantin Stefanov for the inspiring and helpful discussions on the ISIS2 sensor testing. The technical support from engineers Jaya John John and Rui Gao are also much appreciated. Special thanks to Tomas Lastovicka, Erik Devetak, Ben Jeffery and Yambazi Banda, together with other lovely members from Oxford LCFI group, who generously shared their expertise and offered help whenever needed. I have always enjoyed the friendly (and sometimes alcoholic prone) atmosphere of the group.

I am indebted to the University of Oxford Clarendon Fund Scholarship and ORS Scholarship for their financial support throughout the three years of my D.Phil study.

I would like to thank the sub-department of Particle Physics. The lecture courses and skill training for the first year students were extremely useful. The support from the department staff have made the life here easier and more enjoyable.

In addition to the research life, the experience as a member of Jesus College has become a memorable part of my years in Oxford. I really appreciate the support from the college. The research allowance has enabled me to travel to summer schools and conferences. The college has also been a great place to meet academics from various backgrounds. Here I would like to thank my college advisor Philip Burrows (though not sure if I am allowed to mention an examiner) for the enjoyable evenings at college dinners.

Many thanks to my friends, including my fellow students in the department, friends from the Jesus College MCR, the Oxford University Japan Society, and the "Hot Sheep Group". They filled my life in Oxford with colour and laughters. Special thanks to Huo for his love and company despite the distance of eight time zones. Given that this thesis has been written under his consistent encouragement, his "conspiracy" to change my title to Mrs. before I get a doctor degree is forgiven. Finally I want to express my gratitude to my parents, for their constant love, support and understanding. Chinese philosopher Confucius once said: "Don't travel when your parents are still around; but if you do, travel in the right way." Hope the work presented here could show some of my footsteps in that right way.

Contents

List of Figures

List of Tables

Introduction

This thesis covers two studies on the International Linear Collider (ILC) physics based on the work the author has done in the past three years as a member of the LCFI and SiD collaboration. These studies consist of the measurement of the chargino and neutralino masses at the SiD detector and the testing of the ISIS2 sensor for the ILC vertex detector. This thesis starts with two introductory chapters, on the theoretical background and the ILC and SiD experiments. Two following chapters describe the ISIS2 study and the chargino and neutralino masses measurement, respectively. A more detailed structure is given as follows:

- Chapter 1 is a brief review of the theoretical background. A short reminder is given on the Standard Model (SM) and its problems. Supersymmetry is introduced as a most promising theoretical concept beyond the SM. The particle content of the minimal supersymmetric SM (MSSM) is described, where the charginos and neutralinos are mentioned. The mass matrix of the charginos and neutralinos and their production at an e^+e^- collider are discussed at the end of the chapter.

- Chapter 2 introduces the ILC and the SiD detector. Physics motivation of the ILC is briefly described before the description of the planned ILC accelerator. The SiD detector is introduced by individual subsystems.

- Chapter 3 describes the testing of the ISIS2 sensor. The chapter begins with a general introduction on the silicon detectors used in high energy physics. The principle of the In-situ Storage Imaging Sensor (ISIS) is introduced, in the context of the ILC vertex detector. Previous results on the first generation of ISIS sensor, ISIS1, are briefly re-

viewed. The design of the second generation, ISIS2 sensor, and the experimental set-up at the LCFI lab in Oxford are then described. The testing results of the ISIS2 include the studies of the test structure and main array. All the ISIS2 results presented here are the author's work except that specifically indicated. Part of the results are obtained with help of Rhorry Gauld (on the operation optimization) and Oxford M.Phys student Helena Wilding (on the CTE measurement with a shutter).

- Chapter 4 presents the measurements of the chargino ($\tilde{\chi}_1^{\pm}$) and neutralinos ($\tilde{\chi}_1^0$ and $\tilde{\chi}_2^0$) masses, using processes: $e^+e^- \to \tilde{\chi}_1^+\tilde{\chi}_1^- \to \tilde{\chi}_1^0\tilde{\chi}_1^0 W^+W^-$ and $e^+e^- \to \tilde{\chi}_2^0\tilde{\chi}_2^0 \to \tilde{\chi}_1^0\tilde{\chi}_1^0 ZZ$. The motivation of this analysis as one of the ILC benchmarking processes is discussed, and the simulation and reconstruction software used in this analysis (which is also common to the SiD) is introduced. The analysis strategies and results are described, consisting of the selection of $e^+e^- \to \tilde{\chi}_1^+\tilde{\chi}_1^-$ and $e^+e^- \to \tilde{\chi}_2^0\tilde{\chi}_2^0$ signals and the determination of the chargino and neutralino masses using template fitting method. All the results are solely the author's work, while the feasibility study of the template fitting method using toy Monte-Carlo is done with the help of Erik Devetak.

- Chapter 5 summarizes the results of the studies presented in the thesis.

Chapter 1

Theoretical Background

This chapter gives a brief description to the Standard Model and its challenges, and then introduces Supersymmetry as the most promising theory beyond SM. The mass spectrum of charginos and neutralinos, and their production at an e^+e^- collider is discussed in some detail.

1.1 Standard Model

The Standard Model (SM) is a theory summarizing our current knowledge of the fundamental constituents of matter and their interactions. It has been successfully tested to a high precision by a large number of experiments in the last decades. The SM is a gauge invariant quantum field theory based on the symmetry group $SU(3) \times SU(2) \times U(1)$ where $SU(3)$ corresponds to the strong interaction and $SU(2) \times U(1)$ corresponds to the electroweak interaction spontaneously broken by the Higgs mechanism.

1.1.1 Introduction to the SM

In the relativistic quantum field theory, particles are represented by field operators on particle states, with creation and annihilation operators for particles and antiparticles respectively. Spin $\frac{1}{2}$ particles are called fermions, described by spinor fields. The fermionic particle content of the SM is shown in Table 1.1. There are three generations of quarks and leptons, which interact with each other via the electromagnetic interaction, weak interaction and strong

Group	Particles	Charge (e^-)	Spin	I_3	Y
Leptons	$\begin{pmatrix} \nu_e \\ e \end{pmatrix}_L \begin{pmatrix} \nu_\mu \\ \mu \end{pmatrix}_L \begin{pmatrix} \nu_\tau \\ \tau \end{pmatrix}_L$	0	$\frac{1}{2}$	$\frac{1}{2}$	-1
		-1	$\frac{1}{2}$	$-\frac{1}{2}$	-1
	$e_R \ \ \mu_R \ \ \tau_R$	-1	$\frac{1}{2}$	0	-2
Quarks	$\begin{pmatrix} u \\ d' \end{pmatrix}_{L,i} \begin{pmatrix} c \\ s' \end{pmatrix}_{L,i} \begin{pmatrix} t \\ b' \end{pmatrix}_{L,i}$	$\frac{2}{3}$	$\frac{1}{2}$	$\frac{1}{2}$	$\frac{1}{3}$
		$-\frac{1}{3}$	$\frac{1}{2}$	$-\frac{1}{2}$	$\frac{1}{3}$
	$u_{R,i} \ \ c_{R,i} \ \ t_{R,i}$	$\frac{2}{3}$	$\frac{1}{2}$	0	$\frac{4}{3}$
	$d'_{R,i} \ \ s'_{R,i} \ \ b'_{R,i}$	$-\frac{1}{3}$	$\frac{1}{2}$	0	$-\frac{2}{3}$

Table 1.1: Fermionic particle content of the Standard Model. I_3 is the weak isospin and Y is hypercharge. The subscript i runs from 0 to 2 to represent the color. The superscript $'$ denotes the gauge eigenstates for the down-type quarks. Their mass eigenstates are obtained by mixing via the CKM matrix, see text.

Coupling	Particle	Charge (e^-)	Spin	Mass (GeV)
Electromagnetic	γ	0	1	0
Weak	W^+	$+1$	1	80.399 ± 0.023
	W^-	-1	1	80.399 ± 0.023
	Z	0	1	91.1876 ± 0.0021
Strong	g ($\times 8$)	0	1	0
	H	0	0	> 114.4

Table 1.2: Bosonic particle content of the Standard Model. The masses are quoted as in [1].

interaction. The electromagnetic interaction is exclusive for charged particles and the strong interaction is exclusive for quarks. Spin 1 particles are described by vector fields representing the gauge bosons that mediate all the interactions mentioned above. There is also a spin 0 boson in the SM, the Higgs boson, which leads to the spontaneous electroweak symmetry breaking and gives masses to SM particles. The bosonic particle content of the SM is shown in Table 1.2.

The electromagnetic interactions between charged particles can be described by quantum electrodynamics (QED), a local gauge invariant theory based on an Abelian $U(1)$ group. Under a local gauge transformation

$$\psi(x) \to e^{i\theta(x)}\psi(x) \tag{1.1}$$

a covariant derivative should be introduced to assure that the system Lagrangian is unchanged:

$$D_\mu = \partial_\mu + ieA_\mu \tag{1.2}$$

where the subscript $_\mu$ is the Lorentz index running from 0 to 3, e is the electrical charge of the particle and the gauge field A_μ is transformed as

$$A_\mu \rightarrow A_\mu + \partial_\mu \theta(x). \tag{1.3}$$

After the transformation the new Lagrangian therefore becomes:

$$\mathcal{L}_{QED} = i\bar{\psi}\gamma^\mu\partial_\mu\psi - m\bar{\psi}\psi - \frac{1}{4}F_{\mu\nu}F^{\mu\nu} - e\bar{\psi}\gamma_\mu A^\mu\psi, \tag{1.4}$$

where $F_{\mu\nu}$ is defined as

$$F_{\mu\nu} = \partial_\mu A_\nu - \partial_\nu A_\mu. \tag{1.5}$$

The first two terms of Equation 1.4 ($i\bar{\psi}\gamma^\mu\partial_\mu\psi - m\bar{\psi}\psi$) form the Lagrangian for a free charged particle with mass m. Here it can be seen that the field A^μ is interpreted as the photon field and the last term of Equation 1.4 describes the coupling of the electromagnetic current $j^\mu = e\bar{\psi}\gamma^\mu\psi$ to the photon field. Gauge invariance implies the conservation of the electromagnetic current, hence conservation of the charge. The $-\frac{1}{4}F_{\mu\nu}F^{\mu\nu}$ term is the Lagrangian of a free photon. Note that there is no mass term for the photon field, otherwise the $\mathcal{L}_{QED}$ cannot remain the same under gauge transformation. This agrees well with the experimental fact for a massless photon.

The $U(1)$ symmetry can be extended to non-Abelian symmetries. Quantum chromodynamics (QCD) describing the strong interactions between quarks is based on a non-Abelian $SU(3)$ group. The $SU(3)$ group has 8 generators corresponding to 8 gluons and similar to the charge in QED, there are 3 conserved "colour charges".

The weak interaction and electromagnetic interaction are unified by the electroweak theory[2][3] with a $SU(2)_L \times U(1)_Y$ group. $SU(2)_L$ corresponds to the quantum number

of weak isospin and $U(1)_Y$ to the quantum number of the hypercharge. The fermion fields are decomposed into chiral left and right components except for neutrinos that are purely left-handed. The $SU(2)_L$ isospin group only acts on the left-handed chiral states. In other words, the fermions form left-handed weak isodoublets and right-handed isosinglets. Three gauge fields $(W^1_\mu, W^2_\mu, W^3_\mu)$ are introduced by the $SU(2)_L$ gauge transformations while one gauge field B^μ is associated to the $U(1)_Y$ transformation. A linear combination of W^1 and W^2 forms the $W^\pm$ bosons which is responsible for mediating the charge current weak interactions. Similarly the photon field A and neutral boson Z can be formed from a linear combination of W^3 and B, with the weak mixing angle θ_W.

So far in this discussion the $W^\pm$ and Z bosons are still massless as are the photons, which contradicts the experimental observations. To introduce mass to the theory, the $SU(2)_L \times U(1)_Y$ symmetry is spontaneously broken, while leaving the electromagnetic $U(1)_{EM}$ symmetry unbroken, by introducing an isospin doublet of complex scalar Higgs field. The Higgs field self-interaction is described by a Higgs potential which has a non-zero vacuum expectation value. The kinematic term of the Higgs field will give rise to the mass of $W^\pm$ and Z bosons. By properly choosing the gauge, the Higgs field corresponds to a real Higgs boson, which remains the last component of the SM yet to be discovered in experiments. Direct search at LEP established a lower bound of 114.4 GeV[1] at the 95% confidence level[4].

The Higgs boson also generates masses for fermions via the Yukawa couplings between the Higgs field and the fermion fields. Flavour changing interactions via $W^\pm$ bosons have been observed in experiments, indicating that in the quark sector the flavour and mass eigenstates are not the same. The flavour mixing between three generations is described by the Cabbibo-Kobayashi-Maskawa (CKM) matrix[5][6]. The terms in the SM describing Yukawa couplings with the Higgs field are:

$$\mathcal{L}_Y = -Y^d_{ij}\bar{Q}^i_L \Phi d^j_R - Y^u_{ij}\bar{Q}^i_L \Phi^c u^j_R + h.c. \tag{1.6}$$

[1]Natural units are used for energy and mass throughout this thesis. For example, 1 GeV is equivalent to 1 GeV/c^2 in SI units.

where $Y^{u,d}$ are 3×3 complex matrices, Φ is the Higgs field, $\Phi^c = i\sigma_2\Phi$ is the charge conjugate of the Higgs field, $\bar{Q}_L$ are the left-handed quark doublets, u_R and d_R are the right-handed up- and down-type quark singlets respectively, the subscripts i, j are the generation indices, and "*h.c.*" stands for the hermitian conjugation of the previous term. The mass terms can be generated when Φ acquires a vacuum expectation value $\langle\Phi\rangle = (0, v/\sqrt{2})$. The physical states of quarks, namely the mass eigenstates are obtained by diagonalizing $Y^{u,d}$ with four unitary matrices $V_{L,R}^{u,d}$:

$$M_{diag}^{q} = \frac{v}{\sqrt{2}} V_L^q Y^q V_R^{q\dagger},\ q = u, d. \tag{1.7}$$

When the mass eigenstates couple to the $W^{\pm}$ boson, the couplings are given by

$$V_{CKM} \equiv V_L^u V_L^{d\dagger} \tag{1.8}$$

which is defined as the CKM matrix. The CKM matrix is a 3×3 unitary matrix, parameterized by three mixing angles and a CP-violating complex phase [6].

1.1.2 Problems of the SM

Although the SM has had great success in explaining and predicting experimental phenomena, there are certain problems it is confronted with, an obvious one being that the SM does not describe the gravitational interaction. Gravity is negligible at the scale currently accessible by experiments, but becomes important at the Planck scale. Any Grand Unified Theory (GUT) requires that all gauge couplings become unified at the Planck scale. The three gauge couplings of the SM are not the same, nor is there any tendency for gauge coupling unification at the Planck scale.

Another serious problem of the SM is the Hierarchy problem or fine tuning problem [7][8][9]. As introduced in the previous section, the Higgs is associated with electroweak symmetry breaking, therefore its mass m should be in the electroweak energy range $m_H \sim \mathcal{O}(100\text{GeV})$. On the other hand, the radiative corrections of the Higgs mass are quadratically divergent with respect to the cutoff scale Λ_{UV}. For example, the loop correction to Higgs

mass from a fermion f is shown in Figure 1.1. This contribution can be evaluated as:

$$\Delta m_H^2 = -\frac{\lambda_f^2}{8\pi^2}(\Lambda_{UV}^2 - 2m_f^2 \ln(\Lambda_{UV}/m_f) + ...), \tag{1.9}$$

where λ_f is the coupling constant, and Λ_{UV} is the ultraviolet cutoff. The fermion f can be any SM lepton or quark, and for quarks the correction above should multiply a color factor of 3. The most important contribution is from the top quark with $\lambda_f \sim 1$. If the cutoff scale is close to the Planck scale, with $\Lambda_{UV} \sim 10^{16}$ GeV, the Higgs bare mass has to be fine tuned to a precision of $m_H^2/\Lambda_{UV}^2 \sim 10^{-28}$ to make sure the actual Higgs mass is at the electroweak scale.

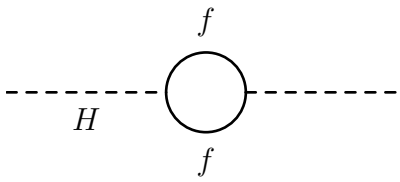

Figure 1.1: Loop corrections to m_H^2 from a fermion f, with mass m_f.

It has been widely accepted that a large portion of the mass in the universe is not directly visible[1]. Indirect observations of this so-called dark matter are made, for example in galaxy rotation curves[10] and gravitational lensing[11][12]. The SM fails to provide a viable particle candidate for cold dark matter, which should be non-relativistic, weakly interacting stable particles.

Another cosmological challenge for the SM is the baryon asymmetry of the universe. CP-violation should be present to explain the overwhelming excess of matter over anti-matter, yet the CP-violating phase in the CKM matrix is too small to give rise to such an asymmetry.

All these issues above represent a serious challenge and indicate that there must be some new physics beyond the SM.

1.2 Supersymmetry

The problems of the SM can be potentially solved by introducing a new symmetry - Supersymmetry (SUSY) between fermions and bosons[13][14]. In a SUSY theory, every fermionic particle has a bosonic superpartner, with all properties the same except the spin differs by $\frac{1}{2}$, and all bosons have such fermionic superpartners.

Introduction of superpartners solves the hierarchy problem naturally because the quadratic divergence contribution of Higgs self energy corrections from heavy quarks (mainly top quark) is canceled out by the contribution from the superpartners. For the example given in Figure 1.1, the loop correction to m_H^2 from a scalar particle S, superpartner of f, is shown in Figure 1.2. The contribution is estimated to be:

$$\Delta m_H^2 = \frac{\lambda_S}{16\pi^2}(\Lambda_{UV}^2 - 2m_S^2 \ln(\Lambda_{UV}/m_S) + ...), \tag{1.10}$$

where m_S is the mass of S, λ_S is the coupling constant. For different chirality states of a fermion, different scalar superpartners are required. Therefore each SM fermion has two superpartners corresponding to left- and right-handed states. Comparing Equation 1.10 to Equation 1.9, if we set:

$$\lambda_S = \lambda_f^2, \tag{1.11}$$

the quadratic divergence term of Higgs mass for fermions and their superpartners will cancel each other.

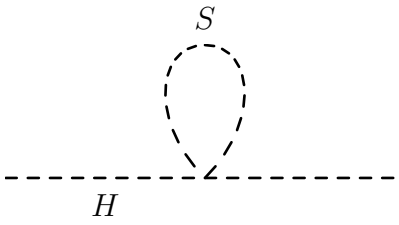

Figure 1.2: Loop corrections to m_H^2 from a scalar S, with mass m_S.

SUSY also offers a solution for the dark matter problem. If R-parity is imposed (definition

of R-parity will be given later), there must be a stable Lightest SUSY Particle (LSP). If the LSP is neutral, it would interact only weakly and could therefore be a good candidate for cold dark matter[15].

Exact SUSY requires that the SM particles have superpartners of the same masses, which obviously contradicts experimental results since no superpartners of the SM particles have been observed. Therefore SUSY must be broken in nature. At the electroweak energy scale, SUSY can be broken "softly" by explicitly adding breaking terms in the Lagrangian. Such low-energy models include the Minimal Supersymmetric extension of the Standard Model (MSSM)[16][17] and Constrained MSSM (CMSSM)[18]. The field content of the MSSM is introduced in the following section.

Various models have been constructed to explain how SUSY is spontaneously broken at the Planck scale and, if spontaneous SUSY breaking happens in the hidden sector[2], how these effects are mediated with the SM sector. One example of such models is Minimum SUperGRAvity (mSUGRA[19][20][21]), where gravity is the messenger transmitting the SUSY breaking of the hidden sector to the MSSM. In mSUGRA, a common scalar mass m_0, a common gaugino mass $m_{1/2}$ and a common soft trilinear SUSY breaking parameter A_0 are assumed at the GUT scale. Two additional parameters are assumed, namely the ratio of the two Higgs field vacuum expectation values at electroweak scale $\tan\beta$ ($\langle H_u^0\rangle/\langle H_d^0\rangle$) and the sign of the Higgsino mass term sgnμ. Various parameters are evolved from the GUT scale to the electroweak scale using the Renormalization Group Equations (RGEs) [22][23]. For the analysis presented in this thesis, we consider one of the models with non-universal soft SUSY breaking contributions to the Higgs masses (NUHM)[24]. The NUHM is similar to the mSUGRA in definition of the parameters, but it allows the soft breaking Higgs masses to differ from m_0 at the GUT scale.

[2]A hidden sector consists of particles that are neutral to the SM gauge groups.

Super-multiplets	Boson fields	Fermion fields	$SU(3)$	$SU(2)$	$U(1)$
gluon/gluino	g	$\tilde{g}$	8	1	0
gauge/	$W^{\pm}, W^0$	$\tilde{W}^{\pm}, \tilde{W}^0$	1	3	0
gaugino	B	$\tilde{B}$	1	1	0
slepton/	$(\tilde{\nu}_e, \tilde{e}^-)_L$	$(\nu_e, e^-)_L$	1	2	-1
lepton	$\tilde{e}_R$	e_R	1	1	-2
squarks/	$(\tilde{u}_L, \tilde{d}_L)$	$(u, d)_L$	3	2	1/3
quark	$\tilde{u}_R$	u_R	3	2	4/3
	$\tilde{d}_R$	d_R	3	2	$-2/3$
Higgs/	(H_d^0, H_d^-)	$(\tilde{H}_d^0, \tilde{H}_d^-)$	1	2	-1
higgsino	(H_u^+, H_u^0)	$(\tilde{H}_u^+, \tilde{H}_u^0)$	1	2	1

Table 1.3: The fields of the MSSM and their $SU(3) \times SU(2) \times U(1)$ quantum numbers. Only one generation of quarks and leptons are shown and anti-particles are not shown.

1.2.1 Particle Content of MSSM

The MSSM is the supersymmetric extension of the SM with the minimum particle content. The $SU(3) \times SU(2) \times U(1)$ gauge groups remain the same. Every SM particles has a superpartner with the same quantum numbers except with the spin different by 1/2. The Higgs sector is extended to two Higgs doublets.

The left- and right-handed states of SM fermions transform differently under the $SU(2)$ gauge, therefore two different superpartners $\tilde{f}_L$ and $\tilde{f}_R$ should be present for each SM fermion f, with the exception of neutrinos which only exist in left-handed states in the SM. The superpartners of leptons and quarks are called sleptons and squarks, respectively. For gauge bosons, the gluons have their fermionic superpartners called gluinos, and the $SU(2) \times U(1)$ gauge bosons have gauginos as their fermionic superpartners, namely the Bino and Winos. The extended Higgs sectors have two doublets with hypercharge ± 1 to generate masses for up-type quarks and down-type quarks (and charged leptons) respectively. The two doublets are also needed to cancel anomalies when higgsinos, the superpartners of the Higgs, are introduced. The field content of the MSSM described above is summarized in Table 1.3.

The gauge eigenstates introduced above can mix with each other and form mass eigenstates. Charged gauginos (Winos) and higgsinos are allowed to mix together to form four

Names	Spin	P_R	Gauge Eigenstates	Mass Eigenstates
Higgs bosons	0	$+1$	$H_u^0\ H_d^0\ H_u^+\ H_d^-$	$h^0\ H^0\ A^0\ H^\pm$ †
squarks	0	-1	$\tilde{u}_L\ \tilde{u}_R\ \tilde{d}_L\ \tilde{d}_R$ $\tilde{s}_L\ \tilde{s}_R\ \tilde{c}_L\ \tilde{c}_R$ $\tilde{t}_L\ \tilde{t}_R\ \tilde{b}_L\ \tilde{b}_R$	$\tilde{u}_L\ \tilde{u}_R\ \tilde{d}_L\ \tilde{d}_R$ $\tilde{s}_L\ \tilde{s}_R\ \tilde{c}_L\ \tilde{c}_R$ $\tilde{t}_1\ \tilde{t}_2\ \tilde{b}_1\ \tilde{b}_2$
sleptons	0	-1	$\tilde{e}_L\ \tilde{e}_R\ \tilde{\nu}_e$ $\tilde{\mu}_L\ \tilde{\mu}_R\ \tilde{\nu}_\mu$ $\tilde{\tau}_L\ \tilde{\tau}_R\ \tilde{\nu}_\tau$	$\tilde{e}_L\ \tilde{e}_R\ \tilde{\nu}_e$ $\tilde{\mu}_L\ \tilde{\mu}_R\ \tilde{\nu}_\mu$ $\tilde{\tau}_1\ \tilde{\tau}_2\ \tilde{\nu}_\tau$
neutralinos	$\frac{1}{2}$	-1	$\tilde{B}^0\ \tilde{W}^0\ \tilde{H}_u^0\ \tilde{H}_d^0$	$\tilde{\chi}_1^0\ \tilde{\chi}_2^0\ \tilde{\chi}_3^0\ \tilde{\chi}_4^0$
charginos	$\frac{1}{2}$	-1	$\tilde{W}^\pm\ \tilde{H}_u^+\ \tilde{H}_d^-$	$\tilde{\chi}_1^\pm\ \tilde{\chi}_2^\pm$
gluino	$\frac{1}{2}$	-1	$\tilde{g}$	$\tilde{g}$

Table 1.4: The undiscovered particles in the MSSM (assuming sfermion mixing for the first two families is negligible). † Two Higgs doublets are required in the MSSM while five physical Higgs particles are left after the spontaneous breaking of the electroweak symmetry.

fermions called charginos. Similarly, neutral gauginos (photino and Zino) and neutral higgsinos mix to form four neutralinos. For squarks and sleptons, f_L and f_R mixing are also possible. A summary of gauge and mass eigenstates of undiscovered particles in the MSSM is given in Table 1.4.

The MSSM implies an R-parity invariance, and R-parity P_R is defined as:

$$P_R = (-1)^{3(B-L)+2S} \tag{1.12}$$

where B is the baryon number, L is the lepton number, and S is the particle spin. All SM particles are R-parity even ($P_R = +1$) and all superpartners are R-parity odd ($P_R = -1$). The MSSM required conservation of R-parity, which has important influence on SUSY phenomenology. For instance, from initial states of even R-parity, superpartners can only be produced in pairs. Another impact is that in the decay product of a supersymmetric particle, there must be a lighter supersymmetric particle. Therefore a Lightest Supersymmetric Particle (LSP) should exist, and the LSP is stable since R-parity invariance allows no mixing between SM particles and SUSY particles. The LSP is likely to be electrically neutral and colorless given by cosmological constraints[25], which made it a promising candidate for the

dark matter[15].

1.2.2 Neutralino and Chargino Masses

The neutral gauginos and higgsinos can mix to form four neutralinos. Their mass term of the Lagrangian given in the basis of $\psi^0 = (\tilde{B}, \tilde{W}^3, \tilde{H}_d^0, \tilde{H}_u^0)$ is:

$$\mathcal{L}_{\tilde{\chi}^0} = -\frac{1}{2}(\psi^0)^T \mathcal{M}_N \psi^0 + h.c. \tag{1.13}$$

where the mass matrix for neutralinos $\mathcal{M}_N$ is

$$\mathcal{M}_N = \begin{pmatrix} M_1 & 0 & -m_Z \sin\theta_W \cos\beta & m_Z \sin\theta_W \sin\beta \\ 0 & M_2 & m_Z \cos\theta_W \cos\beta & -m_Z \cos\theta_W \sin\beta \\ -m_Z \sin\theta_W \cos\beta & m_Z \cos\theta_W \cos\beta & 0 & -\mu \\ m_Z \sin\theta_W \sin\beta & -m_Z \cos\theta_W \sin\beta & -\mu & 0 \end{pmatrix}, \tag{1.14}$$

where M_1 and M_2 stands for the bino and wino mass respectively, θ_W is the Weinberg angle (weak mixing angle) and $-\mu$ comes from the higgsino mass terms. The mass matrix can be diagonalized to get the four mass eigenstates $\tilde{\chi}_1^0$, $\tilde{\chi}_2^0$, $\tilde{\chi}_3^0$ and $\tilde{\chi}_4^0$ (with increasing mass). The properties of neutralinos depend on the field content of the resulting eigenstates. If $|M_{1,2}| < \mu$, the lighter $\tilde{\chi}_1^0$ and $\tilde{\chi}_2^0$ are gaugino like and two heavier ones are higgsino like. For certain choice of parameters, the lightest neutralino $\tilde{\chi}_1^0$ is likely to be the LSP.

Some models (such as mSUGRA) assumes a unified gaugino mass $m_{1/2}$ at the GUT scale, then it can be predicted that [14]:

$$M_1 \approx \frac{5}{3}\tan^2\theta_W M_2 \approx \frac{1}{2}M_2 \tag{1.15}$$

at the electroweak scale. If the electroweak symmetry breaking effects can be viewed as a

perturbation in the neutralino mass matrix, namely,

$$m_Z \ll |\mu \pm M_{1,2}|, \tag{1.16}$$

then the lightest neutralino $\tilde{\chi}_1^0$ is mainly bino-like ($\tilde{\chi}_1^0 \approx \tilde{B}$), and $\tilde{\chi}_2^0$ is mainly wino-like ($\tilde{\chi}_2^0 \approx \tilde{W}$). A straight-forward prediction resulting is that the mass of $\tilde{\chi}_1^0$ is roughly half of that of $\tilde{\chi}_2^0$.

Similar to the neutralinos, four charginos can be formed from combination of two winos $\tilde{W}^{\pm}$ and two charged higgsinos $\tilde{H}^{\pm}$. The chargino mass term of the Lagrangian is given as

$$\mathcal{L}_{\tilde{\chi}^{\pm}} = -\frac{1}{2}(\psi^+, \psi^-) \begin{pmatrix} 0 & \mathcal{M}_C^T \\ \mathcal{M}_C & 0 \end{pmatrix} \begin{pmatrix} \psi^+ \\ \psi^- \end{pmatrix} + h.c. \tag{1.17}$$

in the basis $\psi^+ = (-i\tilde{W}^+, \tilde{H}_u^+)$, where the mass matrix is

$$\mathcal{M}_C = \begin{pmatrix} M_2 & \sqrt{2} m_W \cos\beta \\ \sqrt{2} m_W \sin\beta & \mu \end{pmatrix} \tag{1.18}$$

After diagonalization of the mass matrix two mass eigenstates of $\tilde{\chi}_1^{\pm}$ and $\tilde{\chi}_2^{\pm}$ are obtained, with the latter being the heavier one. If $M_2 < \mu$ the lighter chargino $\tilde{\chi}_1^{\pm}$ is mainly wino like and the $\tilde{\chi}_2^{\pm}$ is higgsino like.

Again, if we assume that $M_2 < |\mu|$ and the electroweak symmetry breaking can be treated as a perturbation (Equation 1.16), then the mass of $\tilde{\chi}_1^{\pm}$ is almost degenerate with the mass of $\tilde{\chi}_2^0$. The higgsino-like $\tilde{\chi}_2^{\pm}$, $\tilde{\chi}_3^0$ and $\tilde{\chi}_4^0$ have masses of the order of $|\mu|$. In the processes studied in Chapter 4, the chargino and neutralino mass parameters[24][26] exhibit such properties.

1.2.3 Chargino and Neutralino pair production at an e^+e^- Collider

At e^+e^- colliders both charginos and neutralinos can be produced in pairs through the s-channel and t-channel. Models of their production have been widely studied [27][28][29][30].

The tree level Feynman diagrams of $\tilde{\chi}_1^{\pm}$ and $\tilde{\chi}_2^0$ pair production (which is studied in this thesis) are shown in Figure 1.3 and Figure 1.4 respectively. The t-channels are significant only if the exchanged sneutrino or slepton is not too heavy. The cross-sections are also dependent on the beam polarization. For example, if the charginos are wino-like, they only couple to the $SU(2)$ gauge boson W^3 component of the γ-Z linear combination. For right-handed electron beams, the s-channel diagram in Figure 1.3 is suppressed because right-handed electrons are weak isospin singlets and they only couple to the $U(1)$ gauge boson B of the γ-Z combination.

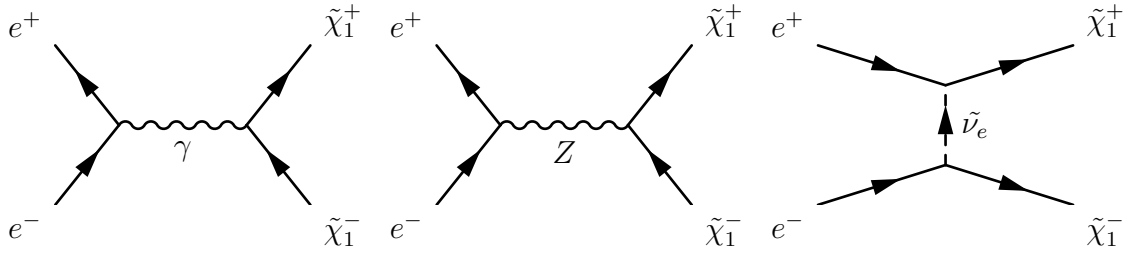

Figure 1.3: Feynman Diagrams of chargino pair production at tree level.

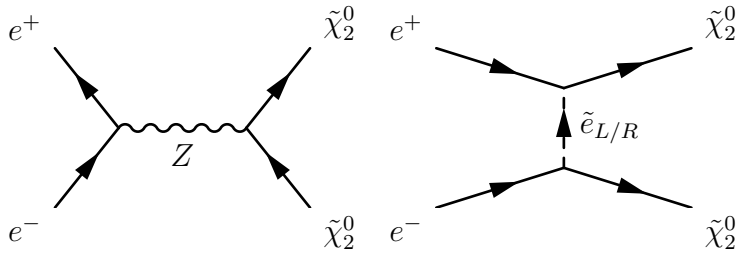

Figure 1.4: Feynman Diagrams of neutralino pair production at tree level.

The observation of these processes at e^+e^- colliders depends on the decay products of the charginos and neutralinos, which is in turn determined by the parameters of the SUSY model and their masses. A study of one of the points in the SUSY parameter space will be presented in Chapter 4, while a general summary of other possibilities can be found in [31].

Chapter 2

ILC and SiD

2.1 International Linear Collider

Historically the understanding of particle physics deepens with the increase of the energy of accelerators. The Large Hadron Collider (LHC)[32] is the largest accelerator ever built with the energy reaching 3.5 TeV per beam. It took advantage of the existing tunnel which was used by Large Electron Position collider (LEP)[33], the most energetic lepton collider so far, which performed a lot of important measurements such as precision measurement of W and Z boson properties. Both of these machines are circular accelerators (synchrotrons), with the obvious advantage of accelerating particles in a more economical way over linear accelerators. In other words they are capable of accelerating particles to a higher energy given the same length (circumference). In reality the synchrotron radiation comes to play a rather important role at high energies. The radiated power is inversely proportional to the fourth power of the mass of charged particles ($P \propto m^{-4}$), so due to the difference of three orders of magnitude, the electrons suffer much higher loss at high energies comparing to protons. Therefore a linear collider becomes necessary for an e^+e^- collider beyond certain energy scale.

2.1.1 Physics Motivation

Since early 2010 the LHC has been accumulating data, and this will be the first look at the physics at the Terascale. While the LHC is about to make exciting discoveries, the ILC, a proposed future lepton collider could complement the LHC studies to answer some fundamental questions in particle physics.

The most promising discovery expected from the LHC is the Higgs boson. Responsible for the spontaneous symmetry breaking and generation of masses, the Higgs mechanism remains the last piece of the Standard Model to be identified by experiments. If there is a SM Higgs it should be found at the LHC and its mass could be measured by the ATLAS and CMS experiments. More detailed study of Higgs properties, however, is only possible with a lepton collider, including the measurements of the Higgs spin, parity, its coupling to gauge bosons and Higgs self-coupling. The ILC will also measure the mass, width and branching ratios substantially more accurately [34]. If there are Higgs multiplets rather than a SM Higgs, for example the four Higgses as in MSSM, they will be detected and studied at the ILC if they are within the energy range. The precision measurement of their mass, spin and couplings would confirm whether they are consistent with the MSSM scenario. It is also possible that no Higgs is seen at all at the LHC, in which case the ILC could study the top quark properties, its Yukawa coupling, and gauge boson scattering with high precision, and the results could point a way to the new physics beyond the SM.

Supersymmetry discovery is possible at the LHC, mainly by looking for missing-E_T if the background can be well suppressed. The ILC will be essential in distinguishing whether the detected new particles are the superpartners of known particles by measuring their parameters such as masses. Chapter 4 gives an example of mass measurement of chargino and neutralino masses in a model independent manner. Such precision measurements could help to understand the force unification at the higher energy scale.

Of course SUSY may not be the correct theory of new physics, for example, gravitons escaping into extra dimensions could also explain the weak coupling of gravity [35]. The

observation of the excited graviton states at the ILC will help to determine theory parameters for the additional dimensions [36]. Several alternative models of new physics addressing problems of the SM have been reviewed in [34].

The ILC will provide a very clean environment, known centre-of-mass energy and polarized beams which enable precision measurements that are very difficult to achieve at a hadron collider. Therefore the ILC results combined with LHC discoveries will unveil new physics beyond the SM and will substantially improve our understanding of the nature.

2.1.2 ILC Accelerator

The design of the International Linear Collider is based on two decades of accelerator R&D since the construction and operation of the SLAC Linear Collider (SLC)[37], which is the proof-of-principle machine of the linear collider concept. The ILC is a proposed electron-positron collider running at a centre-of-mass energy up to 500 GeV, with the peak luminosity of $2 \times 10^{34}\text{cm}^{-2}\text{s}^{-1}$. Physics runs for any energy above 200 GeV and calibration runs at $\sqrt{s} = 91\text{GeV}$ (Z boson mass) will be possible, and a potential upgrade to 1 TeV is foreseen. The key design parameters are listed in table 2.1.

The overall layout of the ILC baseline indicating the major subsystems is shown in Figure 2.1[38]. The total length is approximately 31 km. It consists of an electron and a positron arm, both of the same length. The electron source, the damping rings and the positron auxiliary source are located in the centre of the complex around the Interaction Point (IP).

The polarized electron source generates the required bunch train of electrons based on a photocathode DC gun. The electron DC gun is based on the SLC design [39] incorporating recent technology developments [40]. Polarized electrons ($P > 80\%$) are generated through the photoelectric effect when a GaAs-based photocathode is illuminated with polarized laser light. A Ti:sapphire laser system is used for generating the short (1 ms) bunch trains. The polarized electrons are accelerated to 5 GeV before they are transported to the electron Damping Ring (DR).

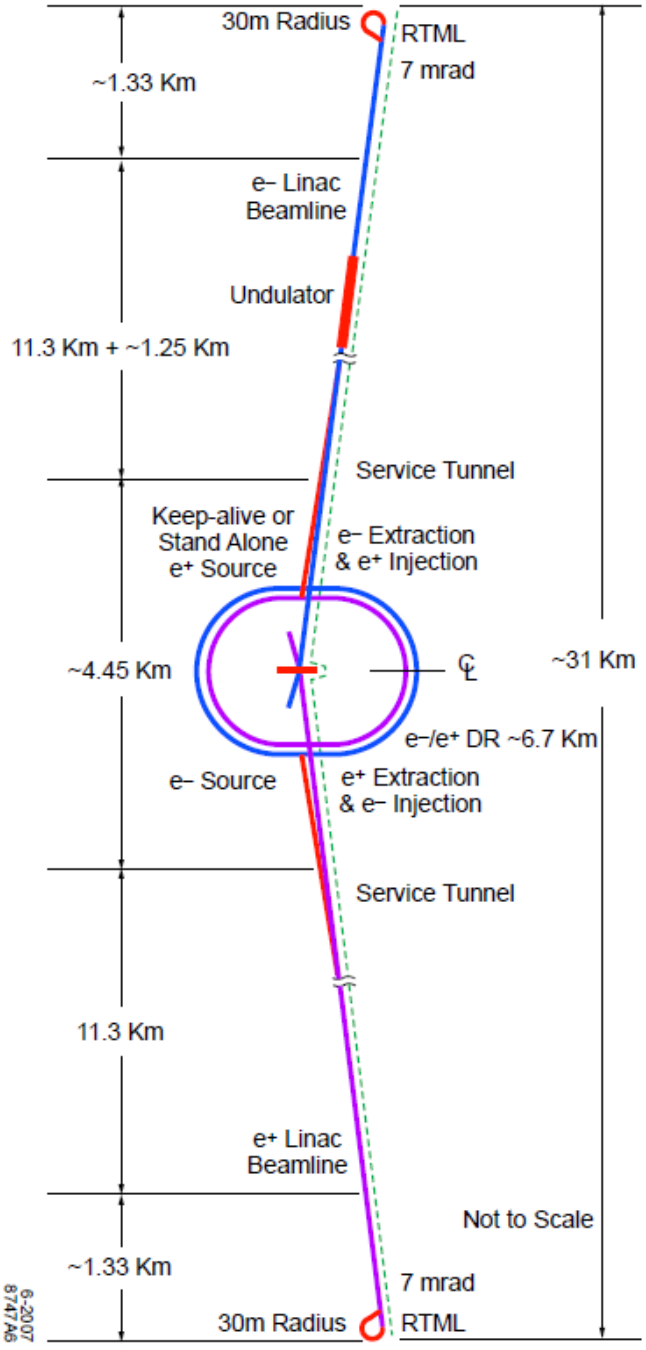

Figure 2.1: Schematic layout of the ILC complex [38].

Parameter		Unit
Center-of-mass energy range	200 - 500	GeV
Peak luminosity*	2×10^{34}	$cm^{-2}s^{-1}$
Average beam current in pulse	9.0	mA
Pulse rate	5.0	Hz
Pulse length (beam)	~ 1	ms
Number of bunches per pulse	1000 - 5400	
Charge per bunch	1.6 - 3.2	nC
Accelerating gradient*	31.5	MV/m
RF pulse length	1.6	ms
Beam power (per beam)*	10.8	MW
Typical beam size at IP*($h \times v$)	640 × 5.7	nm
Total AC Power consumption*	230	MW

Table 2.1: Design parameters for the ILC. The parameters labeled with * are values at 500 GeV center-of-mass energy[38].

In the 6.7 km long damping ring the electron beam's large longitudinal and transverse emittances are damped to low emittances during the 200 ms between the bunch trains. Bunches from the electron source can be delayed here to compensate pulse-to-pulse variations of beam parameters. Injection or extraction of single bunches is enabled in the DR without affecting the beam emittance or stability. A similar positron damping ring is housed in the same tunnel with the same functions. The two damping rings will be placed right above each other.

The beams from the damping rings are collimated and transported to the upstream end of the main linac by the Ring To Main Linac (RTML) system. The polarization of the beam is rotated from vertical to any desired angle by a spin rotator. The RTML also includes a two-stage bunch compressor to compress the beam length from millimeters as in the DR to a few hundred micrometer as required at the IP. The 5 GeV beams are accelerated to 15 GeV after the bunch compressor before injected into the main linac.

The electron beam is directed to an offset beamline through an undulator for use as a positron source and then returned to the main linac. The positrons are produced by the process of photoproduction. The high energy photons emitted by electrons from the

undulator (of order of 10 MeV) will hit a Ti-alloy target to produce electron-positron pairs. The circular polarization of the photon can transfer to the polarization of the positron, depending on the energy transferred to the positron [41]. The ILC positron beam could achieve a spin polarization of 30%. The electrons and photons are separated from the positrons and dumped. The pure positron beams will be pre-accelerated to 400 MeV in a normal-conducting RF accelerator and then accelerated to 5 GeV in a super-conducting Booster Linac. If high-energy electrons are not available, there is a separate low-intensity positron source upstream of the super-conducting linac for commissioning and tuning use. Similar to the electron beams, the positron beams will afterwards be transported through the damping ring, RTML system, and the Main Linac for final acceleration.

The Main Linac is responsible for accelerating the 15 GeV electron/positron beams to the required 250 GeV for collision, at the average accelerating gradient of 31.5 MV/m. The ILC will use Superconducting RF (SCRF) cavities. These 1.3 GHz niobium cavities operate at 2 Kelvin provided by liquid helium. The superconducting technology means minimal energy loss, which enables the use of long-pulse RF and relaxation of peak power generation. Each linac contains hundreds of RF units, each with 3 cryomodules containing 26 one-meter long SCRF cavities. The SCRF is one of the technological highlights of the ILC, one reason being the high gradient (31.5 MV/m in each 9-cell cavity). This has been achieved with several cavities [42][43] but will still be challenging at mass-production levels. The preparation and assembly of the cavities have to be in a cleanroom environment using electropolishing to ensure the micron-level surface smoothness. Blemishes or impurities will cause them to lose the superconductivity and hamper high-gradient performance.

Downstream of the main linacs, situated in the heart of the complex is the Beam Delivery System (BDS). Its main function is to focus the high energy electron/positron beams from the linac to the extremely small size for luminosity production, to bring them into collision and to damp the used beams. The BDS system is located 10 m below the damping rings to prevent electromagnetic interference. The beams are designed to collide at a single Interacting Point (IP) with crossing angle of 14 mrad. The nominal parameters of the beams and the designed

	min	nominal	max	unit
Bunch population	1	2	2	$\times 10^{10}$ particles
Number of bunches	1260	2625	5340	
Linac bunch interval	180	369	500	ns
RMS bunch length	200	300	500	μm
Normalized horizontal emittance at IP	10	10	12	mm·mrad
Normalized vertical emittance at IP	0.02	0.04	0.08	mm·mrad
Horizontal beta function at IP	10	20	20	mm
Vertical beta function at IP	0.2	0.4	0.6	mm
RMS horizontal beam size at IP	474	640	640	nm
RMS vertical beam size at IP	3.5	5.7	9.9	nm
Vertical disruption parameter	14	19.4	26.1	
Fractional RMS energy loss to beamstrahlung	1.7	2.4	5.5	%

Table 2.2: Beam parameters of the ILC[38].

ranges are shown in Table 2.2. The ILC has two detectors in the Interaction Region Hall (IR).

The ILC RDR baseline is designed for the 500 GeV centre-of mass energy. In order to upgrade to $\sqrt{s} = 1$ TeV, the linacs and beam transport lines have to be extended by $\sim$ 11km for each arm. Some components in the beam delivery systems have to be replaced or augmented. In 2009 a modified design Strawman Baseline Design 2009 (SB2009)[44] was proposed and is currently under study. Initiated by the cost-performance optimization, the SB2009 was mainly aimed at improving the machine design in preparation of the ILC Technical Design Report and Detailed Baseline Design documents for the detectors to be published in 2012.

2.2 Silicon Detector Concept

The Silicon Detector (SiD) concept is one of the two ILC detector concepts which are designed to perform precision measurements of e^+e^- collisions and to discover any phenomena related to new physics. The requirements for the detector are therefore set by key physics processes

to be measured by SiD. Some general requirements include[45]:

- Excellent jet energy resolution;
- Excellent flavour-tagging performance, including high purity and efficiency for heavy quark identification;
- Good momentum resolution capable of reconstructing the di-lepton recoil mass of the Higgs with better resolution than beam-energy spread;
- Full hermeticity for missing energy and momentum determination;
- Time resolution capable of separating single bunch crossings to suppress overlapping of events.

Take the requirement on jet energy resolution as an example. For many ILC specific measurements it is essential to separate the WW and ZZ final states, such as the mass measurement of the supersymmetric particles chargino and neutralino (detailed discussion as in Chapter 4). Assuming both W or Z bosons decay hadronically, if we plot the invariant mass of one of the W or Z bosons (reconstructed from two jets) in x axis and the other di-jet mass in the y axis as in Figure 2.2, the WW or ZZ final states will populate around (m_W, m_W) and (m_Z, m_Z) respectively. For the jet resolution of $60\%/\sqrt{E}$ achieved by LEP experiments, these final states cannot be distinguished on the correlated di-jet mass plot. In order to do so a jet resolution a factor of 2 better than that at LEP is required.

Given these requirements SiD is based on a silicon pixel vertex detector, silicon tracking, silicon-tungsten electromagnetic calorimetry and highly segmented hadronic calorimetry. Most of the subsystems will make use of silicon technology because of its high precision, robustness against machine background and also because its response is fast enough to be sensitive to a single bunch crossing. The required jet energy resolution is achievable with a Particle Flow Algorithm (PFA) [47], which has a strong influence on the detector subsystem design. The whole picture is completed with a 5 T solenoid and iron flux return which is

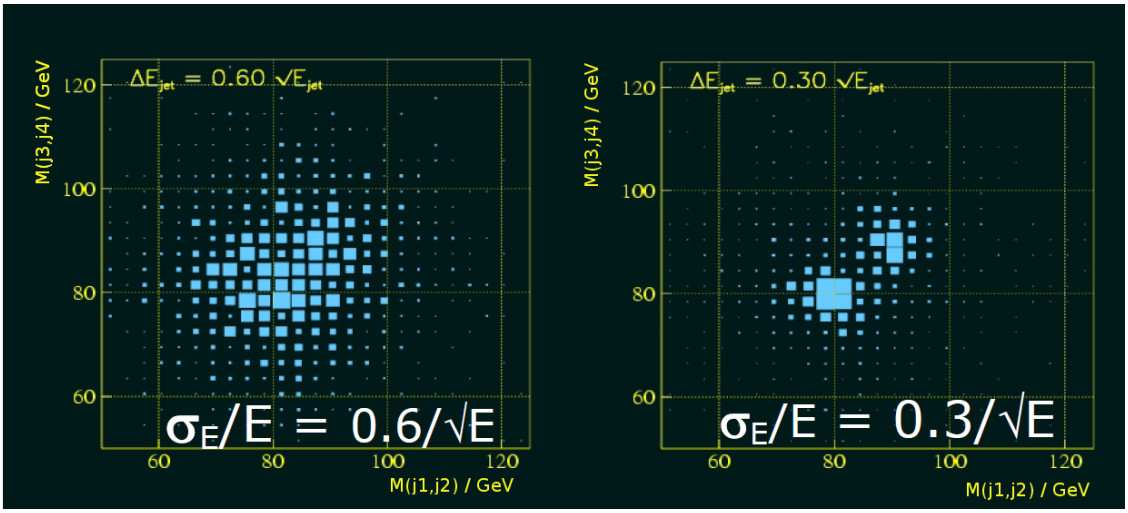

Figure 2.2: Jet mass correlation assuming a jet energy resolution of $60\%/\sqrt{E}$ (left) and $30\%/\sqrt{E}$ (right). This is reconstructed for four jets final states from either WW or ZZ. The vertical and horizontal axes stand for two di-jet masses [46].

integrated into the muon identification system. A quadrant of the SiD design is illustrated in Figure 2.3. The key design parameters are listed in Table 2.3.

The Particle Flow Algorithm approach is built-in to the SiD design philosophy. The PFA uses information from all the detector subsystems to reconstruct hadronic jets. Tracking information is used to determine momenta of charged particles. The energy of photons is determined by the electromagnetic calorimeter (ECAL). The momenta of the neutral hadrons (mainly π^0) that survived after passing the ECAL are determined in the hadronic calorimeter (HCAL). The goal of a good PFA for the SiD is to obtain a jet energy resolution of 3-4% for energies between 40 and 500 GeV. A detailed description of the PFA developed for the SiD can be found in Section 4.2.2.

The performance-cost balance has been considered since the start of the SiD design, and the choice of a high field solenoid is such an example. The $B = 5$T magnetic field helps to optimize the cost by building a more compact detector, while at the same time improves the jet energy resolution compared to lower value of B and provides a better track momentum resolution. Since it minimizes the beam pipe radius by constraining the orbits of the e^-e^+ pairs produced in beamstrahlung[1] (Figure 2.4), the high magnetic field potentially improves

[1]In a collider, beamstrahlung is a process of energy loss of electrons (or positrons) due to their electromagnetic interaction with the positron (or electron) coming in the opposite direction.

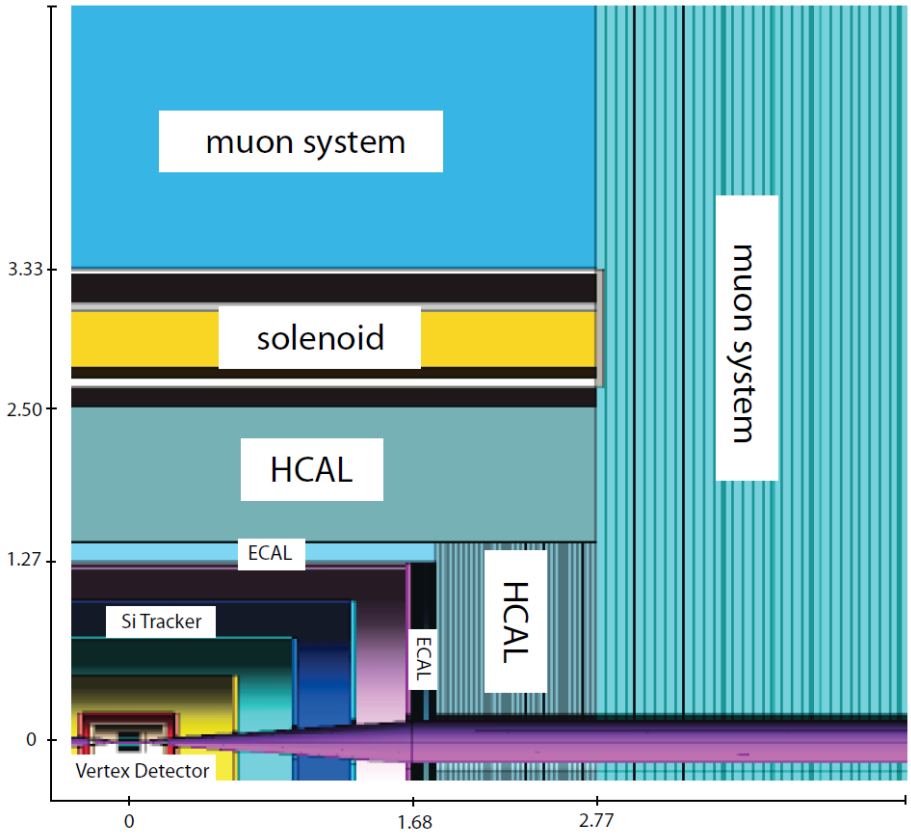

Figure 2.3: Illustration of a quadrant of SiD. The scale shown is in meters.[48]

SiD Barrel	Technology	Inner radius	Outer radius	Z max
Vertex detector	Pixel	1.4	6.0	± 6.25
Tracker	Silicon strips	21.7	122.1	± 152.2
EM calorimeter	Silicon-W	126.5	140.9	± 176.5
Hadron calorimeter	RPCs	141.7	249.3	± 301.8
Solenoid	5 Tesla	259.1	339.2	± 298.3
Flux return	RPCs	340.2	604.2	± 303.3

SiD Forward	Technology	Inner Z	Outer Z	Outer radius
Vertex detector	Pixel	7.3	83.4	16.6
Tracker	Silicon strips	77.0	164.3	125.5
EM calorimeter	Silicon-W	165.7	180.0	125.0
Hadron calorimeter	RPCs	180.5	302.8	140.2
Flux return	RPCs	303.3	567.3	604.2
LumiCal	Silicon-W	158.0	173.0	19.0
BeamCal	Silicon-W	295.0	320.0	14.5

Table 2.3: Key parameters of the baseline SiD design [48]. All dimensions are given in cm. RPC stands for Resistive Plate Chamber.

the resolution of the vertex detector as well.

2.2.1 Vertex Detector

Many precision measurements such as the top Yukawa coupling and Higgs branching ratio at the ILC will benefit greatly from efficient and high purity flavour tagging. The b and c quarks have a characteristic decay length of $\sim$ centimeter, and such decays form secondary vertices (while the interacting point is also called primary vertex). This could be detected by the vertex detector, the innermost subsystem of the SiD. Based on silicon pixel sensors the vertex detector subsystem is designed to reconstruct the primary, secondary and even tertiary vertices and to identify the b and c quarks with a high purity as well as efficiency.

The vertex detector subsystems consists of five barrel layers and three forward region disks, both based on silicon pixels. Three more outer disks are located at larger $|z|$ to cover the transition region between the vertex detector and the outer tracker. An R-z view of the

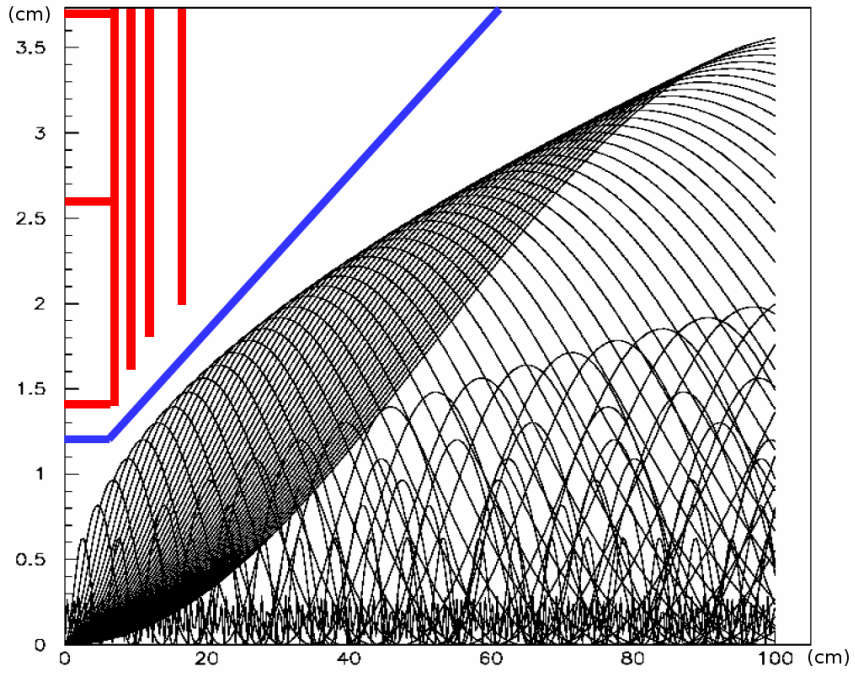

Figure 2.4: The maximum envelope of the e^+e^- pair backgrounds in a 5T field. The units are in cm. Position of the vertex detectors are also indicated [46].

vertex detector layout is shown in Figure 2.5, and the dimensions of each layer are listed in Table 2.4. This arrangement ensures a hermeticity for $\cos\theta \leq 0.984$.

The SiD vertex detector is challenging for sensor technology in many aspects. A position resolution of 5μm or better is required in both r-z and r-ϕ directions. This is necessary to limit the uncertainty of the impact parameter measurement to $\sigma_{rz} = \sigma_{r\phi} = 5 \oplus 10/p \sin^{3/2}\theta \mu$m, where p is momentum. The impact parameter is defined as the distance

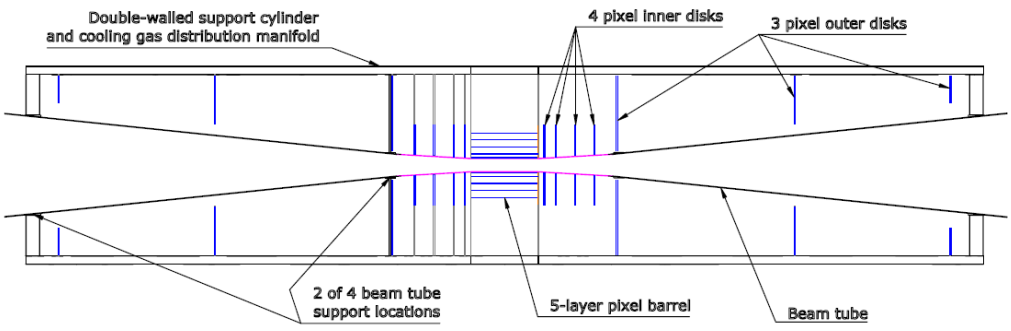

Figure 2.5: R-z view of the vertex detector. The support structures are not drawn for the right side.[48]

Barrel Region	R	Length	Number of sensors in φ
Layer 1	14	125	12
Layer 2	21	125	12
Layer 3	34	125	20
Layer 4	47	125	28
Layer 5	60	125	36
Disk	R_{inner}	R_{outer}	z_{center}
Disk 1	15	75	76
Disk 2	16	75	95
Disk 3	18	75	125
Disk 4	21	75	180
Forward Disk	R_{inner}	R_{outer}	z_{center}
Disk 1	28	166	211
Disk 2	76	166	543
Disk 3	118	166	834

Table 2.4: Parameters of the vertex detector. Units are mm.[48]

of a track at the closest point to the interaction point or the primary vertex. The point resolution in turn requires a sensor with $20 \times 20 \mu\text{m}^2$ pixels. In order to minimize multiple scattering, a thickness of at most $0.1\% X_0$ is targeted, where X_0 is the radiation length. This not only requires a low material budget in the sensitive region and supporting structures, but also implies that gaps and dead areas in the silicon should be minimized to allow mass to be distributed uniformly. The power consumption for the whole barrel and end disks should be limited to as low as a few tens of watts which will make gas cooling possible for the least material penalty. The operational environment also imposes restrictions on the readout of the vertex detector sensors. In order to keep a low occupancy, at least 20 frames should be read during the 1 ms bunch train. Several candidate sensor technologies are discussed in Chapter 3.

2.2.2 Tracker

The SiD outer tracker combined with the vertex detector forms an integrated tracking system. The precision physics measurements planned at the SiD require high momentum resolution and low material budget for the tracker, similar to the vertex detector. Besides, due to the large volume of the tracker, its components should ideally be inexpensive, easily mass-produced and robust against aging. Based on these considerations silicon microstrip sensors are chosen.

The silicon tracker consists of five barrels and four disks at each end of the outer four barrels. The layout of the tracker is shown in Figure 2.6, where the vertex detector and its supporting structure are also plotted. The inner radius of the tracker is limited by the vertex detector and the beam pipe because during servicing the outer tracker should move longitudinally while the inner parts are fixed. The parameters of each tracker barrel layer and endcaps are listed in Table 2.5. For the baseline design, the outer surface of the barrel layers are covered with single-sided silicon sensors. The sensors are 10 cm $\times$ 10 cm which determines the longitudinal readout segmentation. They are 300 μm thick and have a readout pitch of 50 μm with intermediate strips. For better pattern recognition, both sides of the disks are covered with wedge shaped sensors, with a 12° stereo angle between the strips. This design is aimed at providing 3-D points.

Various Monte Carlo simulations have been carried out to study the tracking performance. One example is given in Figure 2.7. It shows the resolution of the track momentum and resolution of the distance of the closest approach in the r-φ direction. The resolutions decreases with the incoming angle (below 90°) due to the multiple scattering. The track momentum resolution figure (left) demonstrates that a good track momentum resolution (better than 1%) can be achieved, which deteriorates at very high jet energies. In the figure of impact parameter resolution (right), it can be seen that at the high momentum limit, resolution of about 4μm is expected for the impact parameter.

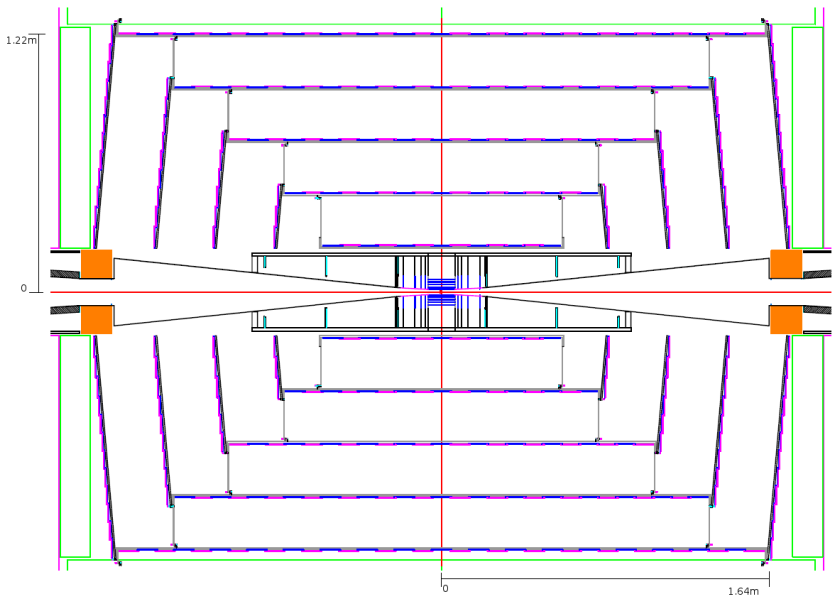

Figure 2.6: R-z view of the SiD tracking system.[48]

Barrel region	$\langle R \rangle$ (cm)	Length of sensor coverage (cm)	Number of modules in φ	Number of modules in z
Barrel 1	21.95	111.6	20	13
Barrel 2	46.95	147.3	38	17
Barrel 3	71.95	200.1	58	23
Barrel 4	96.95	251.8	80	29
Barrel 5	121.95	304.5	102	35
Disk region	z_{inner} (cm)	R_{inner} (cm)	R_{outer} (cm)	Number of modules per end
Disk 1	78.89	20.89	49.80	96
Disk 2	107.50	20.89	75.14	238
Disk 3	135.55	20.89	100.31	428
Disk 4	164.09	20.89	125.36	662

Table 2.5: Main parameters of the tracking detector.[48]

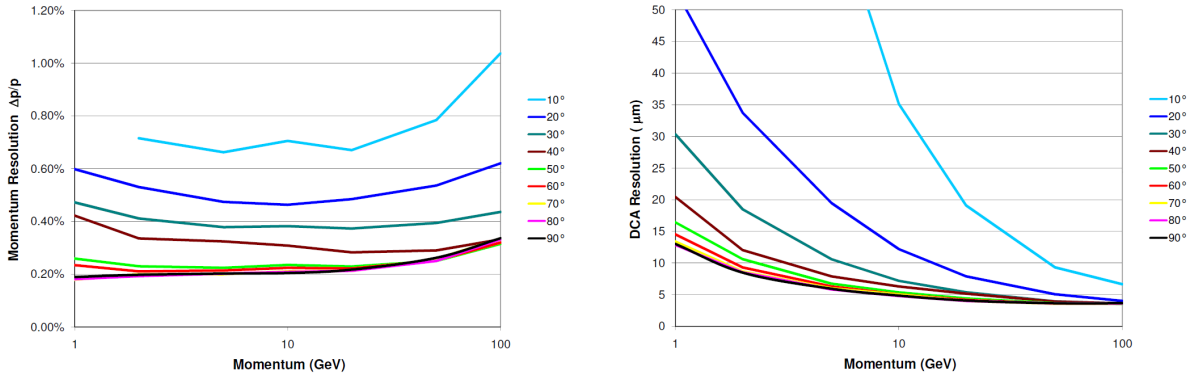

Figure 2.7: Resolution of the track momentum (left) and resolution of the Distance of Closest Approach (DCA) in the r-φ direction (right), as function of track momentum at various polar angles.[48]

2.2.3 Electromagnetic Calorimeter

Since the calorimetry design is essential for optimization of the PFA performance, a number of requirements should be satisfied by the electromagnetic calorimeter (ECAL) design. For example overlaps of electromagnetic showers have to be avoided to better separate the electrons and photons in the ECAL. This, in turn, requires a small Molière radius of the calorimeter material. Highly segmented readout in the transverse and longitudinal directions is required for imaging capability. Small transverse segmentation also helps to differentiate electron showers from MIP tracks. Fine longitudinal segmentation is important not only for its obvious role in improving energy resolution, but also for the ability to reconstruct charged particle tracks, which makes the ECAL an imaging calorimeter and enables calorimeter-assisted tracking. A simulated $\rho^+ \to \pi^+\pi^0$ decay reconstructed in the ECAL is illustrated in Figure 2.8 to show the SiD pattern recognition capability. Two photons from the π^0 are clearly separated and the charged tracks are visible in the ECAL.

The ECAL barrel is mounted inside the hadronic calorimeter, with an inner radius of 1.27 m and maximum $|z|$ of 1.7 m. An EM energy resolution of $17\%/\sqrt{E}$ is aimed for. The radial structure has 30 layers of tungsten alloy absorber with silicon detectors sandwiched between each other. The alloy which includes 93% of tungsten is chosen as the absorber because of its small radiation length ($X_0 = 3.9$ mm) and Molière radius ($R = 9.7$ mm), as

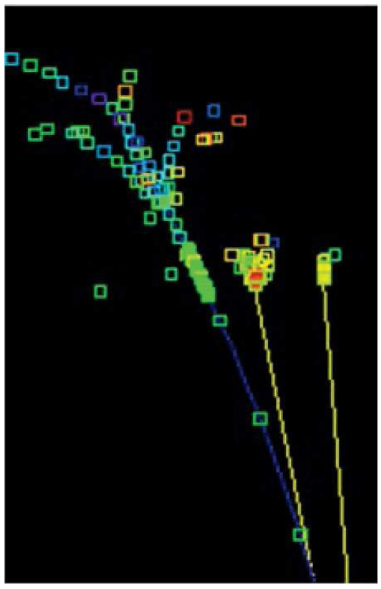

Figure 2.8: Simulated $\rho^+ \to \pi^+\pi^0$ decay in the SiD detector[48]. The two smaller clusters on the right hand side correspond to photon showers in the ECAL caused by two photons from the π^0 decay; while the π^+ leaves a few hits in the tracker and its decay in the ECAL gives rise to a shower with clear inner structure, due to the positron in its decay products.

well as its mechanical stability. In addition, tungsten has a large interaction length which makes separation of electromagnetic and hadronic showers in the ECAL easier. The inner 20 tungsten layers are 2.5 mm thick each while the outer 10 are 5 mm thick, both with the same readout gap of 1.25 mm. This adds up to a total depth of $26X_0$.

Two options for the silicon sensor technology are under development. One of them, as in the baseline design, uses hexagonal sensors, each segmented into 1024 pixels with area of 13 mm^2. The sensor readout electronics has a large dynamic range, implemented in a KPiX ASIC [49]. The other option is Monolithic Active Pixel Sensor (MAPS) [50][51]. These sensors have $50 \times 50\mu$m^2 pixels, and they can be manufactured in a commercially available 180 nm CMOS process. A comparison of the options is summarized in Table 2.6.

2.2.4 Hadronic Calorimeter

A small Molière radius and highly segmented detectors are required by the PFA also for the hadronic calorimeter (HCAL). Furthermore the HCAL must be deep enough to contain all

	Baseline	MAPS option
Pixel size	13 mm^2	$50 \times 50 \mu$m^2
Pixels per silicon sensor	1024	1,000,000
Channels per KPiX readout chip	1024	-
Pixel dynamic range requirement	$\sim$ 0.1 to 2500 MIPs	1 MIP (digital)
Heat load requirement	20 mW per sensor	20 mW per sensor

Table 2.6: Parameter of the baseline and MAPS options.[48]

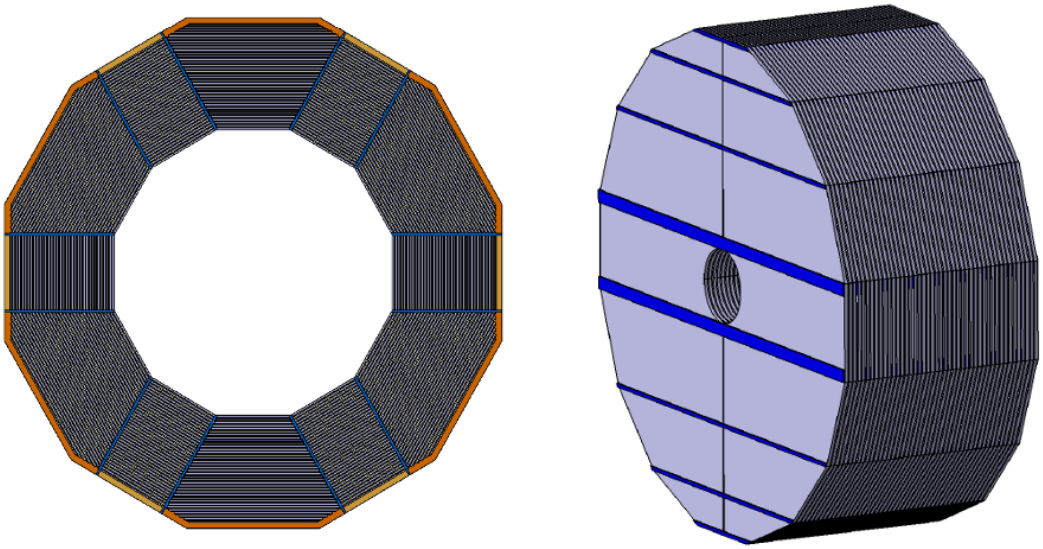

Figure 2.9: Cross-section of the HCAL barrel (left) and face and top view of the HCAL endcap (right).[48]

particles in hadronic showers while being able to fit inside the solenoid so as to avoid energy loss in the magnet. Based on these considerations, stainless steel is chosen as the HCAL absorber. Steel has a radiation length X_0 of 1.8 cm and an interaction length λ of 16.8 cm which leads to the smallest ratio of X_0/λ in most commonly used absorber materials. The HCAL barrel consists of 40 layers of 2 cm thick steel, separated by 8 mm gaps which has a total depth of 4.5λ. It is located outside the ECAL and inside the solenoid, with internal radius $R_{int} = 1419$ mm and external radius $R_{ext} = 2583$ mm. The maximum $|z|$ is 3018 mm. In order to extend the hermeticity an endcap is inserted into each end of the barrel. The shape of the barrel and endcaps is shown in Figure 2.9. The detector layer structure in the endcap is the same as in the barrel.

The active detector element is located in the gap between the absorber layers. Resistive

Plate Chambers (RPC) are used in the baseline design. RPCs are gas detectors where the gas in contained between two resistive plates with a high voltage applied across the gap. The passage of charged particles initiates a streamer or an avalanche which can be recorded as a signal on readout strips or pads placed on the outer surface of the plates. Various chamber geometries are possible with a requirement that all have readout units of $1 \times 1\text{cm}^2$, and the gas is composed of Freon R134A (94.5%), isobutane (5.0%) and sulfur-hexafluoride (0.5%). A test calorimeter with 10 chambers has been built and tested with cosmic rays and in a test beam [52]. The RPC is not the only detector technology available; other options under active study include Gas Electron Multipliers (GEM) [53], MICRO MEsh GAseous Structure (MICROMEGAS) [54] and scintillator with Silicon Photomultipiers (SiPM) [55][56].

2.2.5 Magnet system

The largest superconducting magnet ever built so far is the CMS solenoid with a 4T field installed on the LHC. It is a proof-of-concept for the SiD magnet and provides a starting point and useful experience for the SiD design [57]. The main design parameters of both are compared in Table 2.7. Similar to CMS, a high-purity aluminium conductor stabilizer with indirect liquid helium cooling is used. A winding design with six layers is proposed to provide sufficient linear current density to generate a 5T field. The CMS magnet has the largest stored energy per unit cold mass (E/M) value of all existing magnets. The E/M value is a measure of stability and safety of a magnet [58] because the more stored energy the cold mass is able to absorb, the less likely thermal damage is to occur during a quench. The SiD solenoid is designed with a slightly higher E/M of 12 kJ/kg, which is close to the upper bound where large aluminium dominated magnets can be operated in a fail-safe manner.

In addition to the superconducting solenoids, the magnet system also incorporates a 550 kA turns superconducting Detector Integrated "anti" Dipole (antiDID) which generates a 600 G dipole field. It is used to correct the deviation in the vertical plane for the beam entering the interaction region with a horizontal crossing angle [59]. This helps direct low energy beamstrahlung pairs to the extraction aperture and reduces the total radiation on the

Quantity	SiD	CMS	Units
Central field	5.0	4.0	T
Stored energy	1.56	2.69	GJ
Stored energy per unit cold mass	12	11.6	kJ/kg
Operating current	17.75	19.2	kA
Inductance	9.9	14.2	H
Fast discharge voltage to ground	300	300	V
Number of layers	6	4	
Total number of turns	1457	2168	
Peak field on superconductor strands	5.75	4.6	T
Number of superconductor strands	36	32	
% of short sample	32	33	
Temperature stability margin	1.6	1.8	K
Total mass of solenoid	125	220	Metric ton
Cryostat R_{min}	2.591	2.97	m
Cryostat R_{max}	3.392	3.78	m
Cryostat Z_{max}	$\pm$ 3.033	$\pm$ 6.5	m
Coil R_{min}	2.731	3.18	m
Coil R_{max}	3.112	3.49	m
Coil Z_{max}	$\pm$ 2.793	$\pm$ 6.2	m
Operating temperature	4.5	4.5	K
Cooling method	Forced flow	Thermosiphon	

Table 2.7: Comparison of SiD and CMS superconducting solenoids [48].

BeamCal. The DID corrector is also able to compensate for rotation of the beam polarization or beam size growth caused by the synchrotron radiation.

2.2.6 Muon Detector

The SiD muon detector function is to identify muons originating from the interaction point with high efficiency against the hadron background which is mainly pions and kaons. The first layers of the muon system are also useful in catching the tail of hadron showers. The system starts outside the solenoid cryostat at a radius of 3.4 m and is integrated with the flux return of the magnet. The flux return consists of eleven layers of 20 cm thick steel in an octagonal barrel and another eleven 20 cm layers of steel octagons in the endcap. The muon detectors are inserted into the 4 cm gaps between the layers. A detector layer is also inserted between the solenoid and the first steel barrel layer.

In the baseline design double-layered resistive plate chambers (RPC) are chosen for the muon detector. RPCs are not unfamiliar as a candidate for muon detectors since they are affordable and easy to construct in various sizes and shapes. They are used in BaBar[60], BELLE[61], ATLAS[62] and CMS[63] experiments. The RPC R&D is focused on the readout design[64] and the study of their aging properties[65] which has been the major concern for RPCs. Silicon photomultipliers are considered as an alternative technology for the muon detector based on the strip-scintillator design of the MINOS experiment[66][67].

2.2.7 Forward Detector

The full angular coverage of the SiD forward region where $|\cos\theta| \geq 0.99$ is completed by two calorimeters, the Luminosity Calorimeter (LumiCal) and Beam Calorimeter (BeamCal)[68]. In addition, to extend the detector hermeticity they also have important physics tasks. The LumiCal will use small-angle Bhabha scattering to measure the integrated luminosity to a relative precision better than 10^{-3}. The luminosity in reality has a distribution due to beamstrahlung emission, and the LumiCal is also responsible for measuring the luminosity

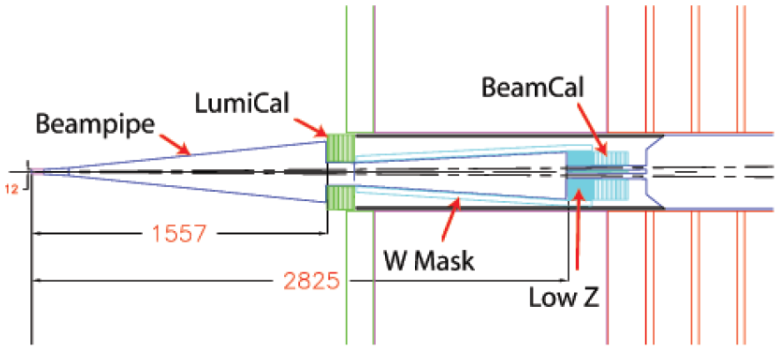

Figure 2.10: Forward region design. Units are cm.[48]

spectrum. The BeamCal is used for monitoring the instantaneous luminosity with beamstrahlung pairs.

An r-z view of the forward detector layout is shown in Figure 2.10. The LumiCal is surrounds the beampipe with inner radius 6 cm and outer radius 20 cm, and covers a polar angle from 40 mrad to 90 mrad. The BeamCal sits further down the beampipe covering from 3 mrad to 40 mrad. Longitudinal structures of both calorimeters follow the same silicon-tungsten design as the ECAL. There is a tungsten mask between the LumiCal and BeamCal to prevent backscattered low energy particles from entering the central detectors.

2.2.8 Machine Detector Interface

Together with the SiD, the International Large Detector (ILD) is another detector concept proposed for the ILC [69]. Its structure of subdetectors is similar to that of the SiD in general, with certain different features. The nominal magnetic field is 3.5T rather than 5T, resulting in a larger volume. A large volume time projection chamber (TPC) as part of the tracking system is another difference from the SiD design.

The ideal arrangement for two experimental detectors would be two beamlines serving each one at two interaction points, which is unfortunately not possible due to the high cost of the beamlines. Therefore the two detectors will work in so-called push-pull mode [70]. In such an arrangement, there is only one interaction region and the two detectors will be

moved alternately to the beam position to share the luminosity.

Many technical challenges have to be addressed for the push-pull arrangement. The time required to switch detectors should be kept to a minimum so as to avoid loss of luminosity. A switch time of about one day is targeted for a period of approximately one month for each detector on beamline. In order to ensure rapid switch, part of the magnetic doublet that provides the final focus for the beam (QD0) is designed to move with the detector. The alignment will be another issue for the push-pull arrangement. A good guiding mechanism should determine the path and position of the detectors to a precision of ± 1 mm. The detector must have an internal alignment system to check the alignment every time it is moved into the beam position. More detailed functional requirements can be found in [70] (while the SiD specific content can be found in [48]), and the effort towards a final push-pull scheme is still ongoing. In spite of the technical challenges for the detector and beamline designs, the push-pull arrangement is very cost-effective for the ILC.

Chapter 3

In-situ Storage Image Sensor for ILC Vertexing

ISIS (In-situ Storage Imaging Sensor) is a novel CMOS sensor with multiple charge storage capability developed for the ILC vertex detector by the Linear Collider Flavour Identification (LCFI) collaboration. This chapter reports test results for ISIS2, the second generation of ISIS sensors implemented in a 0.18 micron CMOS process. The local charge storage and charge transfer capabilities are unambiguously demonstrated.

3.1 Silicon Detectors for HEP Experiments

For high precision vertex detectors, silicon is a preferred material. It has a band gap of 1.1 eV, low enough for prolific charge production by ionization. For every micron of path length that a minimum ionization particle (MIP) traverses, about 80 electron-hole pairs are produced, well localized around the particle trajectory. The band gap is also high enough to prevent large dark current generation at room temperature ($kT \sim 0.026$eV) [71]. Advanced fabrication and processing techniques for silicon, due to the rapid progress in integrated circuit technology, also open the door to wider use of the material in particle detectors.

The simplest silicon detector is a reversely biased p-n junction, or a silicon diode. It is well-known that the concentration of charge carriers in silicon can be increased by doping[72].

Doping with material that has five valence electrons (like phosphorus) increases concentration of electrons as free charge carriers; semiconductors doped this way are called n-type. On the other hand doping with material with three valence electrons (such as boron) contributes to the concentration of holes, which is called p-type doping. When n-type and p-type silicon come into contact, they form a p-n junction. Thermal diffusion will drive electrons from the n-region to the p-region and the electrons will become bound in atoms by filling the holes. The holes in the p-region diffuse to the n-region as well. The trend continues until a layer of space charge near the junction appears. Electric potential and field are built up by the space charge to prevent further diffusion. This thin layer free of mobile charge is "depleted". If external voltage is applied to the p-n junction, with the positive polarity at the n-type side and negative polarity at the p-type side, free charge carriers are pushed further away from the junction, leaving an expanded depletion region. If the voltage is high enough the p-n junction is fully depleted, totally free of mobile charge carriers, forming a capacitor. If a high energy particle pass through the depletion region now, created electrons and holes will be rapidly swept to the electrodes. In this sense, a fully depleted p-n junction forms an ionization chamber. This is the basic principle for all silicon detectors based on high resistivity material.

The basic operation mentioned above is embodied in a simple strip detector as shown in Figure 3.1. The asymmetric p-n junction is composed of heavily doped p-type strips at the surface, and lightly doped n-type bulk. The depletion region extends across the n-bulk. At the backside a highly doped n-type layer provides electric contact to a high voltage bias, necessary for depletion. At the doped p-type strip side, metal strips (usually aluminium) are used to provide an electric contact. The metal strips and doped strips are sometimes separated by a SiO_2 layer, or AC-coupled, to decouple electronics from the effects of bias voltage and leakage current.

The charge produced by the passage of energetic particles will be collected at the nearest electrodes, so division of the sensor area into strips provides position information. The division (essentially the size of the strip pitch) determines the resolution. In colliding-beam

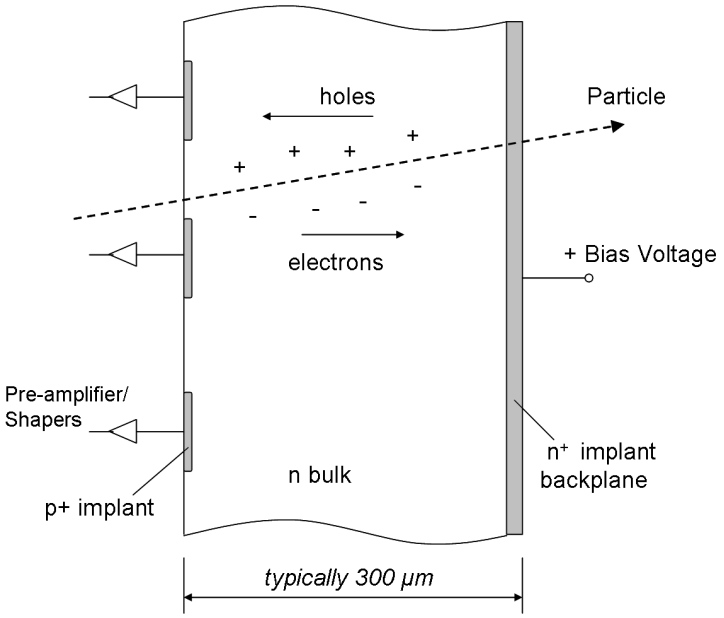

Figure 3.1: Operation principle of a simple silicon strip detector.

experiments the pitch of the strips typically ranges from 25 to 100 μm, and the strips' length can be centimetres to tens of centimetres [73]. With one set of strips only position information in one dimension is available, while another set of strips provides two-dimensional information if they are placed in the back side at an angle with the set in the front side. This configuration however suffers from 'ghosts'. For a simplistic estimation, N hits in the strip detector result in N^2 possible positions among which $N^2 - N$ are so called ghosts. This becomes more severe at high hit densities.

A pixel detector is therefore favourable for pattern recognition since the hit pixel unambiguously identifies the coordinates and there are no ghost hits present. Due to its fine granularity a pixel detector has better tolerance to hit density than a strip detector, therefore can be placed closer to the interaction point, which in turn results in a better precision for the impact parameter. An order of 10^4 reduction in area of a pixel compared to a strip means a huge reduction in the leakage current, hence a much lower shot noise.

Various approaches exist for fine segmentation of silicon detectors in two dimensions. The most straightforward one is a hybrid pixel detector, which is formed by an array of sensor chips connected to a matching readout chip via bump bonds. The readout array extends beyond the sensor chips to allow additional circuitry and external connections. The pixel

size is typically limited by the readout electronics required for each cell.

The charge-coupled device (CCD) was invented in 1969 [74] and was first used for particle detection in the 1980s [75]. During the charge collection phase the CCD acts as an array of small ionization chambers as introduced previously. During the readout phase the gates on pixels are properly biased to transfer the charge to the readout register. The most common three-phase CCD can be taken as an example, see Figure 3.2. There are three gates in each pixel which are connected to three different clock phases. Assume only the first gate is biased high and the charge (electrons) is held underneath. By raising the second gate the charge is shared between two gates by diffusion. Then lowering the first gate the charge is totally driven into the second gate. The movement of the charge packet from one pixel to the neighbouring one is illustrated in Figure 3.2. For a full CCD array, the charge from each pixel is first transferred vertically to the horizontal register at the end of the column, and then horizontally to the readout circuitry. A large number of transfers is required for the full array readout so charge transfer efficiency (CTE) almost equal to unity is essential. High CTE can be achieved in the so-called buried channel CCD by creating a buried-channel potential well [76]. The charge is therefore confined within the potential well without touching the silicon-SiO_2 interface, avoiding the trapping at the interface and greatly improving the CTE.

The hybrid pixel detectors need precision bump bonding, which adds to the complexity of processing. Realization of the similar functionality on a monolithic sensor will represent a major simplification in the detector assembly. The CMOS imagers which integrate the sensor region and readout circuitry monolithically at pixel level have been in wide use for optical imaging for more than a decade. Efforts to apply the technology to particle detection are also being explored. The ISIS2 sensor which will be described in the following sections is such an example. The monolithic pixel detectors will take advantage of the standard CMOS fabrication process, which has become very advanced and mature in the last decade.

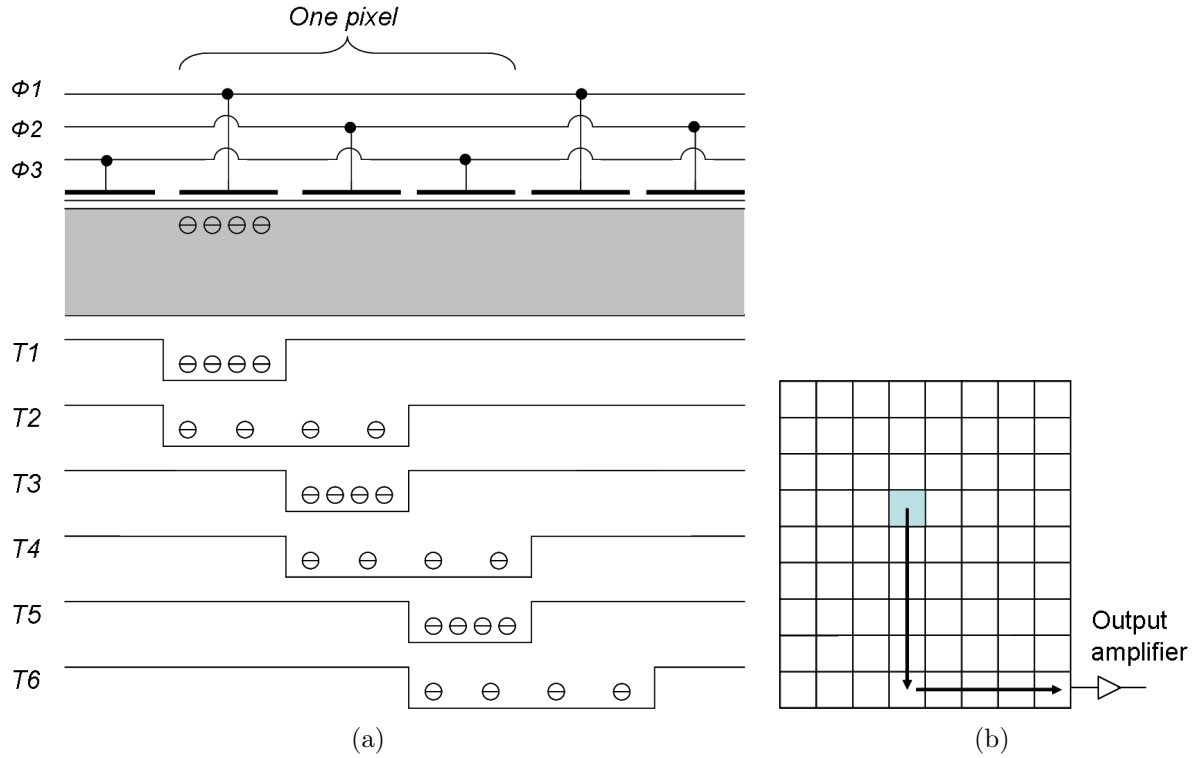

Figure 3.2: (a)Charge packet movement in three-phase CCD. One pixel of three phases is indicated. (b)Readout for CCD full array.

3.2 Introduction to ISIS

3.2.1 Two Approaches to Readout of ILC Vertex Detector

The ILC beam structure is shown in Figure 3.3 for the nominal beam parameters listed in Table 2.2. The repetition rate of the 1 ms long bunch train is 5 Hz. During each bunch train there are 2625 bunches[38], each separated by a 369 ns interval. Estimation of the particle flux in the detector predicts that there are 250 hits/mm^2 per bunch train for the innermost layer of the vertex detector in the barrel section. In order to keep the occupancy at a low level the signals have to be read out 20 times during each bunch train. The difficulty of this requirement can be stressed by a comparison to the SLD[77], a detector at the previous linear collider, SLC[37], which had a vertexing detector. The bunch crossings at the SLC were separated by 8 ms intervals and the signals at the vertex detector were only read out once during each bunch train.

The exact sensor technology is not yet decided for the ILC vertex detector but several

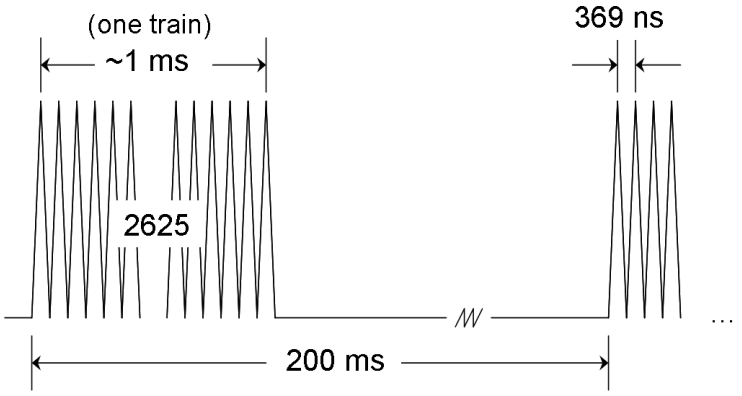

Figure 3.3: The bunch train structure of ILC beam for nominal parameters.

candidates are under development. They can be generally categorized into two types according to their approach to tackle the fast readout challenge. The first approach is readout as fast as possible during each bunch train at a speed of $50\mu s$ per frame, which is pursued by Column Parallel CCDs [78][79][80][81], Monolithic Active Pixel Sensors(MAPS)[82][83] and DEPleted Field Effect Transistor (DEPFET) sensors [84].

The other option is to store the charge at the pixel level during bunch trains and to read it out during the quiet time between collisions. The examples of this approach are ISIS (which will be discussed in detail in this chapter) and Flexible Active Pixel Sensors (FAPS) [85]. For the fast readout option, the peak power during the bunch trains is usually very high, therefore they are powered off between the bunch trains and on again when the next bunch train arrives. The ISIS approach, however, requires a much lower peak power, and avoids power cycling needed for fast readout approaches.

3.2.2 ISIS Principle

The In-situ Storage Image Sensor (ISIS) is a monolithic pixel detector with in-situ charge storage capability to meet the requirements at the ILC vertex detector. The concept of the ISIS sensor can be illustrated in the cross section of a pixel as shown in Figure 3.4. During collisions the charge generated in the $\sim 20\mu$m epitaxial layer is collected under the photogate. Then the raw charge is transferred down to the pixel-level storage cells, equivalent to a short CCD column. The signal charge will be shifted to the register every $50\mu s$ as the time

slicing required. The charge-voltage conversion and readout of the full array will happen in the 200ms quiet time between the bunch trains. The CCD register is protected from the epitaxial layer by the deep p^+ implant. There are openings on the p^+ implant below the photogate so that the signal charge can be collected by diffusion through the openings.

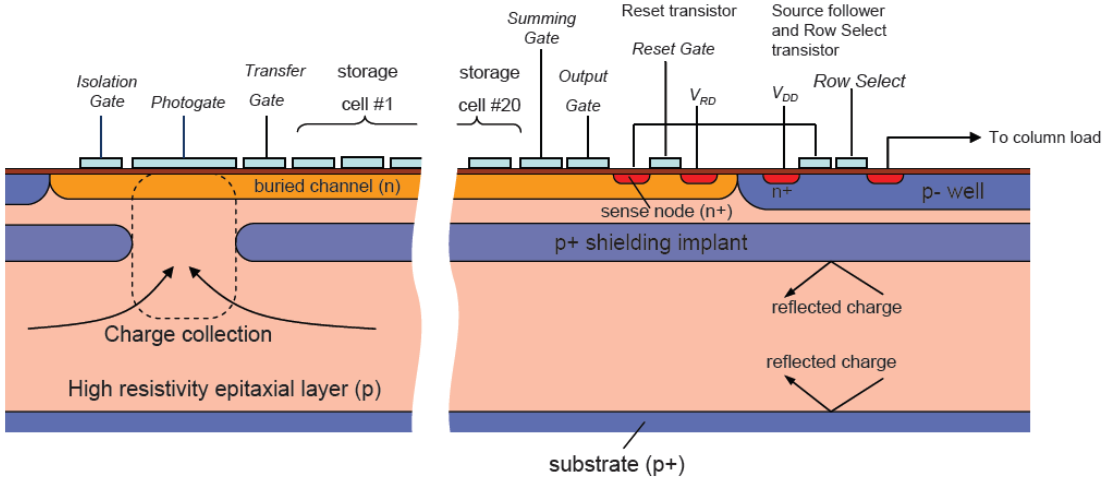

Figure 3.4: ISIS design concept.[86]

3.3 ISIS1

3.3.1 ISIS1 Design

The first generation device ISIS1 was produced to prove the feasibility of local charge storage using storage cells with a relatively large pitch. The ISIS1 sensor was manufactured by e2v technologies [87] in a CCD process with a feature size of $\sim 2\,\mu$m. Figure 3.5 shows an ISIS1 sensor wire-bonded onto a ceramic package. The epitaxial layer is $50\,\mu$m deep. There are 16×16 pixels each with pitch size $160 \times 40\,\mu\text{m}^2$. A photo of three ISIS1 pixels under the microscope is also shown in Figure 3.5. Each pixel has a $8 \times 8\,\mu\text{m}^2$ area photogate, 5 storage cells (a 5-cell CCD) and a three-transistor (3T) output circuit. The photogate is surrounded by isolation gates on three inactive sides and is separated from the memory cells by a transfer gate. The 3T structure consists of a reset transistor, a source follower and a row selector. A schematic sketch of an ISIS1 pixel is shown in Figure 3.6. Each column

connects to an on-chip load and to the gate of a larger source follower transistor. Each row is clocked separately so that the stored charge of any selected row can be read out in parallel.

Two variations of the ISIS1 sensor were manufactured, the basic one and the p-type one. Their difference is in the presence of the p^+ well encapsulating the buried channel. This $3\,\mu$m deep p^+ well is only present in the p-type sensors as shown in Figure 3.6. It reflects the charge created in the epitaxial layer and protects the CCD registers from parasitic charge collection. The charge is collected under the photogate with the help of the punch through effect. The punch through effect appears when the photogate voltage is high enough so the electrons are attracted to the photogate despite the presence of the p^+ well. The absence of the p^+ well in the basic type means the generated charge can be directly collected by the storage cells.

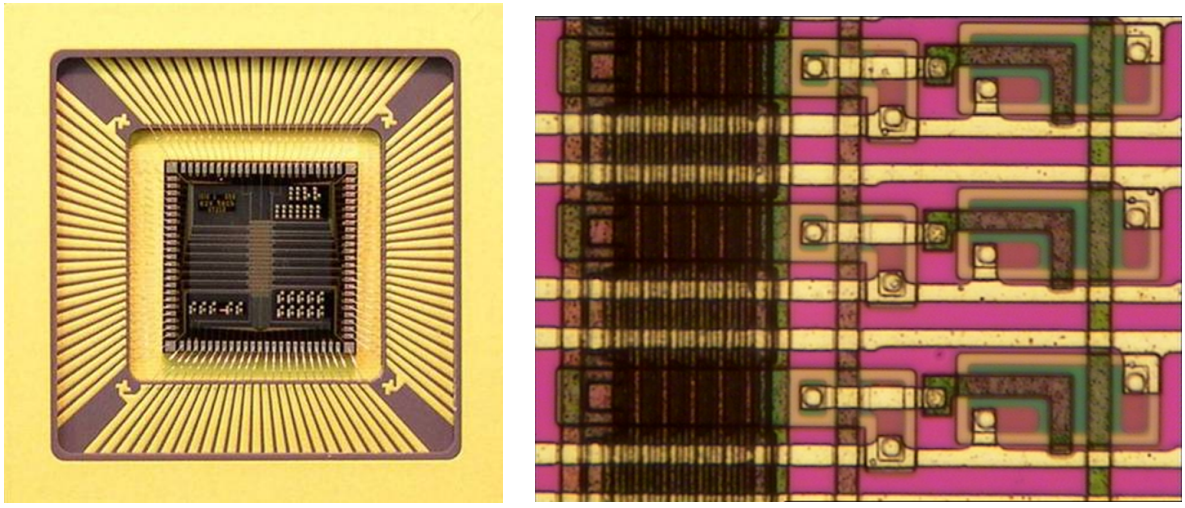

(a) (b)

Figure 3.5: (a)ISIS1 sensor wire-bonded onto a ceramic package; (b)Three pixels on ISIS1.[88]

3.3.2 ISIS1 Testing Results

The in-situ charge storage concept in ISIS1 has been demonstrated in successful tests with X-rays and testbeams [89][88][90].

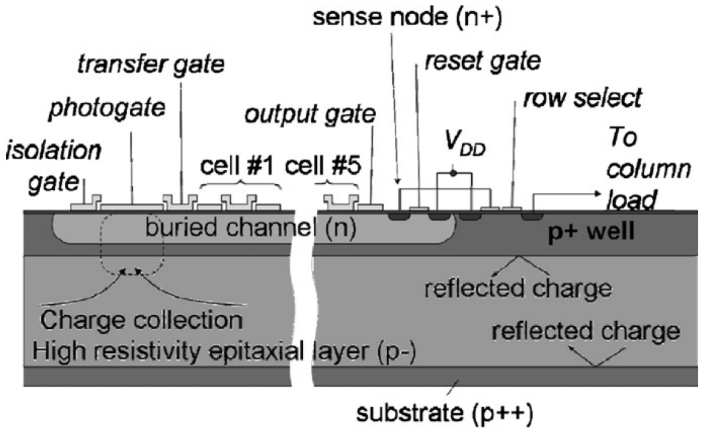

Figure 3.6: Schematic drawing of one ISIS1 pixel. The p^+ well is only present in the p-type sensors.[88]

Testing with ^{55}Fe

CCDs in vertex detectors are used to detect Minimum Ionization Particles (MIPs) while the absolute charge calibration can be conveniently performed with X-ray photons. X-ray photons of a few keV generate a large amount of e-h pairs in an almost perfect point-source. In other words, the charge generated from an X-ray photon can be confined to a single CCD pixel, and the uncertainty of the electron-hole numbers is simply given by statistics ($N \pm \sqrt{N}$ assuming Poisson distrubution). One of the most widely used X-ray sources is ^{55}Fe. An unstable ^{55}Fe atom will decay into a manganese (Mn) atom when the nucleus absorbs a K-shell electron. An electron from the L- or M- shell drops to fill the K-shell, emitting a 5.9 keV or 6.5 keV X-ray, corresponding to K_α or K_β lines. A 5.9 keV photon generates 1620 e^- in silicon contained within a diameter of 0.4 μm (FWHM) [76]. A 6.5 keV photon generates 1780 e^- but the K_β emission is much less probable, accounting for only 1/7 as much as K_α.

Under the illumination of 5.9 keV X-rays from a ^{55}Fe radioactive source, the signals collected by the ISIS1 devices with and without p-well are shown in Figure 3.7 [89]. The pedestal (larger peak in Figure 3.7) is fitted with a Gaussian and the σ value obtained from the fit characterizes the noise. The clear signal beyond pedestal shows successful charge transfer from the photogate through 5 memory cells. The difference in the signal rates between the basic and p-type sensors indicates that the p^+ well efficiently prevents the charge collection in the storage CCD cells.

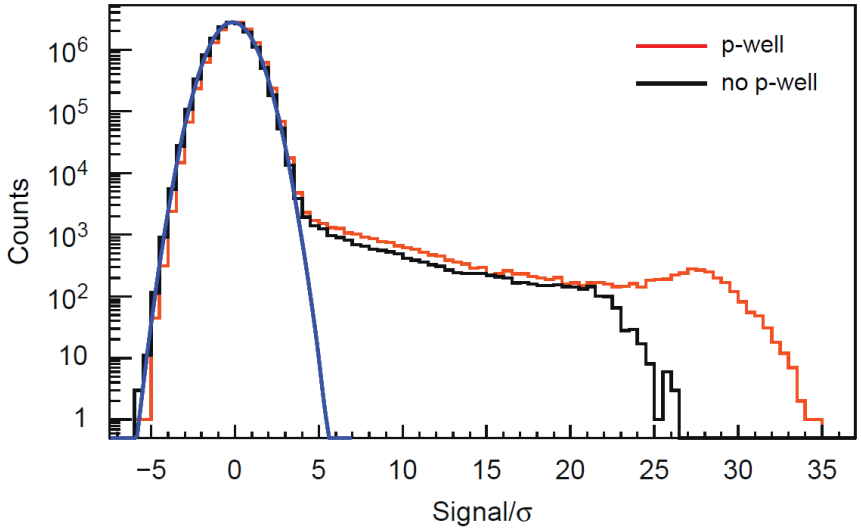

Figure 3.7: Distribution of the Fe^{55} signal scaled by noise for ISIS1 devices with and without p^+ well. σ is the Gaussian noise of the pedestal [89].

The charge shielding capability of the p-well is quantitatively illustrated in Figure 3.8 [90], which shows the ratio of $N_{photogate}/N_{ccd}$. $N_{photogate}$ stands for the ^{55}Fe hit rate as captured by the photogate and N_{ccd} stands for the rate of hits that is captured in the CCD storage cells. The abscissa is the bias on the photogate. The higher the photogate potential, the more charge is collected through the p-well due to the punch-through effect. As a result, the $N_{photogate}/N_{ccd}$ ratio increases with respect to the photogate potential for the p-type sensor. The high value of the ratio at high photogate potential shows that most of the charge is reflected by the p-well rather than directly collected by the CCD registers.

Tests with Testbeams

Five basic ISIS1 devices without p-well were tested with help of the EUDET telescope [91] using a 6 GeV electron beam at DESY. The devices were cooled to −20°C to suppress the shot noise. Hit pixels were combined into clusters. The amplitude distribution of cluster signals is shown in Figure 3.9. A seed pixel is defined to have the highest signal in a frame corresponding to a certain memory cell. Of all the pixels immediately next to the seed, the one with the highest signal is combined with the seed to form a cluster. The amplitude distribution of the seed signals is also shown. From the ^{55}Fe calibration one ADC count

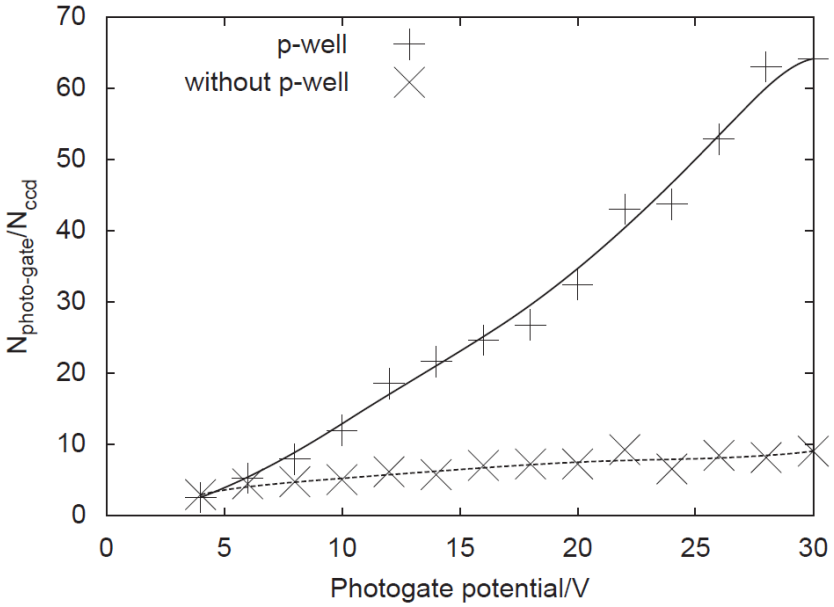

Figure 3.8: The ratio of the signal rate under the photogate to that under the storage cells for ISIS1 sensors with and without p-well [90].

approximately corresponds to $8e^-$. Fitting of the larger cluster signal peak with Landau distribution yield a most probable value of 3900 e^-, which is compatible with the 4000 e^- expectation for the 50 μm epitaxial layer. The smaller peak in the signal distribution is caused by charge collection inefficiency. The hit position was reconstructed with the η algorithm [92], and a position resolution of $11.6 \pm 0.1\,\mu$m was obtained in the direction corresponding to the 40μm pitch.

The double-peak structure in Figure 3.9 indicates an inefficient charge collection, so a method was devised to determine the inefficiency [88]. If the five ISIS1 devices are numbered along the beam direction, the third sensor is considered as the Device Under Test (DUT) while the first, second and fourth sensors are used for track finding. In correlation studies the fifth sensor was found misaligned from the others by approximately 300 μm in both directions and was not considered for this analysis. Once a track is reconstructed from the hits on devices 1, 2 and 4, a hit position on DUT is predicted. The analysis showed that only 34.9% of the tracks were found on the predicted pixel, which increases to 59.3% if the hit occurs in the predicted 5×5 pixel area. This considerable inefficiency is largely due to the ISIS1 geometry. The $160 \times 40\,\mu\text{m}^2$ pitch is large and asymmetric. If a MIP hits between

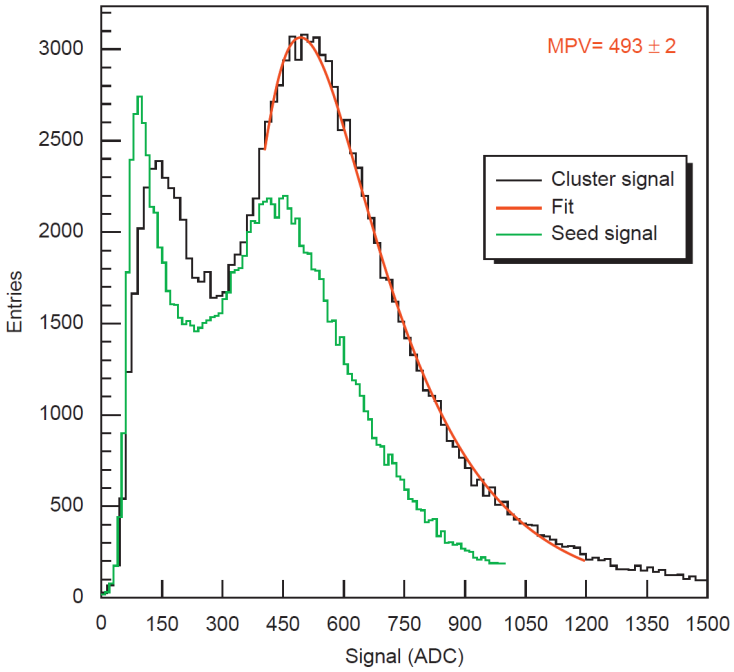

Figure 3.9: Cluster and seed signal distribution for ISIS1 under beam test [88]. MPV stands for the most probable value.

two photogates the generated charge can spread to many pixels and be collected by different photogates at the same time as sketched in Figure 3.10. For the "worst" hit position shown in the figure, which is in the middle of two photogates in both direction, the distance of the hit to each numbered photogate and the fraction of charge collected by each photogate is listed in Table 3.1.

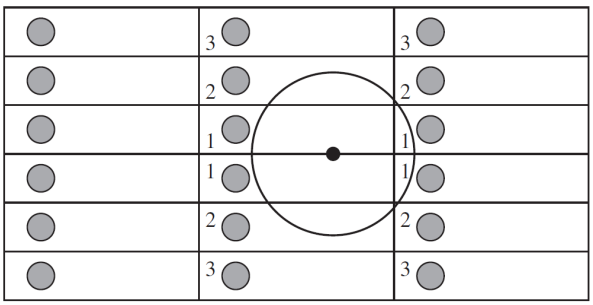

Figure 3.10: Sketch to scale of the photogate positions in ISIS1. A hit between the electrodes (filled circle) will share its charge over many pixels. The circle guides the eye to show that the distance from the worst case hit position to position 1 or 2 is not very different [88].

Photogate	Distance (μm)	Fraction (%)
1	82.5	6.7
2	100.0	5.5
3	128.1	4.3

Table 3.1: Distance between the worst hit position and numbered photogates and fraction of charge arriving at each photogate. The photogate numbering is shown in Figure 3.10 [88].

3.4 ISIS2

3.4.1 ISIS2 Design

With the success of the proof-of-principle sensors ISIS1, the second generation of the ISIS sensor, ISIS2, has been designed and produced. The ISIS2 sensors were manufactured in a 0.18 μm CMOS process by Jazz Semiconductor [93]. The small feature size of the process allows for 20 storage cells in every pixel, each with an area of $3 \times 5\,\mu m^2$ (comparing to the $20 \times 40\,\mu m^2$ storage cell on ISIS1).

Figure 3.11 shows a photo of a packaged ISIS2 sensor and its floor plan. The total size of the sensor is $5 \times 5 mm^2$. The sensor has 32 columns and 128 rows, divided into the upper and lower halves, with buried-channel and surface-channel reset transistor respectively. The columns are divided into four equal sections distinguished by different deep p^+ well variations. Outputs from 8 columns in each section are multiplexed. The row readout is performed using a rolling shutter principle, namely the signals are scanned across the frame row by row, rather than read out in parallel simultaneously.

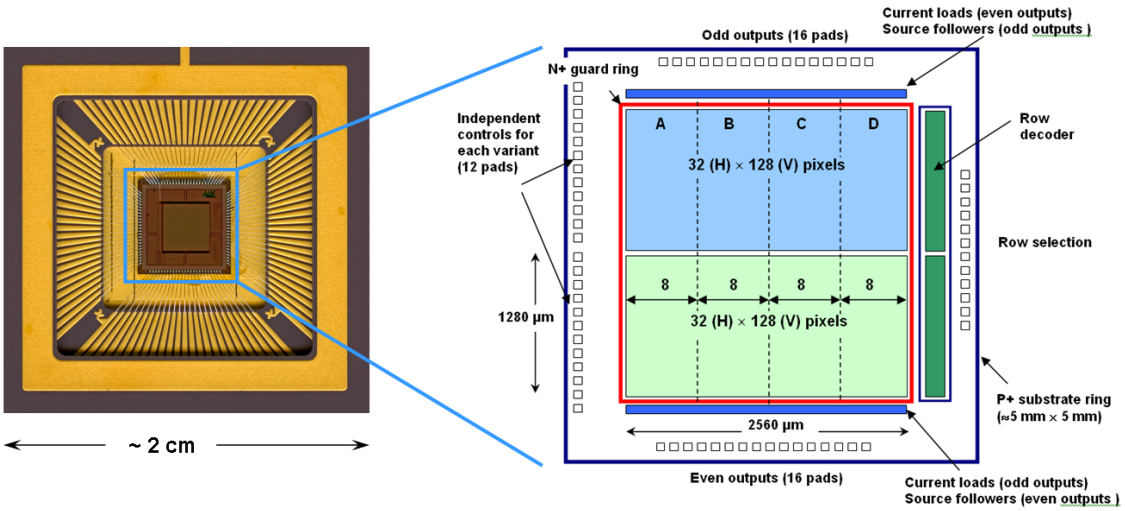

Figure 3.11: ISIS2 sensor wired-bonded in a ceramic package(left) and ISIS2 floor plan[94](right).

The ISIS2 imaging pixel size is $40 \times 20\,\mu m^2$ determined by relative locations of the photo gates, while the pixel layout size is $80 \times 10\,\mu m^2$ as illustrated in Figure 3.12. This

Name	Value (V)	Function
OD	5.0	Output Drain
RD	5.0	Reset Drain
RG	5.0	Reset Gate
OG	0.0	Output Gate
SG	4.0	Summing Gate
PG	3.0	Photogate
P1, P2, P3	3.0	CCD clocks
IG1, IG2	0.0	Isolation Gate

Table 3.2: The default bias settings for ISIS2 testing.

miniaturization is a major progress compared to ISIS1 thanks to the small feature size provided by the foundry. The staggered pixel layout results in a maximum distance of 21 μm to the nearest photogate for any hit, which should improve the charge collection efficiency comparing to ISIS1 (Table 3.1). Each pixel of ISIS2 contains a 3-phase CCD with 20 storage cells, a reset transistor, source follower and a row select transistor. There is a charge injection input next to the photogate and this controlled charge injection is useful for testing. All clock and bias signals are shared between all pixels except the Summing Gate (SG) and Row Select (RSEL) signals, which can be controlled by a separate transfer gate at the row level. A diagram of the pixel structure described above is shown in Figure 3.13. Typical bias values are listed in Table 3.2.

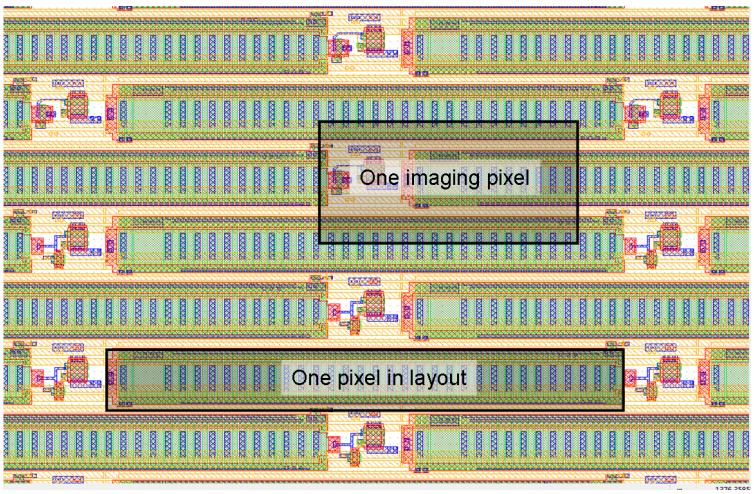

Figure 3.12: ISIS2 pixel layout[95]. An $80 \times 10\,\mu m^2$ layout pixel and a $40 \times 20\,\mu m^2$ imaging pixel are shown shadowed.

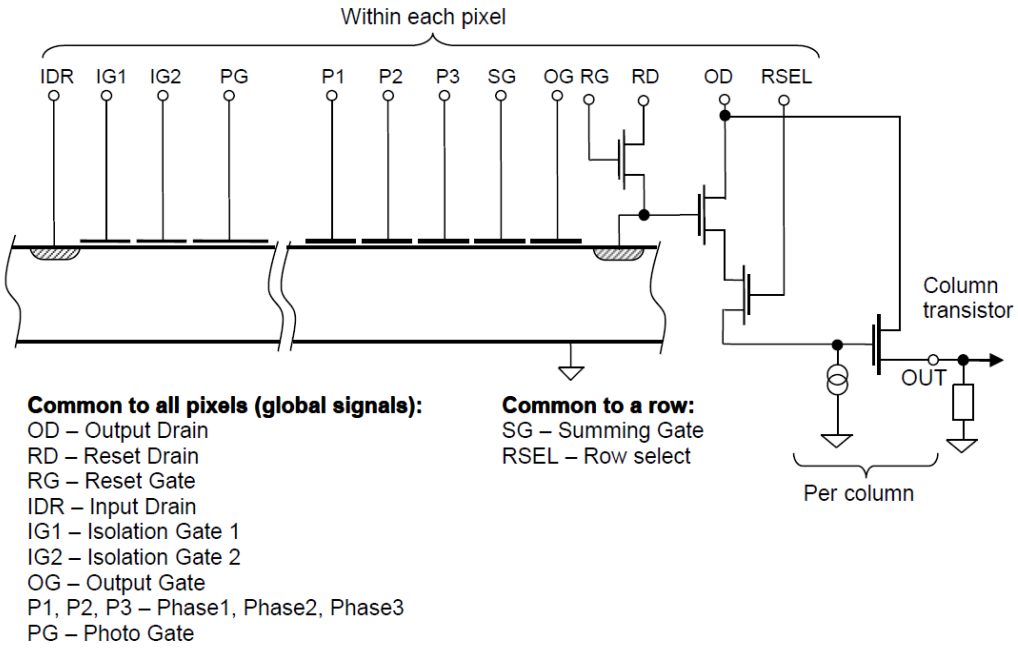

Figure 3.13: Diagram of the ISIS2 pixel.[94]

The separation of the buried channel and the epitaxial layer with the deep p^+ implant is another improvement with respect to ISIS1; this is only possible in a modern CMOS process. Figure 3.14 shows part of the cross-section of an ISIS2 pixel under the photogate. The opening of the deep p^+ implant is shown (not to scale) through which the deposited charge is collected. In order to investigate properties of the deep p^+ implant, four sections of the ISIS2 chip were implemented with the following variations:

A No deep p^+ implant;

B Deep p^+ implant with the opening size equal to the photogate size;

C Deep p^+ implant with the opening size equal to the photogate size plus 0.25 μm on all four sides;

D Deep p^+ without the opening.

The fabrication process enables a range of additional ISIS2 variations which can be helpful in studying and optimizing the performance. These variations are listed below:

- Deep p^+ implant (as mentioned above);

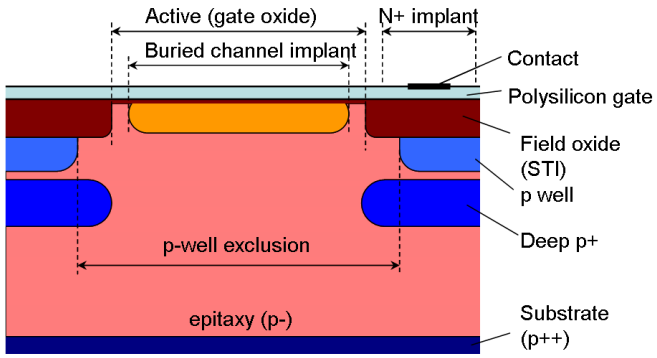

Figure 3.14: ISIS2 pixel cross-section under the photogate[94]. See text for details.

Pixel Type	Reset Transistor	Gate Length	Gap between Gates
1	Buried Channel	0.75	0.25
2	Surface Channel	0.75	0.25
3	Buried Channel	0.77	0.23
4	Surface Channel	0.77	0.23
5	Buried Channel	0.73	0.27
6	Surface Channel	0.73	0.27
7	Buried Channel	0.71	0.29
8	Surface Channel	0.71	0.29

Table 3.3: ISIS2 pixel variants. The unit for the gate length and the gap between the gates is μm.[94]

- Reset transistors implemented in surface channel or buried channel;
- Different CCD gate and gap width (summarized in Table 3.3);
- Wafers implanted with different doses at the surface to create the buried channel.

3.4.2 Experimental Setup

A block diagram of the experimental setup for the ISIS2 testing is shown in Figure 3.15. The packaged ISIS2 sensor is mounted on a customized motherboard (Figure 3.16) which provides all bias voltages and timing signals to the sensor. The motherboard also amplifies the analogue output with a total gain of 3. The power and biases for the motherboard are supplied by three Agilent 6700B power units. A timing sequencer BVM2 developed by

the LCFI collaboration[96] provides all clocking and triggering signals for the motherboard. The BVM2 obtains the master clock from a Tektronix AFG3102 signal generator. Another Tektronix AFG3102 generator triggered by the BVM2 is used to send a charge injection signal to the motherboard when needed. The output from the motherboard passes through a custom-made amplifier with adjustable gain, voltage offset and bandwidth filtering capabilities. The amplified and filtered output is sent finally through an Agilent MSO6104A oscilloscope into a 4-channel 14-bit ICS-554 analogue-digital convertor (ADC). The ADC receives triggers from the BVM2 and uses a 100 MHz internal clock. Most of the equipment is placed in a VME crate as shown in Figure 3.17.

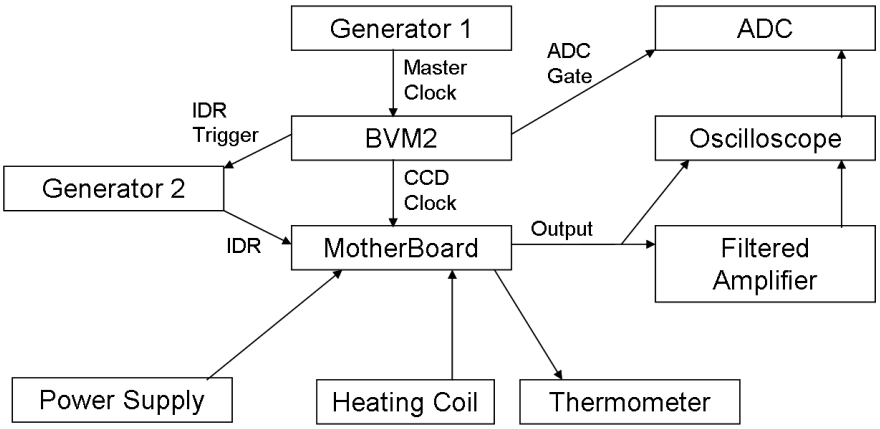

Figure 3.15: Block diagram of the ISIS experimental setup.

The motherboard is mounted in a black plastic box as shown in Figure 3.16 to protect it from visible light. A small hole is cut in the lid at the position right above the sensor to enable X-ray illumination with an ^{55}Fe radioactive source. The source is held in a collimator mounted above the hole. The box is placed in a Frigidaire freezer to provide necessary cooling. Nitrogen is piped into the box to purge the air so as to avoid condensation on the sensor. The motherboard has a thermal resistor and the temperature is monitored by connecting to a custom-made temperature control box. In addition, a Hanna digital thermometer is placed in the freezer to monitor the ambient temperature of the motherboard. When heating is needed, two heating resistors are glued to the diagonal corners of the ceramic ISIS sensor package. The resistors are connected to an external voltage source.

All the instruments providing the timing and biases are controlled by LabVIEW software[97].

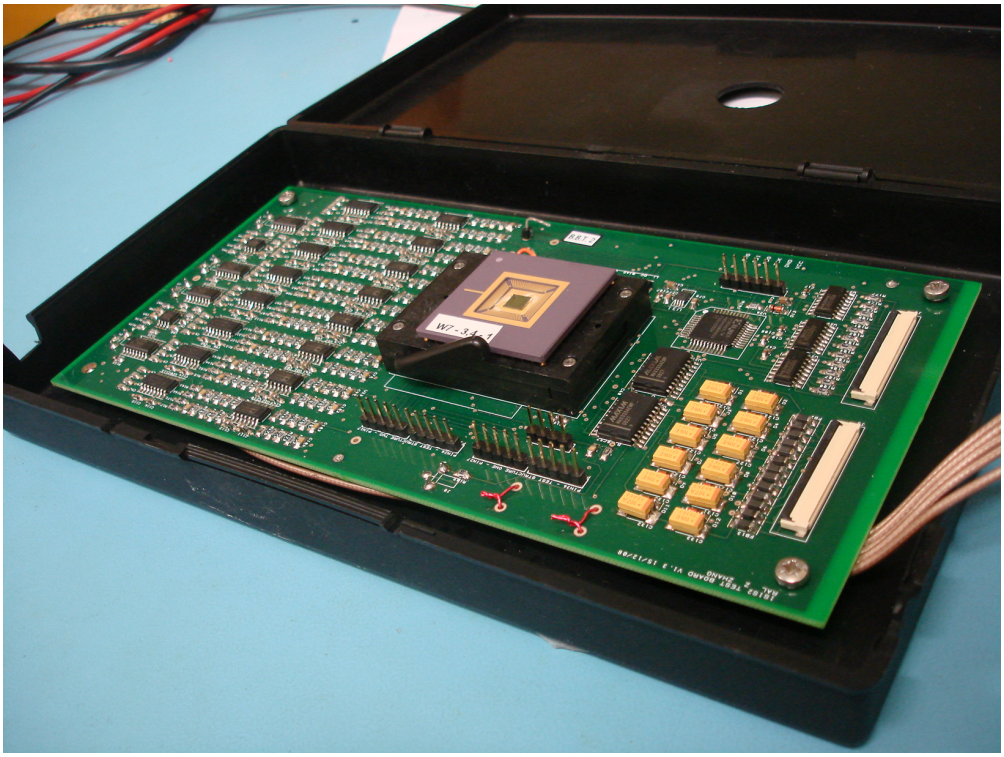

Figure 3.16: Photo of a packaged ISIS2 sensor mounted on the testing motherboard.

A sequence control GUI is used to define parameters of the clocking of the CCD and other gates. The sequence is written in time units, while each unit is equal to 1 over the frequency of the master clock. So for a specific sequence, its actual length can be controlled by varying the master clock frequency.

A diagram of typical ADC output is shown in Figure 3.18, which also illustrates the Correlated Double Sampling (CDS) technique applied in the data analysis to eliminate reset noise. The reset noise is induced on the sensor node during the reset. It is caused by the thermal noise generated at the reset transistor and sometimes is also called the kTC noise. The two plateaus marked as L1 and L2 in Figure 3.18 stand for the level before (reference level) and after (signal level) the charge transfer to the output node. Given that there is no reset in between, both levels suffer the same reset noise. The difference between the reference level and signal level is recorded rather than the absolute value of the signal level because the reset noise cancels out for the difference. The value of the reference level is taken by averaging two points (A1 and A2) while the signal level is obtained by averaging two points B1 and B2 separated by the same distance (L1 = L2).

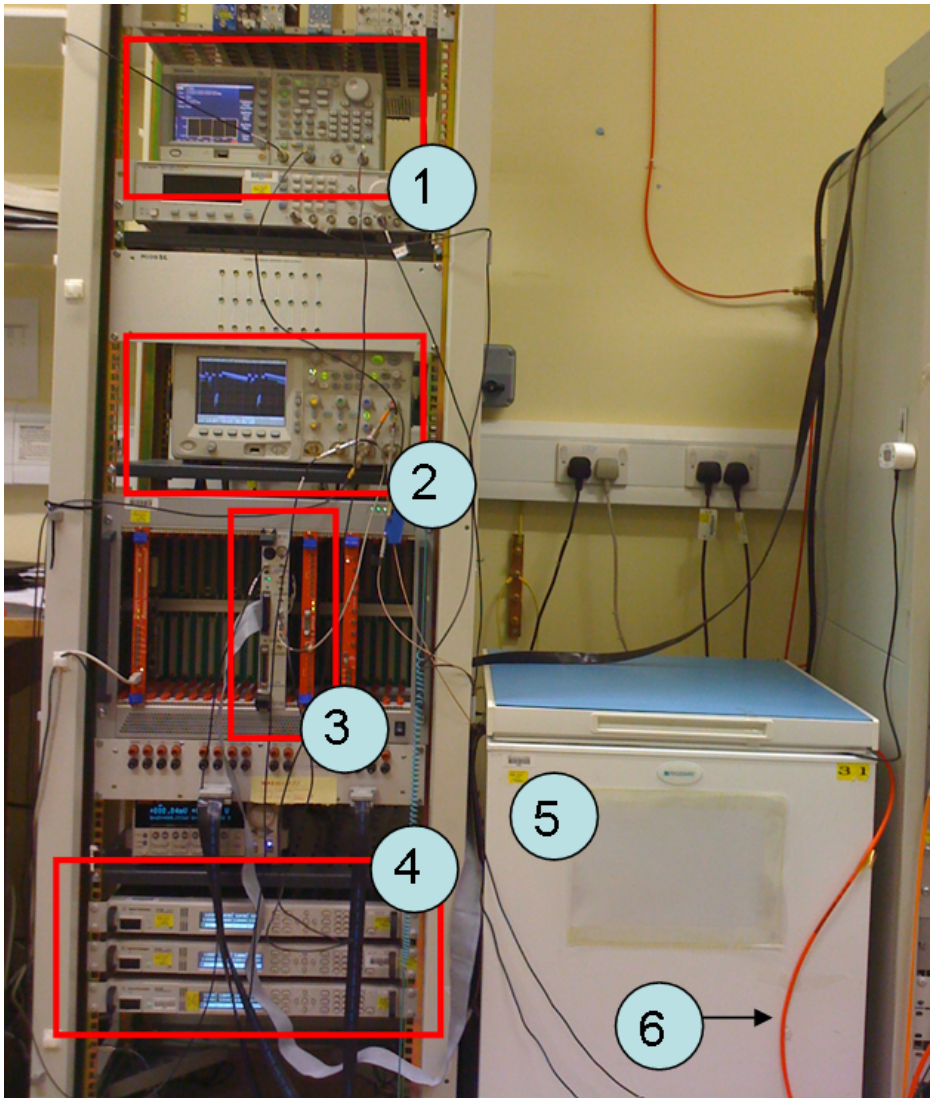

Figure 3.17: Photo of the VME crate and some apparatus in the experimental setup: (1) Tektronix AFG3102 signal generator; (2) Agilent MSO6104A oscilloscope; (3) BVM2 timing sequencer; (4) Agilent 6700B power supplies; (5) Frigidaire freezer; (6) Nitrogen pipe.

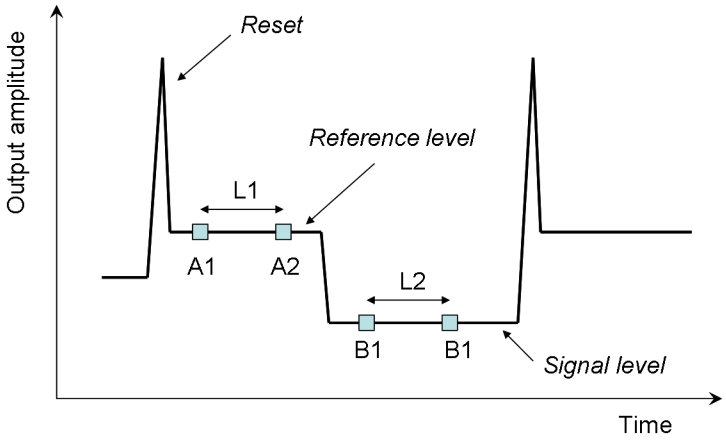

Figure 3.18: Illustration of the Correlated Double Sampling technique. Note the signal level is lower than the reference level because the charge collected is negative.

3.5 Study of ISIS2 Test Structure

A simple test structure, as shown in Figure 3.19, was included on the same ISIS wafer. It is similar to the ISIS2 pixel in the main array except for the absence of the storage CCD cells. The charge generated in the buried channel is collected at the photogate (PG), then transferred to the summing gate (SG), eventually through the output gate (OG) to the output node (Node).

This structure allows us to establish the optimum operation point of the ISIS pixel before studying the full array. Over half of the test structure area is taken by the $4 \times 5\,\mu\mathrm{m}^2$ photogate. The small size of the output node results in its small capacitance, hence a large charge to voltage conversion factor and potentially a very low noise. On the other hand the small size together with the tapered shape from the output gate (OG) to the output node could complicate charge transfer between the two and also means that the edge effects and 3D fringing fields can become important.

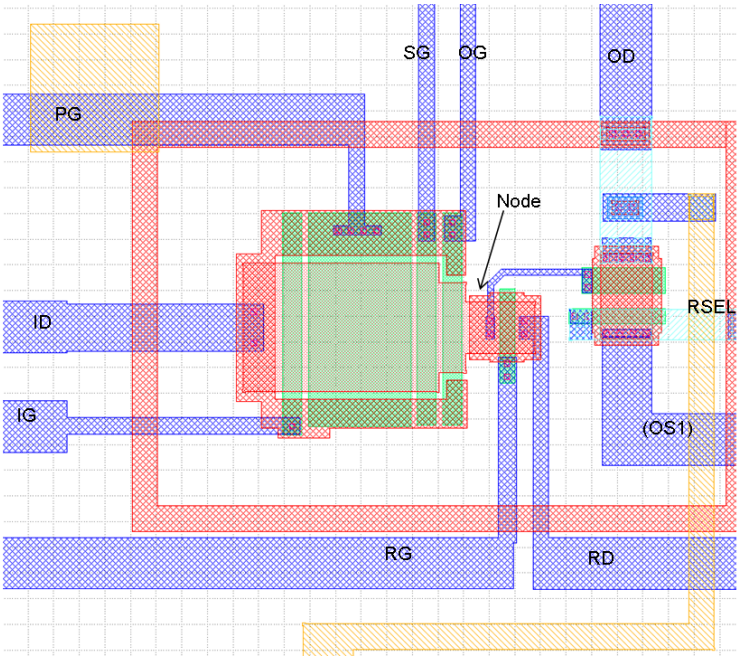

Figure 3.19: ISIS2 test structure[95]. The initials in the figure stands for: ID - Input Drain; IG - Input Gate; OS1 - Test structure 1; RSEL - Row Selector; the rest of them have the same meaning as in Table 3.2.

The test structure is also divided into several variations, mainly by the size of photogate.

In all the results below, the test structure with $4 \times 5\,\mu\text{m}^2$ photogate is used.

3.5.1 Fringing Effect

It turns out that the fringing effect is important because the voltage on the output gate (OG) is pulled up by the constant 5 V bias on the neighbouring output node, and is not equal to the voltage applied to OG due to this effect. It is found that the OG bias should be set to below 0 V otherwise the charge stored on the summing gate (SG) will leak from the summing gate directly into the output node. This is illustrated in Figure 3.20 (b). The OG bias value for a typical CCD could be above 1 V. Figure 3.20 (a) shows a quantitative example of such behaviour [98]. The sensor was illuminated with LED light and then the voltage on the photogate was lowered while the voltage on the summing gate was kept high. The charge collected should be temporarily held within the summing gate if the OG functions properly. The line labeled "SG" shows the charge kept under the summing gate and "PG" shows the charge that leaked through OG to the output node. It is clear that for a low enough OG voltage the charge can be transferred as expected while at high OG the transfer is severely hampered by effects of the fringe field and happens prematurely.

3.5.2 Readout Speed

Another unexpected feature discovered in ISIS2 is the highly resistive polysilicon gate. The gates were left unintentionally undoped, however it turned out that the sheet resistance of undoped polysilicon is much higher than pure undoped silicon by orders of magnitude [95]. The immediate result is that the time constant to charge up the gate to a certain voltage is substantially longer than expected, and a charge transfer between two neighbouring gates typically takes up to a few milliseconds. The time constant also varies with the temperature. From Figure 3.21 which shows the voltage on the output node it is clear that the response at lower temperature is much slower.

The temperature dependence has been studied to determine the optimal conditions. Fig-

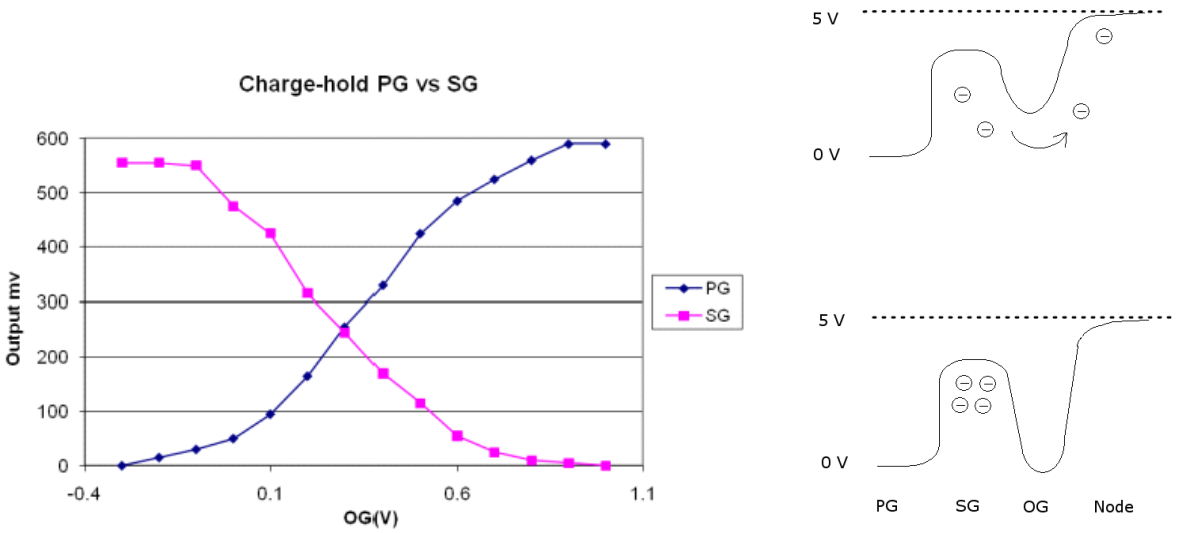

(a) (b)

Figure 3.20: (a) Charge that can be held under the summing gate(SG) and that leaks to the output node(PG) at different OG voltage [98]; (b) Diagram of the charge leaking to the output node (upper) and charge held in the summing gate (lower) if the OG voltage is low enough.

ure 3.22 shows the fastest readout allowed for different temperatures by measuring the injected charge. The y axis is the output amplitude change due to charge injection to the photogate and the x axis is the frequency of the master clock, a measure of time for the charge transfer. The charge injection is enabled with the IDR structure as shown in Figure 3.13. The charge injection process is similar to the transfer from the summing gate to the output node, except that the order is inverted. The voltage on the input gates (OG1, OG2) is always set to zero. When a positive voltage is applied on the IDR certain amount of charge is generated; and when the IDR voltage is lowered to zero, these charge are pushed through the input gates to the photogate. The y value is only determined by the amount of charge injected if the charge is fully transferred. Therefore the drop in the output amplitude at higher frequency means incomplete charge transfer, caused by the slow operation of the gates. The curve for room temperature (26.8°C) starts to drop beyond 2 MHz, corresponding to a period of 2.5 ms for transfer from the photogate to the summing gate. For low temperatures below 0°C the turning point is approximately 0.5 MHz, corresponding to time of transfer of 10 ms.

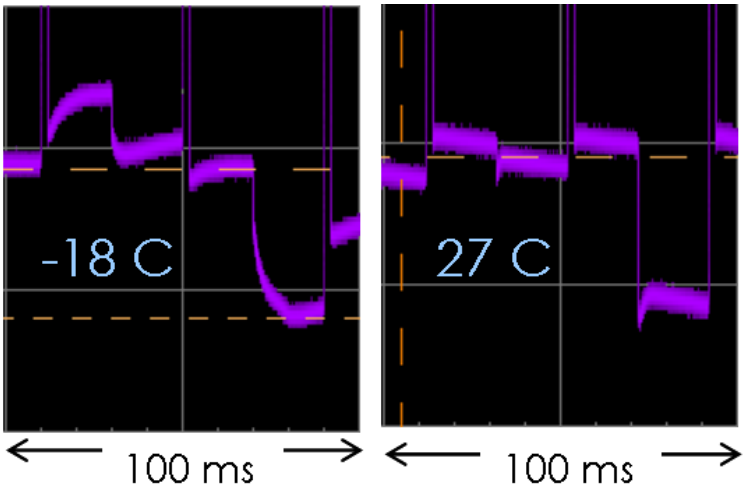

Figure 3.21: Signal output at −18°C and 27°C.

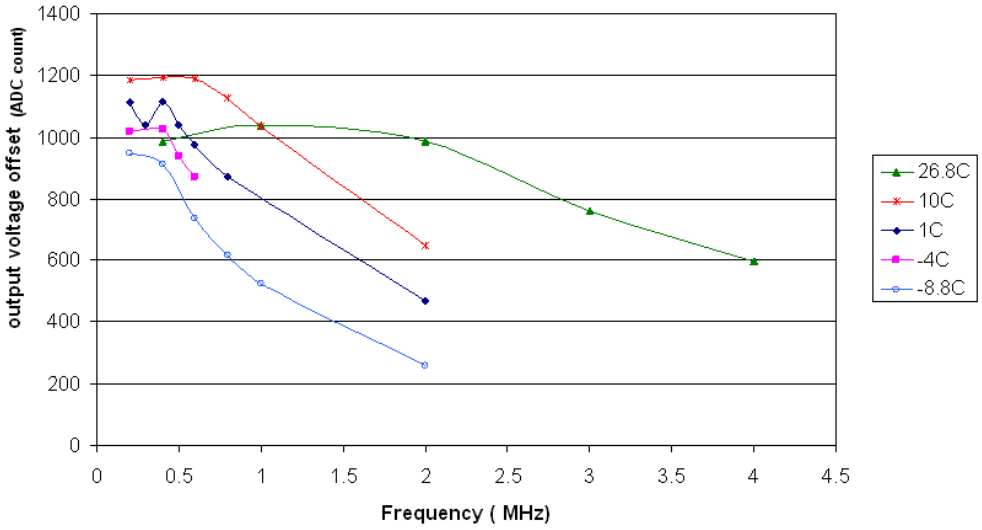

Figure 3.22: Change of the output amplitude due to charge injection, as a function of the master clock frequency for different temperatures. The turning point shows the fastest readout allowed for different temperature, see text.

Though the time of operation was largely limited by the charge transfer speed, it was also found that the charge survives up to a few seconds in the buried channel of the sensor which enables us to investigate charge transfers in the CCD structure and to study the charge transfer efficiency (CTE), as described in Section 3.6.2.

3.5.3 X-ray Calibration

The absolute calibration of the signal is performed using the 5.9 keV X-ray source as introduced in Section 3.3.2. The sensor was illuminated under an ^{55}Fe radiative source. The output amplitude was digitized by the ADC and the CDS technique was used. A data set accumulated for approximately 10 hours at the temperature of 31 °C is shown in Figure 3.23. The right peak in the figure is the signal peak and the left one is the pedestal peak corresponding to the case when no X-ray was registered. The valley in between corresponds to the charge from ^{55}Fe signals shared between pixels. Both peaks are fitted with Gaussian distributions, and the distance between the mean values corresponds to 1620 e^- generated by the K_α X-ray photon. The σ value of the pedestal Gaussian is used as equivalent noise. It gives a calibration of 4.182 ± 0.005 ADC counts per e^-. Given the gain of the sensor and of the test board, it can be determined that the output node has a responsivity of $21.3 \pm 1.1 \mu\text{V}/e^-$, in agreement with the design value.

It is possible to estimate the charge transfer efficiency (CTE) on the test-structure using the X-ray source. The outputs from two cases are compared: (1) direct X-ray hits on the output node with other gates unclocked and (2) hits collected on the photogate and transferred through the summing gate to the output node. The ratio of the charge in case (2) to case (1) is the CTE, shown as in Table 3.4. Only the output node results in case (1) can be used for the absolute calibration since there is no loss of charge in transfer. This measurement was repeated at room temperature and low temperature, and the CTE estimations agree well in both cases. This relatively low CTE about 94% (comparing to typical buried-channel CCDs) was most likely caused by the tapered shape of the transition from the summing gate to the output node. The noise for both cases is also listed in Table

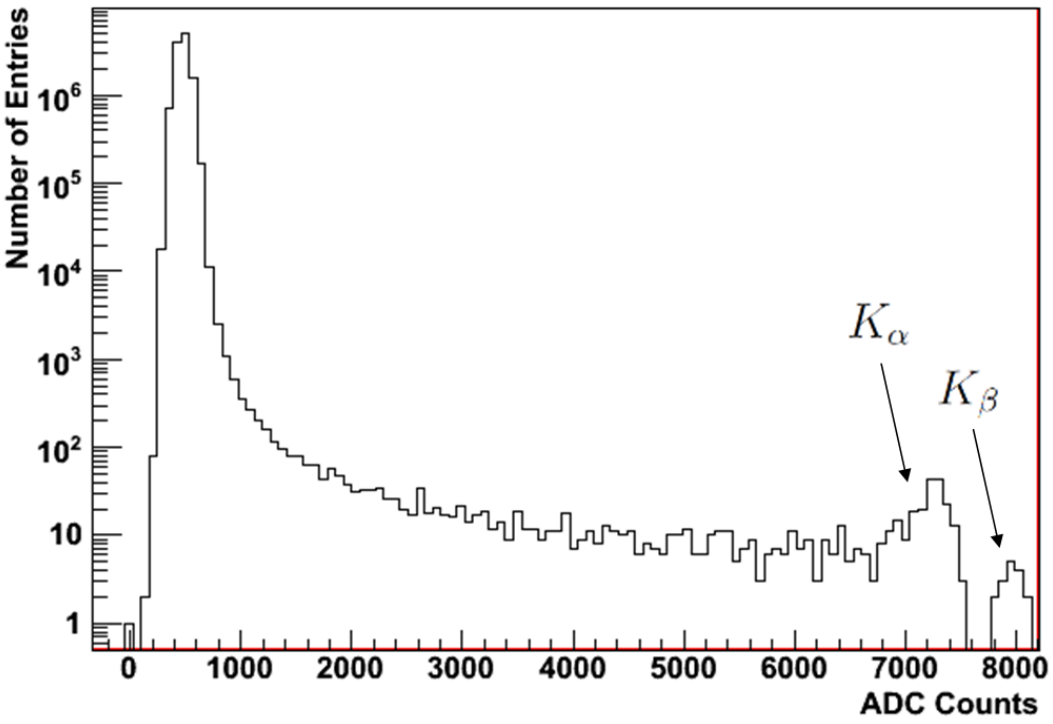

Figure 3.23: Amplitude spectrum of ^{55}Fe X-ray source used for absolute calibrations of ISIS2 sensor.

Temperature	−10°C	31°C
Peak seperation of Output Node(ADC counts)	6810	6799
Peak seperation of Photogate(ADC counts)	6417	6423
CTE	(94.2± 0.2)%	(94.5±0.4)%
Noise of Output Node (e^-)	20	14
Noise of Photogate (e^-)	27	66

Table 3.4: X-ray calibration and CTE on test-structure.

3.4. The noise is low for the output node, which allowed us to resolve the K_α and K_β signals as indicated by arrows in Figure 3.23. The larger noise on the photogate is due to the longer integration time and therefore additional contribution from the shot noise. Its rapid increase with temperature is also typical for shot noise.

3.5.4 Well Capacity

The well capacity of the sensor is measured by observing the signal saturation. The signal on the sensor can be induced by dark current, external light source (LED for example) or injected charge, which all cause saturation at high signal level. Figure 3.24 shows the output signal as a function of integration time for different summing gate bias. For short integration time, the output shows linear dependence due to the dark current accumulated at the photogate. The slope is dependent on temperature. This plot is obtained at 30°C, and for similar measurements at lower temperatures a more gentle slope is observed. The constant output at long integration time shows that saturation occurs when the accumulated charge reaches the well capacity of the summing gate. The summing gate has an area of $1 \times 5\,\mu\text{m}^2$, smaller than the $4 \times 5\,\mu\text{m}^2$ photogate, therefore a smaller well capacity. Figure 3.24 also shows that the well capacity of the summing gate increases with the voltage applied to it, which further confirms that the saturation happens on the summing gate rather than the photogate.

Measurement of the well capacity using charge injection is shown in Figure 3.25. The amount of charge is controlled by the IDR voltage (abscissa). The IDR value has to be

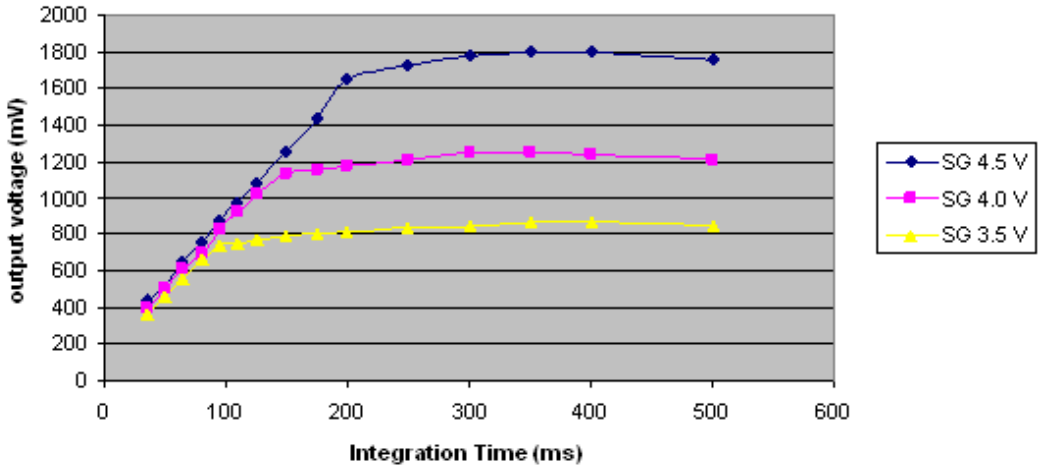

Figure 3.24: Dependence of the output voltage on the photogate integration time.

Summing Gate bias (V)	Well Capacity ($10^3 e^-$)
3.5	2.1
4	7.2
4.5	15.0

Table 3.5: Well capacity of the ISIS2 summing gate for different summing gate bias. The uncertainties for the well capacity measured can be estimated to $76e^-$.

over a certain threshold for the charge injection to function, in this case the threshold being approximately 3 V. Once over the threshold, the amount of charge injected is proportional to IDR voltage until the charge saturates the well capacity of the summing gate. Note that the output amplitude levels at saturation are very similar in Figure 3.24 and Figure 3.25. From the difference between the output amplitude at saturation and that below IDR threshold it is easy to derive the amount of charge needed to saturate the well capacity (charge = output amplitude / ADC count number per e^-), given absolute calibration of output amplitude in electrons (Section 3.5.3). The calculated value for different summing gate biases is given in Table 3.5. It should be noted that this number is given as the lower limit of the well capacity because there is a considerable dark current accumulated on the photogate even when there is no charge injection at all. The well capacity is measured for the summing gate, but it also applies for the CCD storage cells because the pitch size of the CCD gates is the same as the summing gate ($1 \times 5\,\mu\mathrm{m}^2$).

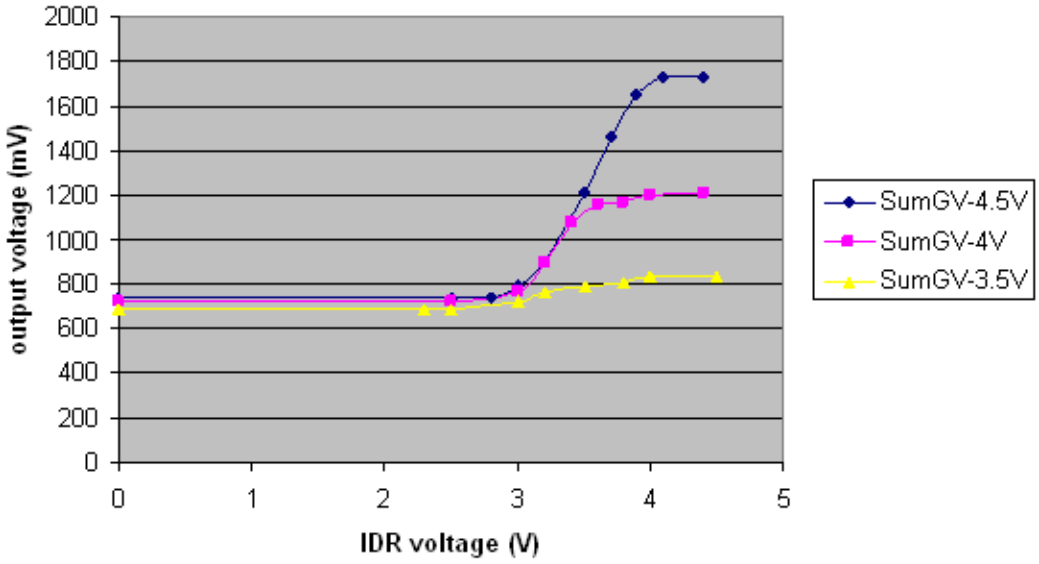

Figure 3.25: Dependence of the output voltage on the IDR voltage.

3.6 Study of ISIS2 Main Array

Studies of the test structure described in the previous section allowed us to optimize the operational parameters of the ISIS2 sensor and to perform tests of the full array. An example of successful charge transfer in an ISIS2 pixel from the main array is shown in Figure 3.26. The oscilloscope traces with and without charge injection are shown. The difference emphasized with the red circle is due to the charge injected to the photogate. The charge accumulated in the photogate is transferred down through 20 storage cells to the summing gate, and eventually over the output gate to the output node where it is converted to voltage. The scope trace records the whole period in which the injected charge propagates through the pixel. The reset drain is enabled once before every transfer from the summing gate to the output node in order to clear the charge on the node. If we number the storage cell next to the photogate as the first, the change of amplitude after the first reset corresponds to the charge collected on the 20th storage cell. Similarly the signal after the second reset is the charge from the 19th cell transferred through the 20th to the output, and so forth. The linear accumulation of leakage current on the twenty CCD registers is clearly visible.

The scope trace above is taken from a continuous readout of a pixel in a fixed row rather than a whole frame with rolling shutter readout switching among the rows. The rolling

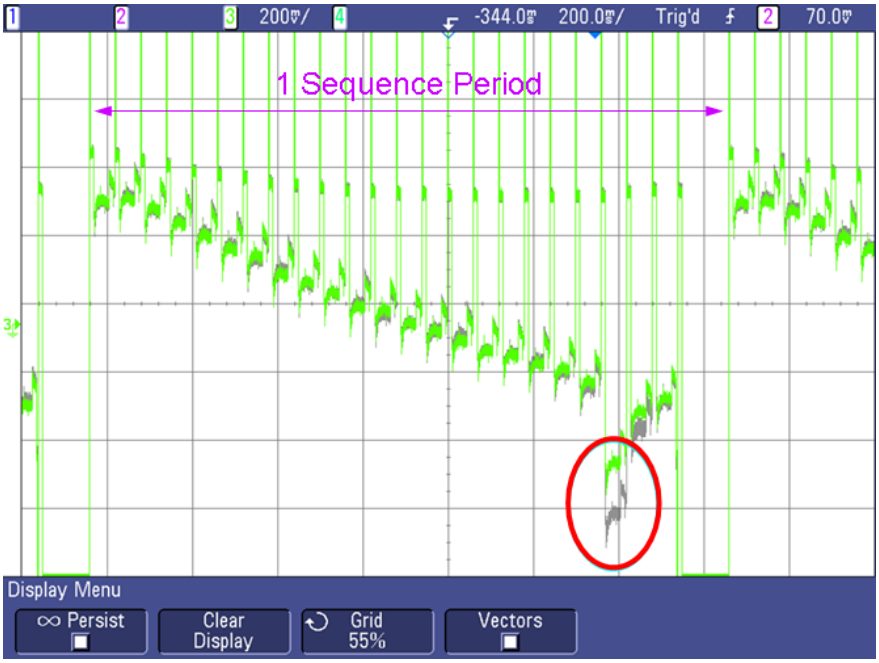

Figure 3.26: Oscilloscope trace of a successful charge transfer in the ISIS2 main array.

shutter readout is unfortunately not working for the ISIS2 due to a design mistake in the row logic which prevents selection of a single row.

3.6.1 Operation Optimization

The slow readout speed mentioned earlier means that it takes a long time (up to seconds) to read out a full pixel, during which the dark current could cause a considerable shot noise and, more worryingly, could saturate the well capacity. A lot of efforts therefore have been directed to minimize the readout time. The most straightforward way of reducing the dark current will be to reduce temperature, but this will lead to higher resistivity of the polysilicon gates, hence even longer readout time. The following optimization study is done at the fixed temperature of $-5°C$. This temperature is chosen as a trade-off between low shot noise and fast readout speed.

Charge injection was again used to determine the fastest readout allowed. The well capacity is a fixed value, determined by the potential applied to the gate (as discussed in Section 3.5.4). Ideally it is equal to the amount of charge injected that causes the saturation of output. However due to the leakage current accumulated on the photogate as well as on

the CCD storage cells, the charge injected at saturation is always less than the well capacity of the CCD gates. The dark current accumulation is proportional to the integration time (as shown in Figure 3.24), therefore the faster the readout, the less charge is collected due to dark current, hence the more charge injection is needed to saturate the well capacity. The difference of the output between cases with saturation and with no charge injection should increase as the readout speeds up. This tendency continues until the readout speed limit is reached, starting from when the charge is transferred only partially due to slow operation of the gates. Beyond the threshold speed, the output at saturation should decrease as the speed increases, because more charge will be left in the CCD cells, untransferred.

Figure 3.27 shows the measurement based on the idea above. The x-axis is the IDR voltage which determines the amount of charge injected, and the y-axis is the output amplitude subtracted by the amplitude for the case without any charge injection. The height of the plateaus indicates the amount of charge injected to saturate the well capacity. Various frequencies of master clock are presented. It is observed that for frequencies above 800 kHz the maximum height of the plateau is reduced, which indicates incomplete charge transfer, therefore the 800 kHz master clock is the fastest readout allowed at this temperature. This is equivalent to a period of 2.6 s for charge transfer from the photogate to the output node.

The optimization above considers a uniform sequence, namely the transfer time between each pair of neighbouring gates is the same. This is justified for the case of the CCD storage cells, since each gate has exactly the same geometry. But if we look into the pixel layout (Figure 3.12), the 2 μm wide output node is much narrower than the summing gate and output gate, and the tapered shape could become the bottleneck for faster charge transfer. If this is the case, the time sequence could be modified to further decrease the readout time by allowing less time for the transfer from the photogate throughout 20 storage cells while keeping the transfer time between the summing gate to the output node unchanged. Figure 3.28 shows the optimization based on this idea. The axes bear the same meaning as in the previous paragraph. Various percentages by which the transfers through the 20 storage cells are compressed are shown. Comparing to the original sequence compressing the transfer by

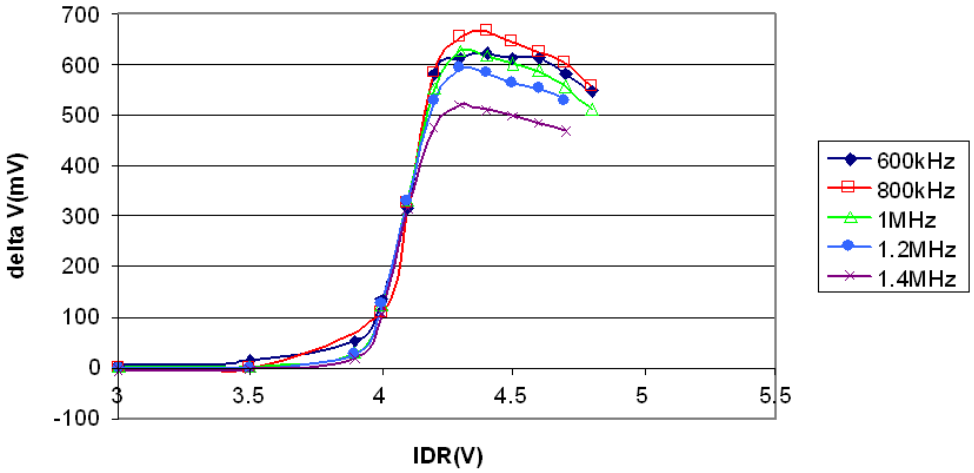

Figure 3.27: Readout time minimization by increasing the master clock frequency. The y-axis is the output amplitude offset by the amplitude when there is no charge injection. Different curves corresponds to various frequencies of the master clock.

up to 15% indeed improves the readout speed while maintaining the same CTE. The sequence compressed by 20% already shows a drop in the output amplitude at saturation, indicating incomplete transfer through the CCD registers. Therefore compressing the transfer time between storage cells to 85% while keeping the summing gate to output node unchanged will further reduce the total period of transfer to 2.2 s.

3.6.2 Charge Transfer Efficiency (1)

The Charge Transfer Efficiency (CTE) is defined as the fraction of charge that is transferred successfully from one CCD pixel to the next. Sometimes charge transfer inefficiency CTI which equals to 1 − CTE is also used for convenience. It is an important measure of CCD performance especially for large area CCDs. Modern CCDs can reach a CTI of the order of 10^{-5}. Whether such efficient transfer can be achieved is not a major concern for ISIS2 because the number of transfers is small, but we do need to make sure there is no substantial loss in the transfer from the photogate through 20 storage cells. Had the CTI been 5%, only one third of the charge collected at the photogate would make its way to the output node, which is unacceptably low.

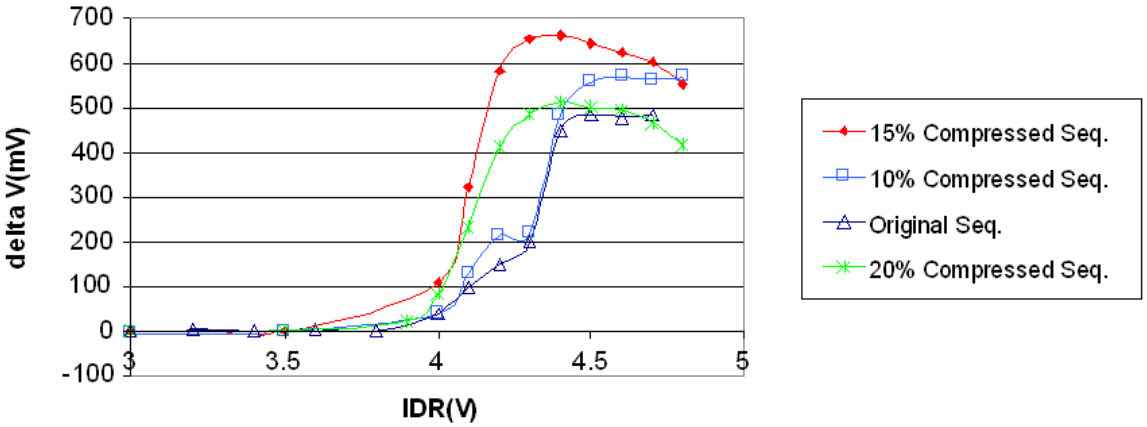

Figure 3.28: Readout time minimization by compressing the sequence without changing the transfer time from SG. The y-axis is the output amplitude offset by the amplitude value when there is no charge injection. Various percentage by which the transfers through 20 storage cells are compressed are shown.

In order to measure the CTE in the CCD registers two different methods are used. This section will describe a method using charge injection, while another method making use of an ^{55}Fe radioactive source is described in the next section. Three-phase CCD registers are used in the ISIS2 storage cells, therefore the charge can be moved in both directions. The first method of CTE measurement uses charge manipulation and compares the two cases as illustrated in Figure 3.29. In case (2) the charge injected to the photogate is first moved forward to the middle of the CCD, then backward for n cells, then forward again to the output node. In case (1) charge always moves forward, but will be paused in the middle simply to keep both sequences at the same length making sure that the leakage current effects are the same. Therefore there will be $2n$ more transfers in case (2) than in (1). Assuming that the charges initially injected are S_0 and the outputs measured in the two cases are S_1 and S_2, it is derived that:

$$\begin{aligned} \frac{S_2}{S_1} &= \mathrm{CTE}^{2n} \\ &= (1-\mathrm{CTI})^{2n} \\ &\simeq 1-2n\times\mathrm{CTI}, \end{aligned} \tag{3.1}$$

where CTI $\ll 1$ is the Charge Transfer Inefficiency. The statistical uncertainty of the CTE is estimated as:

$$\left(\frac{d\mathrm{CTE}}{\mathrm{CTE}}\right)^2 = \left(\frac{1}{2n}\right)^2 \times \left[\left(\frac{dS_2}{S_2}\right)^2 + \left(\frac{dS_1}{S_1}\right)^2\right] \tag{3.2}$$

where dS_2 and dS_1 stand for the statistical uncertainty of S_2 and S_1 in repeated measurements. It follows straightforwardly that a large number of transfers n will result in a small statistical error for the CTE. On the other hand the main systematic uncertainty of the measurement is caused by the temperature instability, so for large n the shot noise contribution to the uncertainty will be dominating. The measured CTE with its statistical uncertainty for different number of extra transfers n is given in Figure 3.30. Measurements for different n are consistent, giving a CTE of $98.9 \pm 0.4\%$. The sensor used is the type 4 (Table 3.3) with 0.23 μm gap between the CCD gates.

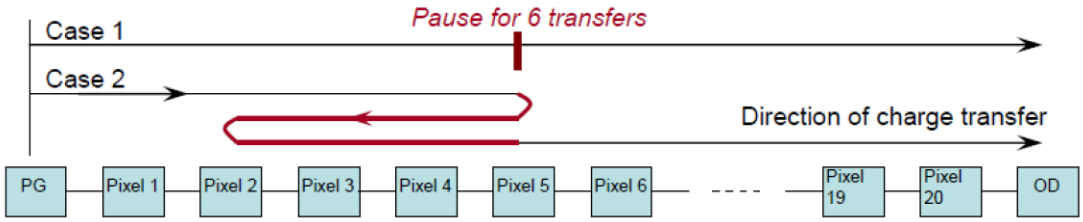

Figure 3.29: CTE measurement method using reversing of direction for the charge transfer in the CCD register.

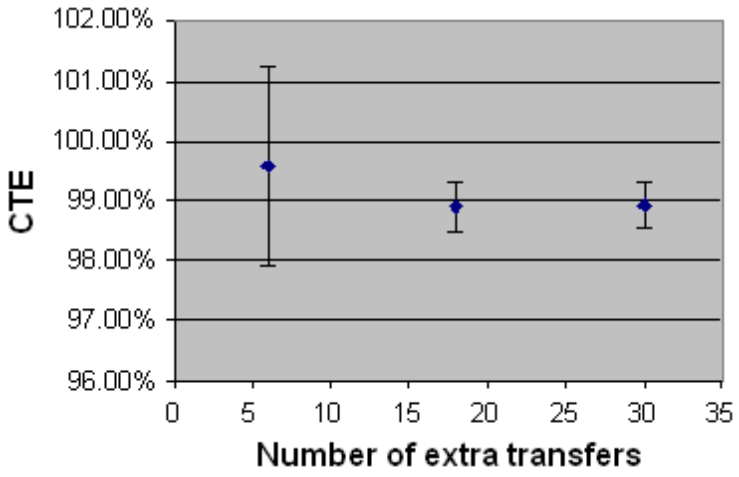

Figure 3.30: CTE versus number of extra transfers.

3.6.3 Charge Transfer Efficiency (2)

Another method to measure the CTE uses X-rays from a ^{55}Fe source. To understand the method, we consider the ISIS2 pixel is as one-dimensional CCD registers. If the initial charge package is S_0 (e.g. 1620 e^- in the K_α case) then after transfer through k pixels the charge left is

$$\begin{aligned} S_k &= S_0 \cdot \mathrm{CTE}^k \\ &= S_0 \cdot (1 - \mathrm{CTI})^k \end{aligned} \tag{3.3}$$

where CTI is the charge transfer inefficiency. Usually CTI $\ll 1$, so we can make an approximation that $(1 - \mathrm{CTI})^k \simeq 1 - k \cdot \mathrm{CTI}$. Then Equation 3.3 becomes

$$S_k = S_0 - S_0 \cdot \mathrm{CTI} \cdot k. \tag{3.4}$$

If we plot the charge S_k as a function of number of transfers k, then we will get a straight line with intercept S_0 and slope $-S_0 \cdot \mathrm{CTI}$. CTI can be obtained by dividing the absolute value of slope over S_0.

The photogate integration time is typically tens of milliseconds, a few percent of the readout time. When charge is transferred down the storage cells a lot of X-ray hits are also inevitably collected under the CCD gates. Therefore for this CTE measurement a challenge is to disentangle the hits on the photogate and those on different storage cells. A solution is to limit the X-ray illumination to the time interval when the charge is held at the photogate or at the targeted storage cell. Two measurements based on this idea are made at different setups. Zhang et al. [98] utilizes a moving ^{55}Fe source which is placed above the sensor when the charge is held on the cell being measured and moved away when the charge is transferred further. Figure 3.31 shows the X-ray signal as a function of number of charge transfers. From the linear fit a CTE of 99.26% is calculated.

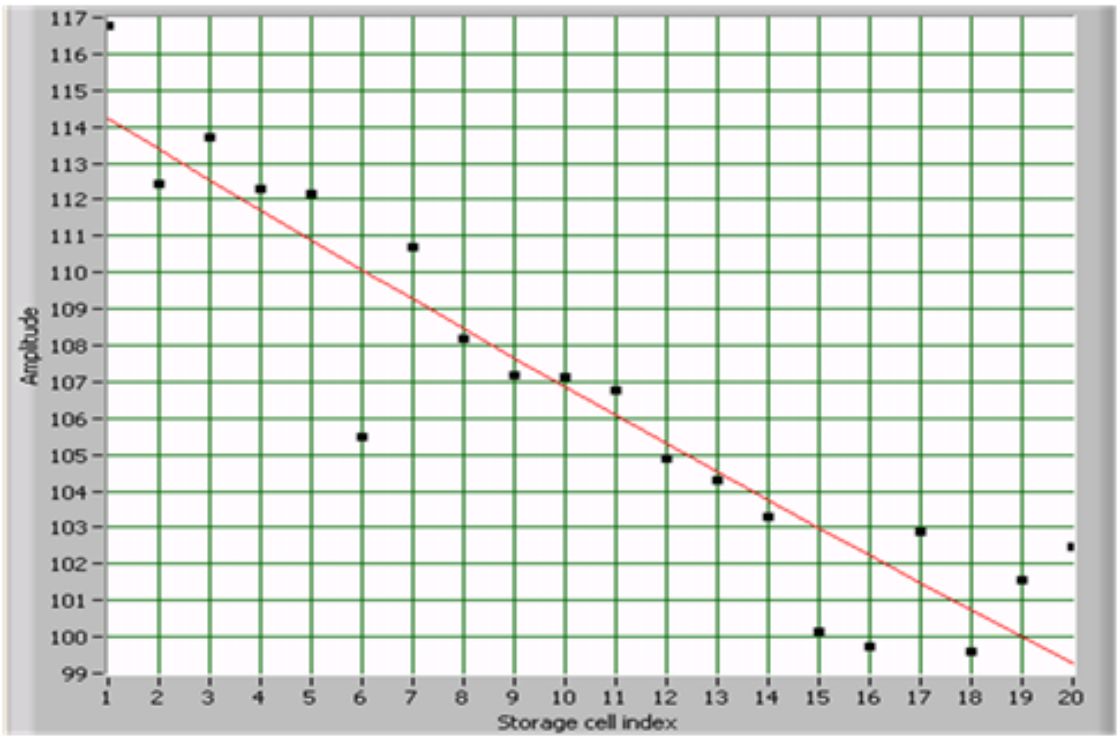

Figure 3.31: Position of ^{55}Fe signal peak versus number of transfers. This was obtained with a moving ^{55}Fe source [98].

Experimental Setup of the Shutter System

The other CTE measurement was made using a fast mechanical shutter between the radioactive source and the sensor. A Uniblitz LS6 shutter [99] with aperture diameter of 6 mm was used. An aluminium shelf was installed above the motherboard and the shutter was mounted right below the aluminium surface, see Figure 3.32. There is a hole in the aluminium surface to place the ^{55}Fe source holder. The distance between the shutter blades and the sensor is 12 mm and the source is 10 mm above the shutter. Specific properties of the lubricant used do not allow the shutter to function below 0 °C. The temperature of the Frigidaire Freezer is adjustable, but even at the highest temperature setting the ambient temperature around the working sensor is about -10°C. Therefore two 22 Ω resistors in series are glued to the aluminium shelf to provide extra heating. A voltage of 14.5 V is applied to the resistors. During operation the temperature of the sensor is stabilized at 6.5 °C and that on the shelf at 16.8 °C. The latter is closest to the temperature of the shutter, which is safely within its working range.

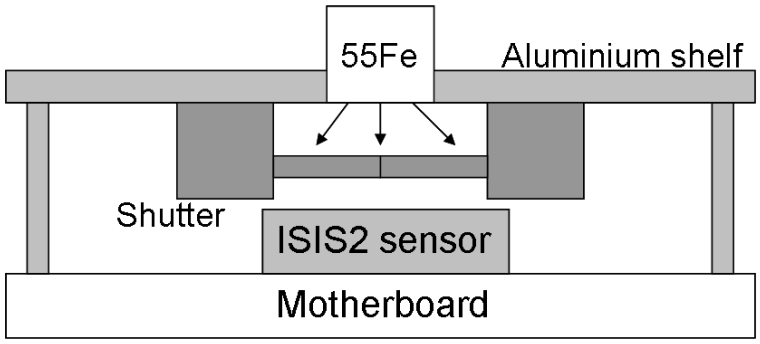

Figure 3.32: Setup of the shutter system (not to scale).

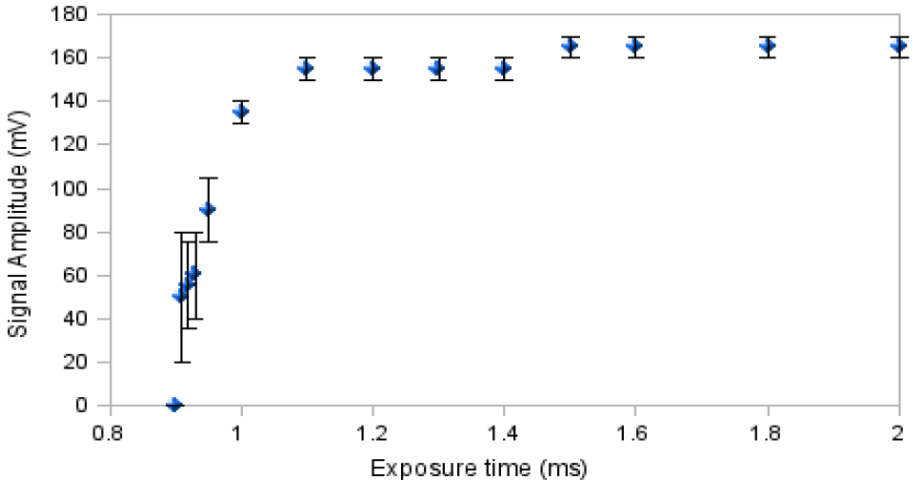

Figure 3.33: Dependence of the signal amplitude on the exposure time.

The operational properties of the shutter were studied to ensure its appropriate usage. The signal response to the shutter exposure time was measured to determine the minimum exposure time. The ISIS2 sensor is light sensitive, so optical light is used instead of X-rays from the ^{55}Fe source to gain higher signal rates. One end of an optical fibre is fixed above the shutter blades, and the other end is illuminated by a SCHOTT light source[100] at the maximum power setting. The change in signal amplitude as a function of exposure time is shown in Figure 3.33. The exposure time is the time period when the shutter is triggered open, which is synchronized with other clock sequences in the same sequencer. Below an exposure time of 1.5 ms the signal response starts to drop, while no signal is observed at all when it further reduces to 0.9 ms and lower. The minimum exposure time is therefore taken as 1.5 ms.

The same setup was also used to determine the delay in opening and closing of the

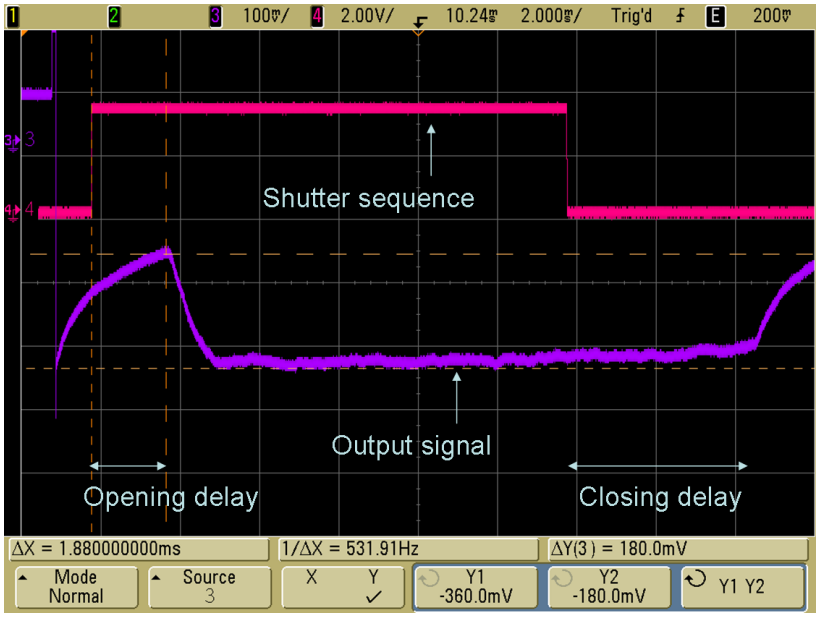

Figure 3.34: Oscilloscope trace for study of the shutter delay. The pink trace (trace 4) is the control sequence for the shutter and the purple trace (trace 3) is the output signal. The distance between the two vertical dashed lines shows the 1.88 ms delay in opening of the shutter.

shutter. The signal response on the output node is observed, so no clocking is applied except for regular reset to move the charge. Therefore it is easy to observe the change of the output with respect to the shutter on the oscilloscope. When the control sequence for the shutter is displayed in the oscilloscope at the same time as in Figure 3.34, the time difference between the shutter opening and the edge of the signal increase gives the delay. It is found that the delay varies with the exposure time when the exposure time is short. When the exposure time is set above 4 ms, the opening delay is 1.88 ms and the closing delay is 4.4 ms.

The sequence control of the shutter is integrated into the main LabVIEW programme. When we measure the signal for k number of transfers, the shutter is triggered open when charge is in the $(20-k)^{th}$ storage cell. The delay of the shutter is taken into account when setting the trigger. The polysilicon gates become less resistive at the working temperature of 6.5°C, so the readout speed is faster than the case described in Section 3.6.1. The master clock can be set to 9 MHz while maintaining an efficient charge transfer. If we use the same sequence as in the previous sections this results in a transfer time $T_i \sim 9$ ms for each CCD cell, about 5% of the whole period. A very low rate of X-ray hits is therefore foreseen. In order to increase the rate we modified the sequence so that when the charge is transferred

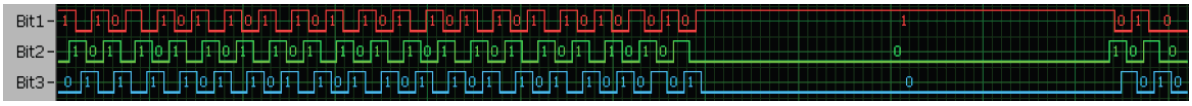

Figure 3.35: Sequence of the CCD clocks that pauses at the 19th CCD register.

to the target storage cell, the first gate from the three-phase CCD is held high for N times of T_i while the other two gates are held low (Figure 3.35). Due to this the charge transfer is paused to integrate the signal at the first gate. N is set to 18 in our measurement (equivalent to pausing the sequence for 112.5 ms) because a larger value will result in too much dark current that saturates the well capacity of the gates.

CTE Result with the Shutter

The main difficulty of this CTE measurement is the low rate of X-ray hits. The area under study is limited to one CCD gate which is very small. In addition the source is placed far from the sensor to allow installation of the shutter. As a result, only a few tens of ^{55}Fe hits are obtained for each measurement which typically lasts 10 hours. With the small number of entries it is difficult to fit a well-defined signal peak as in Figure 3.23. The peak position is therefore estimated as following. Assume the signal peak still obeys a Gaussian distribution, then 96% of the entries should fall into a $\pm 2\sigma$ window around the peak. The pedestal peak is well defined and its fitting can give the standard deviation σ. It is reasonable to assume that the σ values of the pedestal and the signal peak are roughly the same. Then the signal peak is roughly reconstructed by spanning $\pm 2\sigma$ around the highest occupied bin. The number of hits in the signal peak is counted. For a Gaussian distribution 16% percent probability lies above 1σ greater than the mean value, so the 1σ position is determined at the point above which 16% of the total number of hits occur. The mean value of the signal peak is hence determined by stepping back 1σ. Though not ideal, this method allows a quantitative analysis of the measurements.

With the estimation mentioned above the separation of the pedestal peak and signal peak is plotted as a function of number of transfers in Figure 3.36. The last point with transfer number 20.33 corresponds to the transfer from the photogate to the output node.

The photogate has a larger area than the CCD gates so the transfer efficiency is expected to be smaller than that in the storage cells, which is consistent with the plot. A straight line fit is given in the plot without the transfer from the photogate. For estimation of the CTE in the storage cells, this fit without the photogate measurement is used, which is given by:

$$y = (-124 \pm 25) \cdot x + (7789 \pm 279). \tag{3.5}$$

Relate the equation above to Equation 3.4, the CTI is calculated as:

$$\text{CTI} = -\frac{slope}{intercept} = -\frac{-124}{7789} = 1.59\% \tag{3.6}$$

hence the CTE is $1 - \text{CTI} = 98.41\%$.

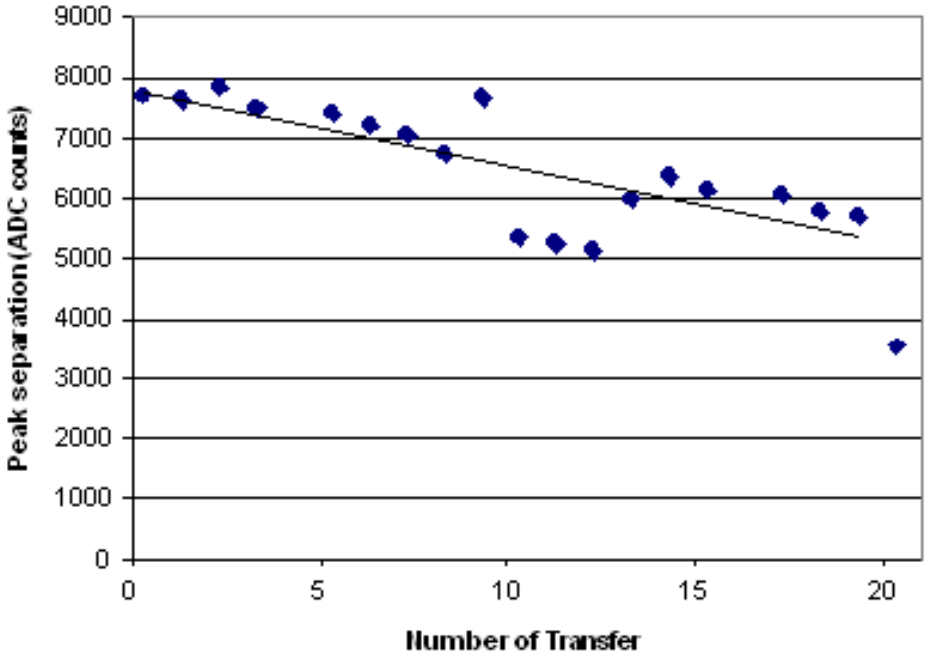

Figure 3.36: Separation of ^{55}Fe signal peak and pedestal peak versus number of transfers. This was obtained with a mechanical shutter placed between the X-ray source and the sensor. The straight line fit shows the fitting for transfer from storage cells only.

The uncertainty of the CTI is estimated as:

$$\delta_{\text{CTI}} = \text{CTI} \cdot \sqrt{(\frac{\delta_{slope}}{slope})^2 + (\frac{\delta_{intercept}}{intercept})^2} = 0.32\% \tag{3.7}$$

which gives a final CTE result of $98.41 \pm 0.32\%$. The main source of the large uncertainty comes from the determination of the signal peak position, which is in turn due to the low signal rate. Another possible source of uncertainty is the presence of K_β hits which is ignored in the analysis above. The CTE result itself demonstrates a quite efficient charge transfer capability of the ISIS2 sensor, and the result is consistent with that presented in [98].

3.7 Conclusion

The ISIS sensor is one of the sensor technologies proposed for the ILC vertex detector. It stores raw charge at the pixel level during ILC bunch trains and reads it out in the quiet time between bunch trains. This approach has the advantage of low peak power, and it avoids power cycling.

The ISIS2 sensor is the second generation of sensors based on the ISIS principle, with CCD registers implemented in a CMOS process. The tests performed in this chapter showed its successful local charge storage capability and good charge transfer efficiency (CTE). The well capacity were measured for various biases. Charge transfer through pixels with 20 memory cells was observed. Two independent measurements both gave a CTE better than 98%. Some unexpected features were observed and characterized, such as the slow charge transfer caused by resistive polysilicon gates. This is easy to correct in future sensor iteration, and with such correction the sensor readout could reach the nominal rates of the ILC and tests with full array will be possible.

The testing results described here showed that the ISIS principle is promising for the ILC vertex detector. A next sensor iteration, ISIS3, based on the ISIS2 results could in principle directly applicable to the ILC vertexing. The ISIS3 should be a large sensor with more compact sensor geometry. The pixel area should be reduced by a factor of two comparing to the ISIS2. A readout architecture should be implemented with data serialization.

Chapter 4

Chargino and Neutralino Mass Measurements

4.1 Introduction

The chargino or neutralino pair production or so-called SUSY Point 5 is one of the benchmarking processes proposed for the ILC [26]. The SUSY Point 5 has the SUSY parameters as listed in Table 4.1 based on the NUHM model as introduced in Section 1.2. the lightest chargino mass is smaller than slepton masses but at the same time is much larger than the lightest neutralino mass. The $\tilde{\chi}_1^0$ is the Lightest Supersymmetry Particle (LSP), and for this choice of SUSY parameters charginos dominantly decay into the LSP and on-shell W bosons. In this scenario the $\tilde{\chi}_2^0$ mass is almost degenerate with the $\tilde{\chi}_1^\pm$ mass, so similarly it decays into an LSP and a Z boson. The decay chain of $\tilde{\chi}_1^\pm$ and $\tilde{\chi}_2^0$ is shown in Figure 4.1.

$$\begin{aligned} e^+e^- &\rightarrow \tilde{\chi}_1^+\tilde{\chi}_1^- \rightarrow \tilde{\chi}_1^0\tilde{\chi}_1^0 W^+W^- \\ e^+e^- &\rightarrow \tilde{\chi}_2^0\tilde{\chi}_2^0 \rightarrow \tilde{\chi}_1^0\tilde{\chi}_1^0 Z^0Z^0 \end{aligned}$$

If we consider all-hadronic decays of the gauge bosons in the final state, the above processes will both be defined by a signature of four jets with a large missing energy. Once the

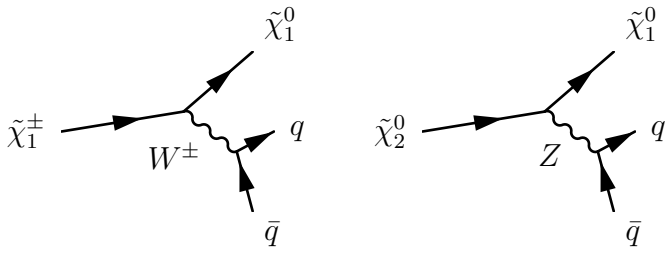

Figure 4.1: The decay chain of the $\tilde{\chi}_1^\pm$ (left) and $\tilde{\chi}_2^0$ (right) studied in this thesis.

parameter	value
m_0	206 GeV
$m_{1/2}$	293 GeV
tan β	10
A	0
μ	375 GeV
$M_{\tilde{\chi}_1^0}$	115.7 GeV
$M_{\tilde{\chi}_1^\pm}$	216.5 GeV
$M_{\tilde{\chi}_2^0}$	216.7 GeV

Table 4.1: SUSY point 5 parameters.

W or Z bosons are successfully reconstructed, their energy distribution will provide information on the chargino and neutralino masses. By comparing the energy distribution obtained from the data to Monte-Carlo templates, it will be determined whether the chargino and neutralino masses agree with those listed in Table 4.1.

Characteristic of many analyses with SUSY particles, large Standard Model backgrounds need to be suppressed for this analysis. Another challenge is to separate the $\tilde{\chi}_1^+\tilde{\chi}_1^-$ and $\tilde{\chi}_2^0\tilde{\chi}_2^0$ signals. Since this measurement requires separation of pairs of W and Z bosons reconstructed from two jets, excellent jet energy resolution, hence a good performance of the Particle Flow Algorithm, is essential.

The simulation and reconstruction of the data samples in the context of the ILC software framework is introduced in Section 4.2. The analysis strategy is defined as follows. Common preselections for the $\tilde{\chi}_1^+\tilde{\chi}_1^-$ and $\tilde{\chi}_2^0\tilde{\chi}_2^0$ events are defined to suppress the Standard Model background, as described in Section 4.3. The cross-sections of both signal processes could be determined after they are separated using the di-jet mass correlation as described in Section 4.4. The energy distributions of the gauge bosons as decay products of charginos and neu-

tralinos give information on the SUSY particle masses. The masses and their uncertainties are determined by the template fitting method presented in Section 4.5.

4.2 Analysis Software

Before starting construction of modern accelerators and detectors a virtual environment should be in place to model their functionality. This will allow studies of the detector performance and optimization of the design while demonstrating its physics potential in necessary detail. It is also useful for development of various reconstruction algorithms. Monte-Carlo data of various processes are generated, their interaction with detectors is modeled and event reconstruction is performed. This section will give a brief introduction to the software framework employed for the SiD concept studies, in the context of the Chargino or Neutralino Mass measurement.

4.2.1 Event Simulation

The simulations start from generation of various SM processes and processes corresponding to other theoretical models. The Monte Carlo program Whizard 1.4 [101] is used for generation of all samples in the analysis. The samples include:

- Standard Model sample: a SM sample with $\sqrt{s}$ of 500 GeV and integrated luminosity of 500 fb^{-1} is generated for analysis of SiD benchmarking processes [48] including the chargino and neutralino analysis presented here. All SM final states with 0, 2, 4 and 6 quarks are included. The number of events generated is $\sim 5 \times 10^6$, less than the 500 fb^{-1} integrated luminosity because some processes with large cross-sections have restricted number of events to save on the total computing resources.

- SUSY sample: This consists of the chargino and neutralino signals and SUSY backgrounds such as $e^+e^- \rightarrow \tilde{\chi}_1^0\tilde{\chi}_2^0$ and slepton pair production, with SUSY parameters listed in Table 4.1. The number of events generated is approximately 1.3×10^6, and

they are weighted to an integrated luminosity of 500 fb^{-1}. The cross-section of chargino production accounting for all hadronic final states is 57.1 fb and the corresponding neutralino one is 11.0 fb. Note that the cross-section of neutralino pair production is considerably smaller than the chargino one, therefore, the separation of the two, especially the neutralino selection in the presence of a large chargino background, is challenging.

- Mass-varied SUSY samples: In order to estimate the uncertainty of Chargino and Neutralino masses, several additional samples with the same statistics were generated, each with one SUSY particle mass shifted by a certain amount ΔM, see Table 4.2.

The samples have the same polarization, namely 80% left handed electrons and 30% right handed positions. In practice, all events are generated using fully (100%) polarized electrons and positrons. Unpolarized electrons are obtained by mixing equal amount of 100% left-handed and 100% right-handed electrons, so are the positrons. Samples with the desired polarization are then produced by properly combining the events. It should be noted that the W mass was mistakenly set to 79.8 GeV and this was taken into account in the analysis.

Template	$M_{\tilde{\chi}_1^0}$ (GeV)	$M_{\tilde{\chi}_1^\pm}$ (GeV)	$M_{\tilde{\chi}_2^0}$ (GeV)
standard	115.7	216.5	216.7
$\tilde{\chi}_1^0 + \Delta M$	115.7 + ΔM	216.5	216.7
$\tilde{\chi}_1^\pm + \Delta M$	115.7	216.5 + ΔM	216.7
$\tilde{\chi}_2^0 + \Delta M$	115.7	216.5	216.7 + ΔM

Table 4.2: SUSY sample parameters. $\Delta M = -0.5; 0.5; 2\,\text{GeV}$ or $6\,\text{GeV}$ (only for $\tilde{\chi}_2^0$)

The output of the Whizard generator is quarks and gluons, therefore they need to be run through parton showering, fragmentation and decay to provide observable particles for the final state. PYTHIA 6.4 [102] is used to perform these steps.

Interaction of particles with the detector at the ILC needs to be subsequently simulated. This includes description of the detector geometry and modeling of interactions of particles with specific detector materials in the presence of a magnetic field. Design of the ILC and

SiD is still in progress, therefore such detector simulations are not only necessary for physics analysis, but also essential for the optimization of the detector design. As is common in particle physics today, the full detector simulation is provided by the GEANT4 toolkit [103] [104]. An additional layer of code, Simulator for the Linear Collider (SLIC) [105], is used by the SiD detector concept as an interface to the GEANT4 framework. Different detector geometries are defined in SLIC in the XML format to facilitate optimization of the detector performance. Out of existing variations, the baseline design geometry sid02 [106] is employed for the analysis in this thesis. The data output uses the standard LCIO format [107].

Simulation of individual raw signal deposition in the detector is not included in the GEANT4 simulation. Energy deposits in the detector sensitive material are transformed into a detector response at the digitization step of the reconstruction. This is convenient for study of various readout configuration, avoiding the need for re-running of the full simulation each time.

4.2.2 Event Reconstruction

The general purpose at the reconstruction stage is to identify each particle object from the information collected in the detector. It is aimed to model the detector with enough detail so that all the reconstruction algorithms used here could in principle be applicable to real data. In the following sections the tracking algorithm, the Particle Flow Algorithm (PFA) and the jet clustering algorithm will be discussed.

The software framework that implements the reconstruction differs for various detector concepts. The SiD concept developed the org.lcsim 1.5 framework [108] for this purpose and the ILD concept uses the MarlinReco package [109]. For the analysis described here, the samples have been processed through org.lcsim for tracking and particle identification, where pattern recognition of hadronic final states using a PFA algorithm is devised for the SiD [47]. The jet clustering and further physics analysis are performed within the MarlinReco framework.

Tracking Algorithm

The purpose of a track finding algorithm is to efficiently reconstruct tracks left by charged particles using hits in the tracking system, namely the vertex detector and the tracker. A good tracking system should reconstruct a set of tracks with high efficiency and minimal number of fake tracks. A standard pattern recognition algorithm and a calorimeter assisted tracking algorithm developed for the SiD have been successively employed at the reconstruction stage.

The tracks are first reconstructed with the standard pattern recognition algorithm, which provides a uniform pattern recognition throughout the whole tracking system across different parts of the detector. It is exhaustive in the sense of considering all possible combinations of hits which could potentially form a track. Its decision making is based on a global χ^2 value. This algorithm consists of the following steps:

1. The digitized hits found in the tracking system are converted to a unified format, so that the further track finding algorithm should not differ for hits from pixels or strips, barrel or endcap. Three types of hits are accepted: pixel hits, axial hits from a single strip or stereo hits from a pair of strips.

2. All three-hit combination from three "seed" layers of the silicon tracker are taken to form a track candidate. The three candidate hits are fitted with a helix and those that fail a particular χ^2 requirment are eliminated. The remaining candidates form "seeds".

3. A seed is confirmed by adding another hit from a confirmation layer. A helix is fitted for the seed hits and the confirmation hit, and the track candidate is "confirmed" if the resulting χ^2 passes a certain cut. The number of confirmation layers is a user defined parameter but studies found that one is enough for a good performance[47].

4. The confirmed seed track is extended by adding hits from an extension layer, similar to adding confirmation hits to the seed. Helix fits are performed for each added hit and the hits passing χ^2 cut are added to the track. If no hit can be added to the confirmed seed in one layer, searches will continue for the next extension layer.

5. Finally the track seeds with enough hits are selected as a collection of reconstructed tracks. An arbitration scheme is used to choose track seeds which share same hits.

This algorithm has a built-in flexibility because it allows the user to define a set of strategies including the role (seed, confirm or extend) of layers used, kinematic constraints, required number of hits and the χ^2 cut values. The strategy used in this thesis as well as in the other SiD benchmarking studies requires one confirmation layer, a minimum of 7 hits per track, transverse momentum $p_T > 200$ MeV and the closest distance to the interaction point < 10 mm in both the xy and z directions. All helix fits are performed with a fast helix fitter. The tracking uncertainties caused by multiple scattering are estimated and included in the helix fit.

The calorimeter assisted tracking algorithm is performed after the standard pattern recognition and helps to find tracks primarily from K_S^0 and Λ decay products. Clusters in the electromagnetic calorimeters (ECAL) are considered as seeds for tracks if they are consistent with a minimum ionization particle (MIP) energy deposition and if they have hits in the inner ECAL layers. MIP stubs unattached to any reconstructed tracks are propagated back to the tracker and are combined with hits not assigned to any reconstructed tracks. The quality of these new candidates is checked and ambiguities are resolved before the new reconstructed tracks are added to the complete track collection.

Particle Flow Algorithm

The goal of a Particle Flow Algorithm (PFA) is to reconstruct individual particles. Theoretically a jet energy resolution of $\sigma_E/E = 20\%/\sqrt{E(GeV)}$ can be achieved if there is no confusion between calorimeter responses caused by charged or neutral particles. A good PFA algorithm, therefore, should have excellent segmentation to minimize the confusion. For optimal use of each subsystem, the PFA algorithm designed for the SiD concept [47][110] takes the reconstructed tracks (as described in the previous section) and the energy depositions in calorimeters and muon detectors as input information.

The first step of the PFA algorithm is to identify photons, electrons and muons with track and cluster association. Electromagnetic showers are reconstructed in the ECAL. The ECAL clusters not associated with any tracks are identified as photons. The ECAL clusters whose locations are consistent with tracks from a charged particle are reconstructed as electrons, if their energy matches the tracks' momenta. Muon identification utilizes information from the muon detector in addition to tracking systems and calorimeters. A standalone muon "stub" is identified in the muon detector, with a group of isolated hits close to the projection line from the interaction point. The incoming direction of the muon stub can be determined. The tracks reconstructed in the tracking system are extrapolated through the calorimeters with a helical trajectory. If the outgoing direction of an extrapolated track at the end of the hadronic calorimeter is consistent with the direction of the muon stub, a muon is identified, with its direction obtained from the stub in the muon detector. The minimum momentum required to reach the endcap and barrel muon detectors is 2 GeV and 5 GeV respectively, below which the efficiency and purity of muon reconstruction are poor.

The next step is the hadron identification, aiming at minimum confusion between charged and neutral particles. Every extrapolated track has a directly connected cluster in the calorimeters which is defined as a seed. The clusters are assigned to a charged hadron's track by adding clusters to the seed according to their geometrical proximity until the track's momentum equals to the total deposited energy of the clusters within uncertainties. This algorithm for reconstruction of charged hadron showers does not consider the internal structure of the shower, or the secondary particle hits or back-scattering of low energy particles. These effects are taken into account by assigning clusters in a cone to the tracks whose deposited energy in the calorimeters is not equal to their momentum obtained from the tracking system. Clusters still left unassociated with any track after these iterations are identified as neutral showers.

The final step of the PFA algorithm is to reconstruct four-momenta for all visible particles. For charged particles they are obtained from the tracking system and for neutral particles the four-momenta are calculated from the energy measured in the calorimeters. The charged

process	Energy resolution	
	Barrel	Endcap
$e^+e^- \to Z(q\bar{q})Z(\nu\bar{\nu})$	4.7%	3.9%
$e^+e^- \to q\bar{q}, \sqrt{s} = 100$ GeV	3.7%	3.8%
$e^+e^- \to q\bar{q}, \sqrt{s} = 200$ GeV	3.0%	3.2%
$e^+e^- \to q\bar{q}, \sqrt{s} = 360$ GeV	2.7%	2.7%
$e^+e^- \to q\bar{q}, \sqrt{s} = 500$ GeV	3.5%	3.3%

Table 4.3: PFA performance for sid02. For the $e^+e^- \to q\bar{q}$ events, the rms90 of energy sum is quoted as a fraction of centre-of-mass energy; for the $e^+e^- \to ZZ$ process, the rms90 of the dijet mass is quoted as a fraction of Z mass. Here the resolutions are quoted in terms of rms90, defined as the root mean square of the central 90% of events.

and neutral hadrons are assumed to be pions and kaons in the calculation respectively.

The performance of the algorithm described above has been studied with simulation for the detector geometry sid02. The energy resolution for processes with various centre-of-mass energies is listed in Table 4.3 [111]. The resolutions in the table are quoted in terms of rms90, defined as the root mean square of the central 90% of events. Note that at $\sqrt{s}$ of 500 GeV the energy resolution deteriorates because the energy leakage at the back of the calorimeters becomes important when the jet energy approaches 250 GeV making the pattern recognition much more challenging.

Jet Finding

The quarks directly produced in e^+e^- collisions first fragment into quarks and gluons through radiation of gluons and then gluon splitting. All these partons undergo hadronization resulting in many colorless hadrons in the final state. Usually these final state particles are boosted, so the directions of particles radiated from the same initial parton are close to each other. Their trajectories are confined to a cone, forming a jet. Jet finding algorithms aim at reconstructing the jets from the data where all individual particles have been identified. In the MarlinReco package, a Satoru Jetfinder processor[112] is dedicated to jet finding. The processor employs the Durham algorithm [113][114] as described below.

For every pair of final state particles (k, l) the scaled transverse momentum is calculated:

$$y_{kl} = \frac{2(1 - \cos\theta_{kl}) \min(E_k^2, E_l^2)}{E_{\text{vis}}^2} \tag{4.1}$$

where E_k, E_l are the energy of particle k, l respectively, θ_{kl} is the relative angle, and E_{vis} is the total visible energy. The y_{kl} is calculated for all combination of (k,l). The particles (k, l) with the minimum scaled transverse momentum is denoted as (i, j), whose transverse momentum y_{ij} will be combined and replaced by a so-called "pseudoparticle". The four-momentum of the pseudoparticle is obtained by adding those of the pair together:

$$p = p_i + p_j. \tag{4.2}$$

Such procedure is repeated for the new set of particles and pseudoparticle, until the minimum y_{ij} reaches beyond a set value y_{cut}. Then all the resulting pseudoparticles are taken as jets. In this analysis though, a fixed number of jets rather than a y_{cut} is set so that the iteration introduced above stops when the total number of jets is equal to the preset value - four jets corresponding to the decay products of a WW or ZZ pair when all bosons decay hadronically. The minimum scaled transverse momentum y_{min} for each event is recorded together with other jet parameters.

4.3 Signal Selection

A set of preselection criteria described in Section 4.3.1 are applied to all events to reject the SM and SUSY backgrounds. Then jets are properly paired (Section 4.3.2) for reconstruction of W and Z bosons.

4.3.1 Preselection

The SM background is a major background common to the $e^-e^+ \to \tilde{\chi}_1^+\tilde{\chi}_1^- \to \tilde{\chi}_1^0\tilde{\chi}_1^0 W^+W^-$ and $e^-e^+ \to \tilde{\chi}_2^0\tilde{\chi}_2^0 \to \tilde{\chi}_1^0\tilde{\chi}_1^0 ZZ$ processes. SUSY backgrounds include $e^-e^+ \to \tilde{\chi}_1^0\tilde{\chi}_2^0$ and

slepton pair production. In this analysis only the $W(Z) \to q\bar{q}$ signals are considered, so the leptonic and semi-leptonic decays of the W and Z bosons are also treated as backgrounds. In order to reject these common backgrounds while obtaining a sufficient efficiency for the signals, a set of selections is applied, based on the kinematics and event topology. The selection criteria are explained below:

- Total visible energy: For the $\tilde{\chi}_1^0\tilde{\chi}_1^0 q q \bar{q}\bar{q}$ final state, the $\tilde{\chi}_1^0$ cannot be detected resulting in large $\not{E}$, so only events with large missing energy are selected (the missing energy is estimated as the nominal centre-of-mass energy minus total visible energy);

- Number of tracks: The multiplicity of 4-jet signal events is generally high, events with low number of tracks are eliminated;

- Thrust; $\cos\theta_{thrust}$: Thrust is an event shape variable [115] defined as:

$$T = \max_{|\vec{n}|=1} \frac{\sum_i |\vec{p_i} \cdot \vec{n}|}{\sum_i |\vec{p_i}|} \tag{4.3}$$

  where $\vec{p_i}$ is the momentum of the ith particle, $\vec{n}$ is a unit vector which maximizes T. The angle between the beam and the $\vec{n}$ is defined as the thrust angle θ_{thrust}. Thrust indicates how much the final state particles are boosted. The neutralinos in the signal carry away large momentum, so W or Z decay products are not highly boosted comparing to many Standard Model processes. A selection on $\cos\theta_{thrust}$ is based on the consideration that jets originated from signal events should be distributed more uniformly rather than boosted along the beam direction.

- Isolated leptons: As introduced in Section 4.2.2, the jet finding algorithm forces 4 jets to be reconstructed. In this process some energetic leptons could be clustered as a jet on their own. If there is any jet containing an electron or a muon only (defined as isolated leptons), the event is eliminated.

- E_{jet};

- Fraction of EM energy in each jet;

- Lepton energy (defined as the energy of electrons and muons) in each jet;

  The three selections listed above are set for ruling out jets falsely reconstructed from energetic charged leptons;

- $\theta(i,j)$: opening angle between jet i and j (ordered by energy) is a criteria used to eliminate events in which one jet is falsely split into two;

- Acoplanarity[1]: Assume the projections of the two W or Z boson momenta $\vec{p_1}$ and $\vec{p_2}$ on the xy plane correspond to polar angles θ_1 and θ_2 respectively, then the acoplanarity A is defined as

$$A = |\theta_1 - \theta_2 + \pi|. \tag{4.4}$$

  The WW or ZZ pair from $\tilde{\chi}_1^+\tilde{\chi}_1^-$ or $\tilde{\chi}_2^0\tilde{\chi}_2^0$ decay are acoplanar, in contrast to the WW pairs produced through SM processes, whose acoplanarity is typically close to zero.

Table 4.4 shows exact values of the above selections used in the analysis. Distributions of the variables mentioned above are shown in Figure 4.2 and Figure 4.3. The figures are produced consecutively in the same order as the selections applied. The numbers of signal and background events after each of the selections are summarized in Table 4.5. After all the selections, the efficiency for the chargino and neutralino signals are 60.1% and 59.3% respectively, while only a fraction of 4.05×10^{-6} of the SM background and 1.74% of SUSY backgrounds (other than any of the signals) pass the selections. The effectiveness of the cuts is also illustrated by the distribution of the y_{min} value. As mentioned in the Durham jet finding algorithm in Section 4.2.2, the y_{ij} indicates the separation between two particles or pseudoparticles. The y_{min} is the minimum of the y_{ij} after all particles in the event are clustered into four jets. For the background events with less than 4 jets such as the SM di-jet processes, the y_{min} turns out to be very small to force 4 jets, as shown in Figure 4.4(a). After all selections are applied, especially the θ_{ij} selections, those backgrounds are practically eliminated (Figure 4.4(b)).

[1]The acoplanarity selection is actually applied after the separation of chargino and neutralino signals and kinematic fitting.

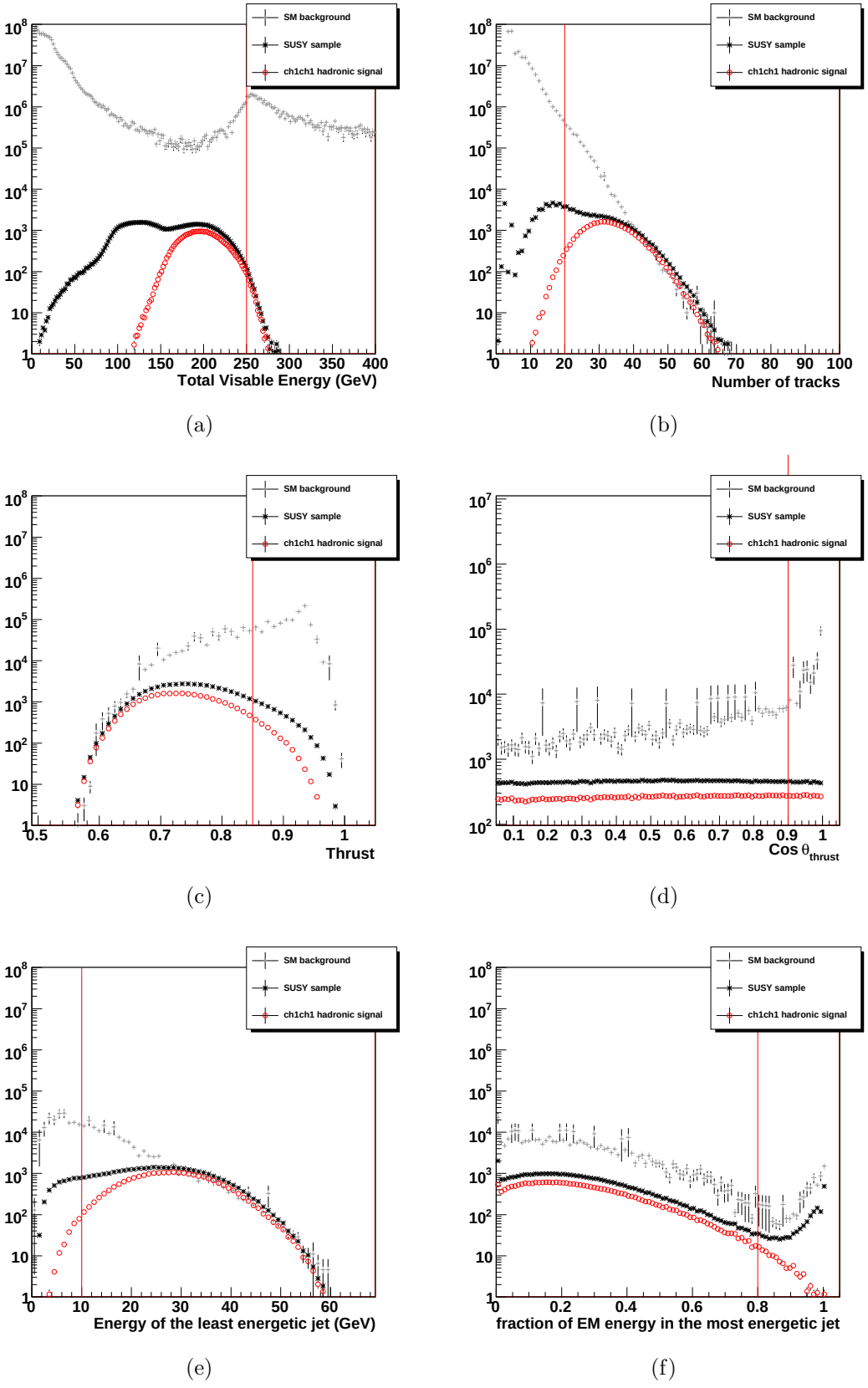

Figure 4.2: Distribution of variables used in preseclections, for $\tilde{\chi}_1^+\tilde{\chi}_1^-$ signal (circle), Standard Model background (star) and SUSY background (cross). (a) Total visible energy; (b) number of tracks; (c) thrust; (d) thrust angle θ_{thrust}; (e) energy of the least energetic jet; (f) Fraction of electromagnetic energy in the most energetic jet. The red lines show the cut values. The histograms are shown after each successive cut.

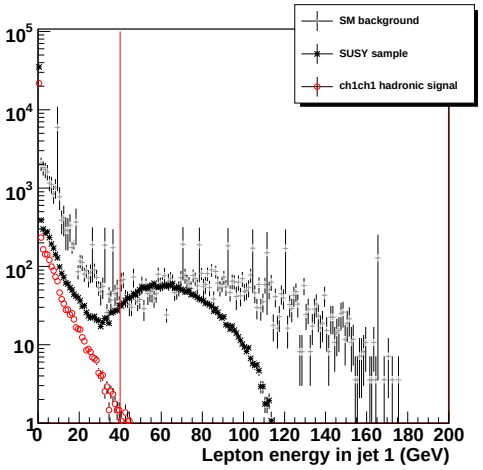

(a)

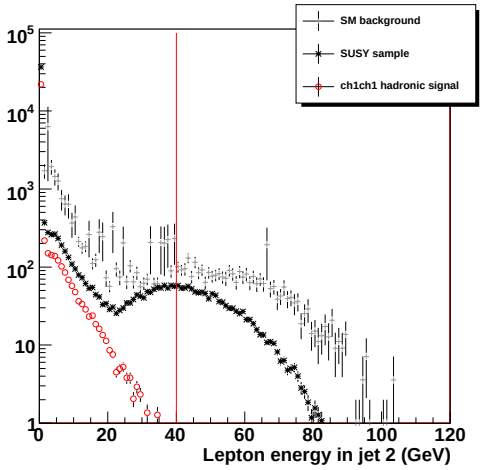

(b)

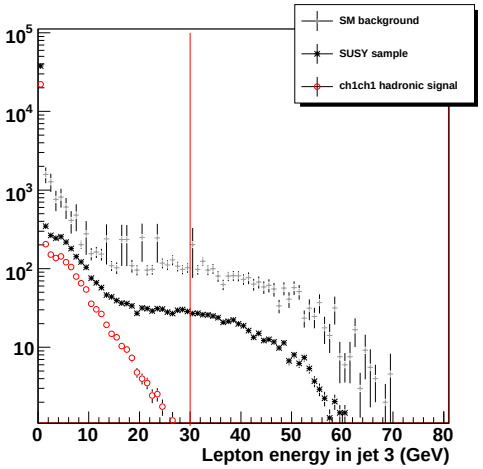

(c)

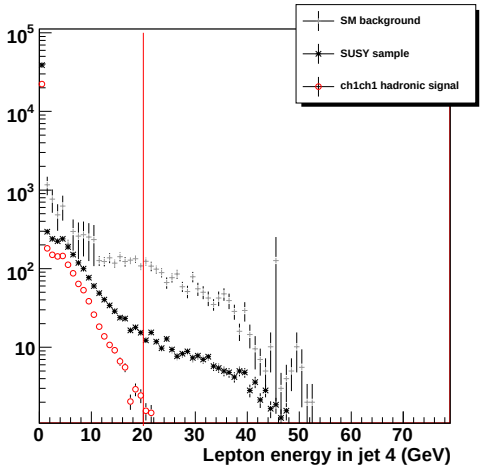

(d)

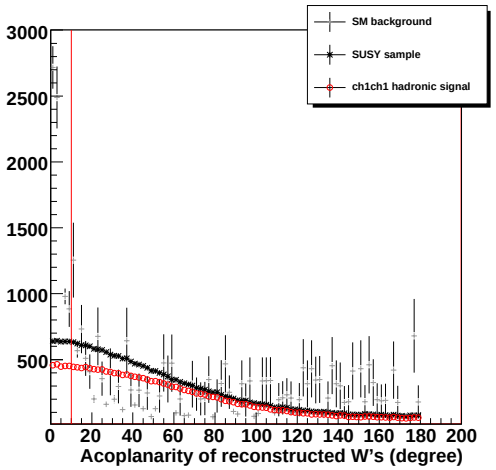

(e)

Figure 4.3: Distribution of variables used in preseclections, for $\tilde{\chi}_1^+\tilde{\chi}_1^-$ signal (circle), Standard Model background (star) and SUSY background (cross). (a)-(d) lepton energy in four jets (ordered by energy); (e) acoplanarity of two reconstructed W's (after kinematic fitting). The red lines show the cut values. The histograms are shown after each successive cut.

	selection	value
(1)	Number of Jets	$= 4$
(2)	Total visible energy	< 250 GeV
(3)	Number of tracks	> 20
(4)	Thrust	< 0.85
(5)	$\cos\theta_{thrust}$	< 0.9
(6)	Number of isolated leptons	$= 0$
(7)	Fraction of EM energy in each jet	$< 80\%$
(8)	lepton energy in jet 1	< 40 GeV
	lepton energy in jet 2	< 40 GeV
	lepton energy in jet 3	< 30 GeV
	lepton energy in jet 4	< 20 GeV
(9)	E_{jet}	> 10 GeV
(10)	$\theta(1, 2)$	$> 60°$
	$\theta(1, 3)$, $\theta(1, 4)$, $\theta(1, 3)$	$> 40°$
	$\theta(2, 4)$, $\theta(3, 4)$	$> 20°$
(11)	Acoplanarity of two reconstructed gauge bosons	$> 10°$

Table 4.4: Analysis pre-selections. $\theta(i, j)$ defines the opening angle between the ith and jth jet. Jets were ordered in energy, e.g. jet 1 is the most energetic jet.

4.3.2 Jet Pairing

To reconstruct two gauge bosons from four jets we have to determine the jet pairing corresponding to correct combinations. The invariant mass from all possible combinations of jet pairs is shown in Figure 4.5 for the hadronic $\tilde{\chi}_1^+\tilde{\chi}_1^-$ signal and in Figure 4.6 for the $\tilde{\chi}_2^0\tilde{\chi}_2^0$ signal. The correct combination is chosen by minimizing the quantity d defined as:

$$d = (m(j_1, j_2) - m_{W/Z})^2 + (m(j_3, j_4) - m_{W/Z})^2, \tag{4.5}$$

where $m(j_1, j_2)$ is the invariant mass of the jets j_1 and j_2. All possible jet permutations are considered. The W mass m_W is used when selecting $\tilde{\chi}_1^+\tilde{\chi}_1^-$ events, and correspondingly the Z mass m_Z is used for the $\tilde{\chi}_2^0\tilde{\chi}_2^0$ events[1]. The invariant dijet mass for $\tilde{\chi}_1^+\tilde{\chi}_1^-$ after the jet pairing is shown in Figure 4.5, correctly peaking at the W mass. Similarly, Figure 4.6 shows that for $\tilde{\chi}_2^0\tilde{\chi}_2^0$ where the Z mass peak is clearly visible.

Selection†	$\tilde{\chi}_1^+\tilde{\chi}_1^-$ signal	$\tilde{\chi}_2^0\tilde{\chi}_2^0$ signal	SM background	SUSY background
Before selections	28531	5482	6.24×10^9	74991
(1)	28531	5482	1.09×10^9	61160
(2)	28214	5145	9.79×10^8	61088
(3)	27530	5353	1.73×10^6	17904
(4)	26061	4933	616743	14287
(5)	23324	4484	336854	13020
(6)	23323	4484	330762	11465
(7)	22603	4377	306044	9089
(8)	22585	4359	303419	7805
(9)	22379	4334	135367	4553
(10)	19428	4019	39160	1461
(11)	17157	3250	25274	1307

Table 4.5: Number of signal and background events after each step of selections. † The selection index is listed in Table 4.4.

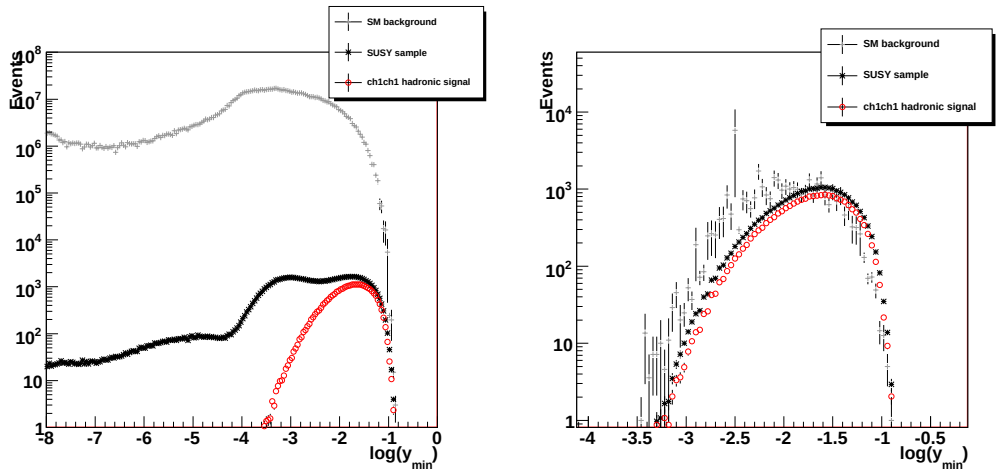

(a) (b)

Figure 4.4: The value of $\log(y_{min})$(a) without any preselection and (b) after angular selection (as well as other preselections). The grey crossed markers are Standard Model background, the black star marker show the total SUSY sample and the red circled markers are the pure hadronic $\tilde{\chi}_1^+\tilde{\chi}_1^-$ signal.

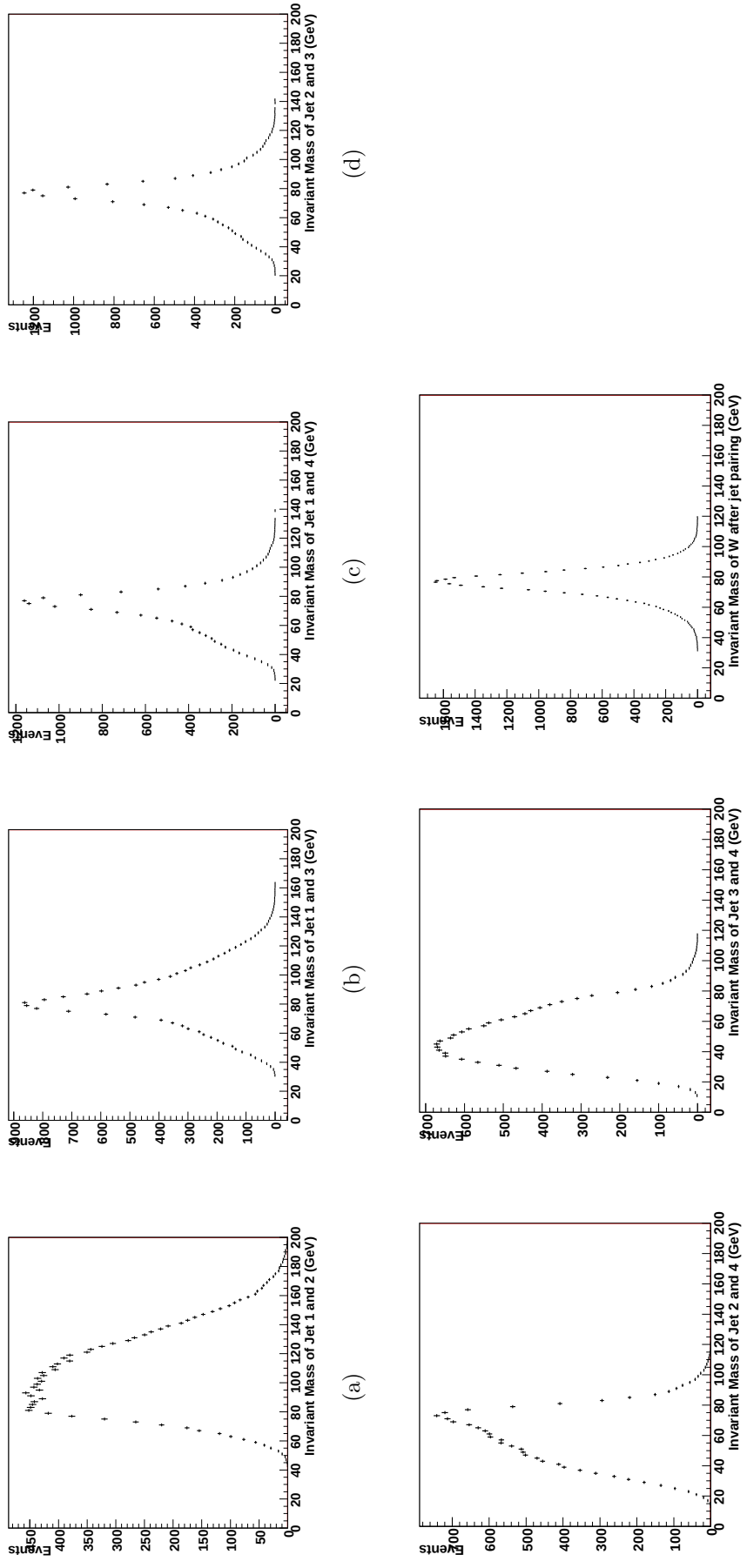

Figure 4.5: (a) - (f) Distributions of the invariant mass from all possible jet combinations for the pure hadronic $\tilde{\chi}_1^+\tilde{\chi}_1^-$ signal. Jets are ordered by energy. (g) shows the invariant dijet mass distribution after choosing the jet combination that minimizes the d value.

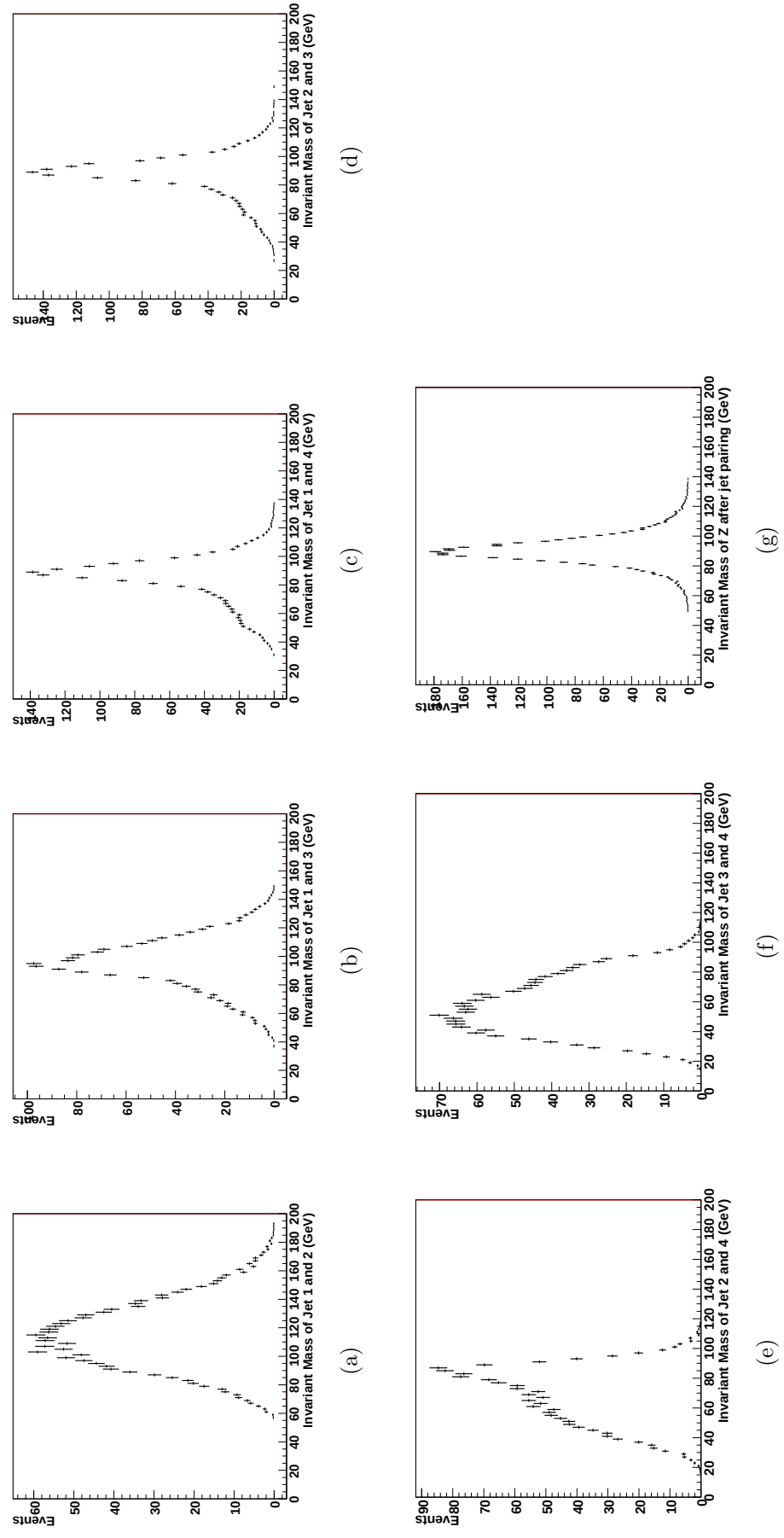

Figure 4.6: (a) - (f) Distributions of the invariant mass from all possible jet combinations for the pure hadronic $\tilde{\chi}_2^0\tilde{\chi}_2^0$ signal. Jets are ordered by energy. (g) shows the invariant dijet mass distribution after choosing the jet combination that minimizes the d value.

4.4 Chargino and Neutralino Separation

For the common preselections described above, the major concern is to suppress the SM background. However for each individual signal, $\tilde{\chi}_1^+\tilde{\chi}_1^-$ or $\tilde{\chi}_2^0\tilde{\chi}_2^0$, the other is part of the background. The separation of both signals is therefore essential. The separation is based on the correlation of two reconstructed boson masses as explained below.

4.4.1 Separation of Chargino and Neutralino Signals

The correlation of two reconstructed boson masses is shown in Figure 4.7. The reconstructed boson masses populate different regions in the histogram for chargino and neutralino signal events. A study has been performed on how to separate the two signals based on the signal purity and efficiency after the separation. Two kinds of separation selections have been considered: χ^2 cut and "box" cut. Both selection criteria are based on the fact that the $\tilde{\chi}_1^+\tilde{\chi}_1^-$ and $\tilde{\chi}_2^0\tilde{\chi}_2^0$ signals should populate areas around points (m_W, m_W) and (m_Z, m_Z) respectively.

The χ^2 cut means that all events are classified as $\tilde{\chi}_1^+\tilde{\chi}_1^-$ events if they satisfy:

$$\chi^2 \leq \frac{(m_1 - m_W)^2 + (m_2 - m_W)^2}{m_W^2} \tag{4.6}$$

where m_1 and m_2 are the two reconstructed boson masses and χ^2 is a chosen value. In the boson mass correlation plot, this is equivalent to a circle with radius of $\chi \cdot m_W$ centered at (m_W, m_W). Similarly, m_Z is used instead of m_W for the $\tilde{\chi}_2^0\tilde{\chi}_2^0$ events. The purity and efficiency for $\tilde{\chi}_1^+\tilde{\chi}_1^-$ and $\tilde{\chi}_2^0\tilde{\chi}_2^0$ signals with various χ^2 cut values are shown in Figure 4.8. Note that the purity of the χ^2 cut is defined as the ratio of the chargino (or neutralino) signal events over the total number of SUSY events after the cut. The SM background is not considered at this step. The efficiency is defined as the ratio of chargino or neutralino signal events after selection over the total event number before any preselection.

The "box" cut, on the other hand, applies a line cut in the mass correlation plot. The

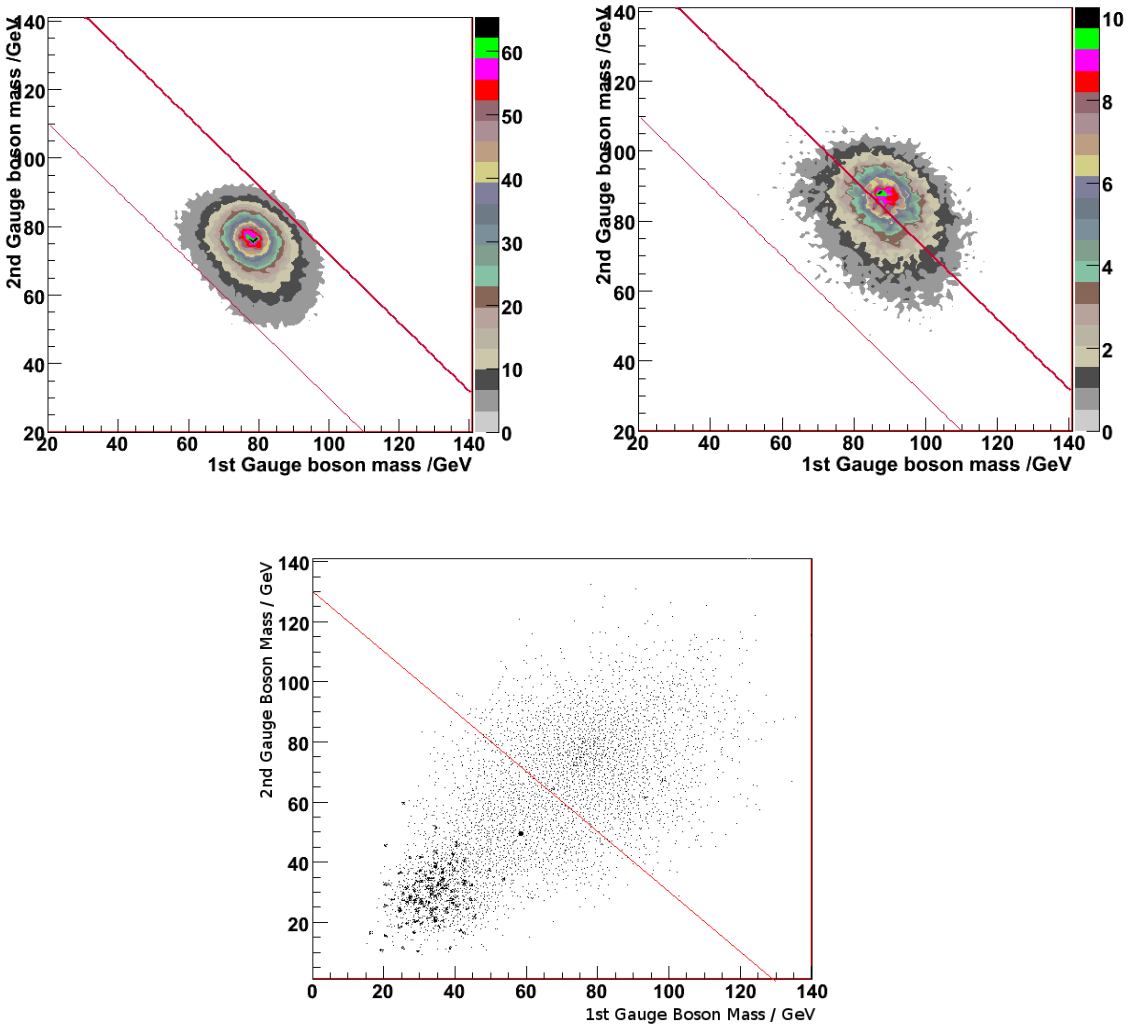

Figure 4.7: Reconstructed boson masses from the four jets, for the chargino selection. (a) pure chargino signal; (b) pure neutralino signal; (c) SM background. The thicker solid line is the separation cut for the neutralino and chargino signals. The thinner line is a separation cut between the chargino signal and the SM background.

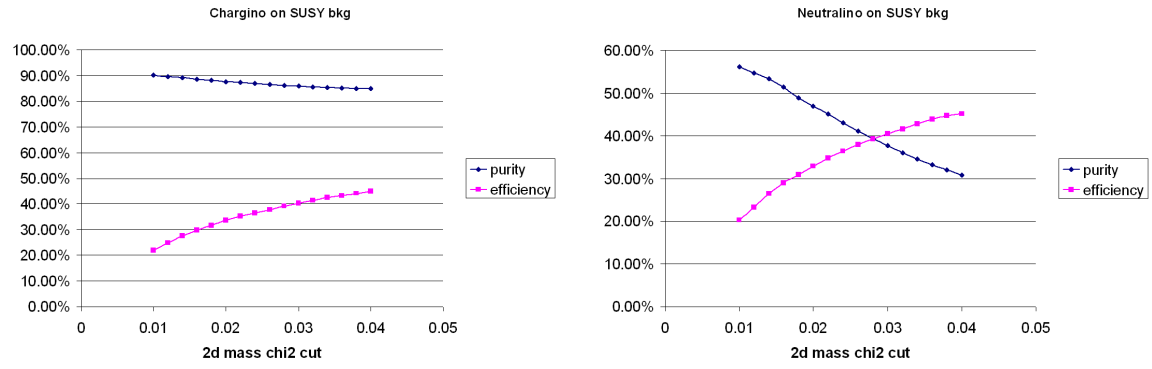

(a) (b)

Figure 4.8: Purity and efficiency of (a)$\tilde{\chi}_1^+\tilde{\chi}_1^-$ signal and (b)$\tilde{\chi}_2^0\tilde{\chi}_2^0$ signal in the presence of SUSY background as functions of χ^2 cut.

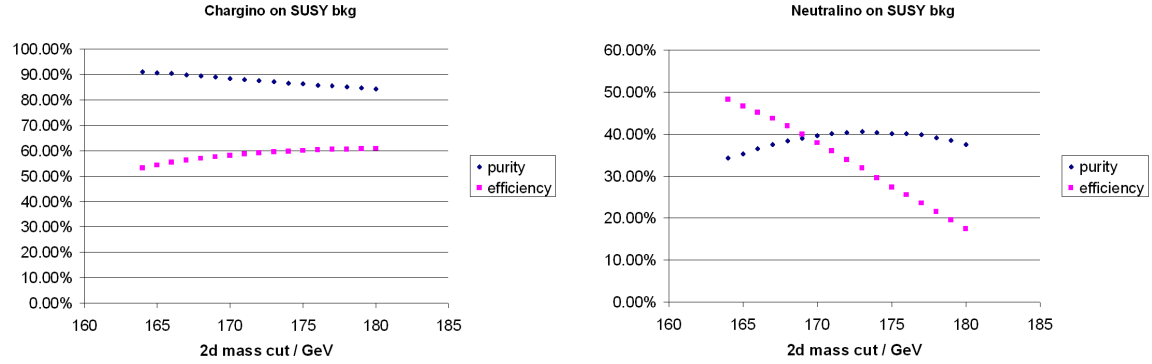

(a) (b)

Figure 4.9: Purity and efficiency of (a)$\tilde{\chi}_1^+\tilde{\chi}_1^-$ signal and (b)$\tilde{\chi}_2^0\tilde{\chi}_2^0$ signal in the presence of SUSY background as functions of box cut.

events are classified as $\tilde{\chi}_2^0\tilde{\chi}_2^0$ events if

$$m_1 + m_2 > M_{cut}(\text{GeV}) \tag{4.7}$$

otherwise they are classified as $\tilde{\chi}_1^+\tilde{\chi}_1^-$. The purity and efficiency for both signals for different M_{cut} values are shown in Figure 4.9.

The relatively smaller production cross-section of $\tilde{\chi}_2^0\tilde{\chi}_2^0$ means that it is more difficult to identify it from the SUSY background. From the purity and efficiency studies it is found that a small χ^2 cut value can help to obtain a $\tilde{\chi}_2^0\tilde{\chi}_2^0$ sample with high purity, but at the cost of a low efficiency. The χ^2 cut also leads to a lower efficiency for the chargino signal. As a result the box cut criteria is used, with the cut value set as a trade-off between purity

and efficiency for the neutralino samples. The cut is indicated by a thick line in Figure 4.7. Events in the lower left part ($m_1 + m_2 \leq 172\,\mathrm{GeV}$) are classified as $\tilde{\chi}_1^+\tilde{\chi}_1^-$ events and in the upper right part ($m_{W1} + m_{W2} > 172\,\mathrm{GeV}$) as $\tilde{\chi}_2^0\tilde{\chi}_2^0$ events.

For chargino events selection we also add a selection to remove events in the most lower left corner of the 2D mass histogram ($m_{W1} + m_{W2} > 130\,\mathrm{GeV}$ as shown in Figure 4.7(c), which are due to the remaining leptonic or semi-leptonic decays of the bosons.

4.4.2 Kinematic Fitting

Determination of chargino and neutralino masses is based on the energy distribution of the W or Z bosons reconstructed from two jets. The energy distribution is therefore essential in this analysis and we attempt to improve it by a kinematic fitting algorithm. Four-vectors of the objects of interest (jets in this case) are parameterized. These measured parameters can be varied within their uncertainties so that a global χ^2 is minimized under kinematic constraints given by a specific physics process, a procedure called kinematic fitting. A brief mathematical description of kinematic fitting is given below.

Assume that there are N measured parameters $\vec{y}(y_1, ..., y_N)$ with corresponding fitted parameters $\vec{\eta}(\eta_1, ..., \eta_N)$ and J unmeasured parameters $\vec{\xi}(\xi_1, ..., \xi_J)$, then a general χ^2 can be written as:

$$\chi^2 = (\vec{y} - \vec{\eta})^T \cdot V^{-1} \cdot (\vec{y} - \vec{\eta}). \tag{4.8}$$

where V^{-1} is the inverse of the covariance matrix of the measurements. A total of K kinematic constrains can be expressed as

$$\vec{f}(\vec{\eta}, \vec{\xi}) = 0, \tag{4.9}$$

where $\vec{f} = f_1, ..., f_K$. Using Lagrange multipliers, a new χ_T^2 is defined as:

$$\chi_T^2 = (\vec{y} - \vec{\eta})^T \cdot V^{-1} \cdot (\vec{y} - \vec{\eta}) + 2\vec{\lambda} \cdot \vec{f}(\vec{\eta}, \vec{\xi}), \tag{4.10}$$

where $\vec{\lambda} = \lambda_1, ..., \lambda_K$ are Lagrange multipliers. The χ^2_T consists of a general χ^2 and a constraint term. The best set of fitted parameters $\vec{\eta}$ should minimize the χ^2_T. So taking derivatives in Equation 4.10 and setting the derivatives to zero we can get a set of equations:

$$V^{-1} \cdot (\vec{\eta} - \vec{y}) + \vec{F}_\eta^T \cdot \vec{\lambda} = \vec{0}, \tag{4.11}$$

$$\vec{F}_\xi^T \cdot \vec{\lambda} = \vec{0}, \tag{4.12}$$

$$\vec{f}(\vec{\eta}, \vec{\xi}) = 0 \tag{4.13}$$

where matrices $\vec{F}_\eta$ and $\vec{F}_\xi$ are defined as:

$$(F_\eta)_{kn} = \frac{\partial f_k}{\partial \eta_n} \tag{4.14}$$

$$(F_\xi)_{kj} = \frac{\partial f_k}{\partial \xi_j}. \tag{4.15}$$

By solving the equations the $\vec{\eta}$ are obtained. Note that Equation 4.13 corresponds exactly to the kinematic constraints.

The equations are generally nonlinear, so they are solved numerically. Kinfit in Marlinreco software package [116] is used for the fitting in this analysis. The fitted parameters are the energy E, polar and azimuthal angle θ, ϕ of each jet. The uncertainty of the parameters are set as $50\%/\sqrt{E}$ for the jet energy and 100 mrad for θ and ϕ, according to a study for the SiD detector[117]. Only one kinematic constraint is applied, which is that the invariant mass from each pair of jets should be the same ($m_{boson1} = m_{boson2}$). The uncertainty on the W mass improved from 6.7 GeV to 4.4 GeV after the kinematic fitting, and the uncertainty on the Z mass improved from 6.8 GeV to 3.4 GeV. The uncertainties were estimated by fitting the distribution with a single Gaussian. In their energy distribution the upper and lower edges are more clearly defined. The distribution of the boson mass and energy are shown in Figure 4.10 for W and in Figure 4.11 for Z. The kinematic fitting is performed after the separation of $\tilde{\chi}_1^+\tilde{\chi}_1^-$ and $\tilde{\chi}_2^0\tilde{\chi}_2^0$ signals because otherwise the di-jet mass correlations as shown in Figure 4.7 will be reduced to one-dimensional because of the $m_1 = m_2$ constraint.

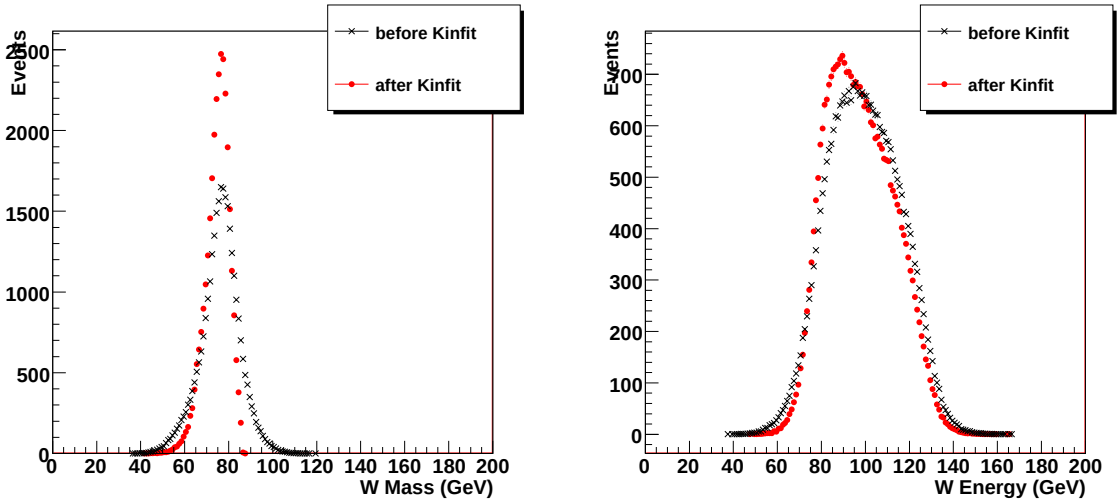

(a) (b)

Figure 4.10: Mass (a) and energy (b) distributions of the reconstructed W boson before (black crosses) and after (red dots) kinematic fitting.

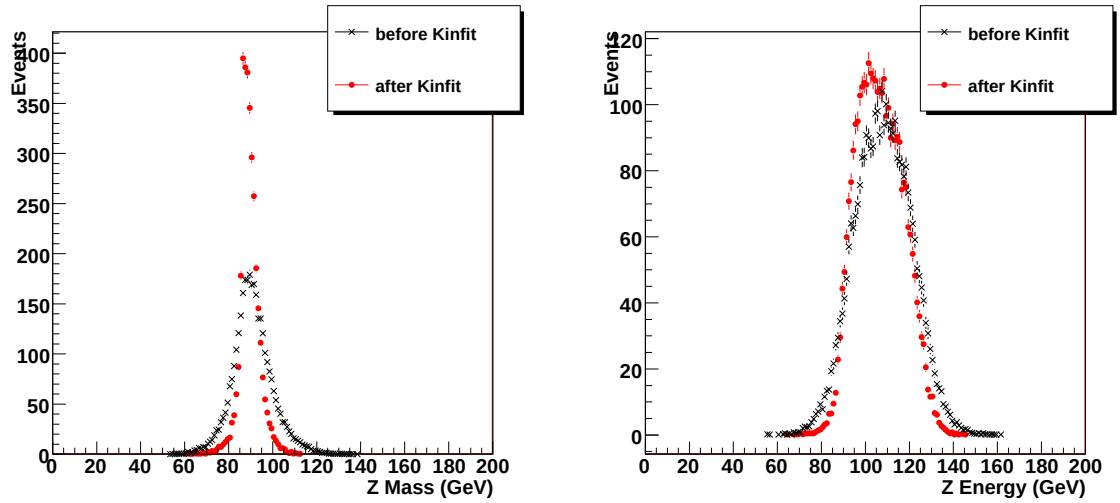

(a) (b)

Figure 4.11: Mass (a) and energy (b) distributions of the reconstructed Z boson before (black) and after (red) kinematic fitting.

4.4.3 Measurement of Chargino and Neutralino Pair Production Cross-sections

The reconstructed boson energy distribution are shown in Figure 4.12 after the preselections and signal separation. The few spikes are caused by the presence of some SM events with large weight at generation due to limited computing resources and are therefore purely statistical. The chargino sample contains 15362 signal events, 1997 events of neutralino pair background, 65 events of other SUSY backgrounds and 2980 events of SM background. Similarly the neutralino sample contains 1659 events of pure neutralino signal, 2395 events of chargino background, 9 events of other SUSY backgrounds and 865 events of SM background. All numbers and distributions are normalized to 500 fb^{-1} of integrated luminosity. The uncertainty on the cross-section measurement can be estimated as:

$$\Delta\sigma = \frac{\sqrt{S+B}}{S}, \tag{4.16}$$

where S stands for the number of pure signal, and B stands for the number of all background events identified as signal. The uncertainty on the cross section measurement for chargino and neutralino pair production with all hadronic final states is 0.9% and 4.2% respectively neglecting the uncertainty on the efficiencies and any systematic errors. In summary, the cross-sections are measured to be:

$$\sigma(e^+e^- \to \tilde{\chi}_1^+\tilde{\chi}_1^- \to \tilde{\chi}_1^0\tilde{\chi}_1^0 W^+W^- \to \tilde{\chi}_1^0\tilde{\chi}_1^0 q\bar{q}q\bar{q}) = 57.1 \pm 0.5\text{fb}$$

$$\sigma(e^+e^- \to \tilde{\chi}_2^0\tilde{\chi}_2^0 \to \tilde{\chi}_1^0\tilde{\chi}_1^0 ZZ \to \tilde{\chi}_1^0\tilde{\chi}_1^0 q\bar{q}q\bar{q}) = 11.0 \pm 0.5\text{fb}$$

Note that the cross-sections are dependent on the chargino and neutralino masses.

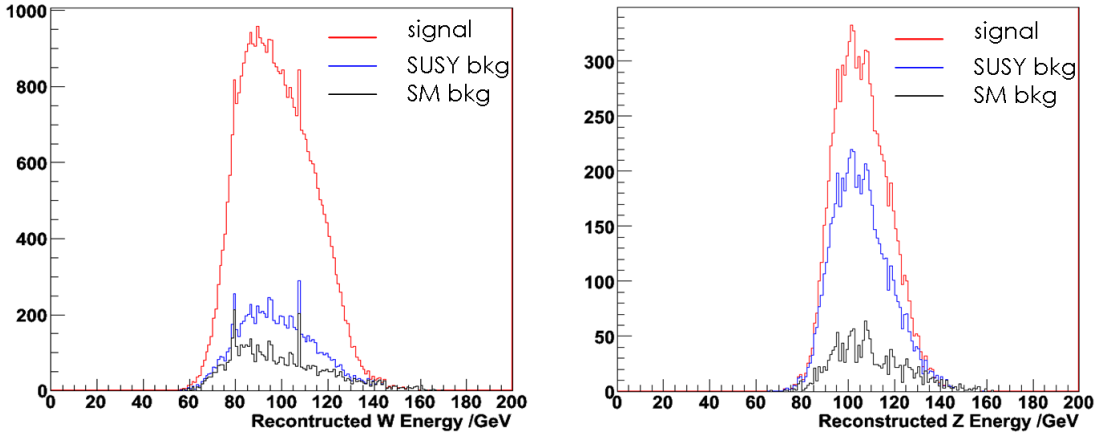

Figure 4.12: The inclusive histogram of reconstructed W energy for $\tilde{\chi}_1^+\tilde{\chi}_1^-$ selection (left) and Z energy for $\tilde{\chi}_2^0\tilde{\chi}_2^0$ selection (right).

4.5 Measurement of Chargino and Neutralino Masses

In the rest frame of $\tilde{\chi}_1^\pm$ or $\tilde{\chi}_2^0$ the energy of the W or Z is monochromatic because it is a two-body decay, and the energy $E_{W/Z}$ is:

$$E_{W/Z} = \frac{M^2_{\tilde{\chi}_1^\pm/\tilde{\chi}_2^0} + M^2_{W/Z} - M^2_{\tilde{\chi}_1^0}}{2M_{W/Z}} \tag{4.17}$$

In the lab frame $\tilde{\chi}_1^\pm$ or $\tilde{\chi}_2^0$ is boosted but the upper and lower edges of the energy distribution of the W or Z bosons still have well-defined values determined by $m_{\tilde{\chi}_1^\pm}$, $m_{\tilde{\chi}_1^0}$ and $m_{\tilde{\chi}_2^0}$. The masses can be determined by comparing the data to Monte-Carlo templates for different masses. The sensitivity of the method is studied in detail in this section.

4.5.1 Template Fitting

The determination of the masses can be explained using the example of the $\tilde{\chi}_1^+\tilde{\chi}_1^-$ process. The W energy distribution is shown in Figure 4.13 for different $\tilde{\chi}_1^0$ masses. All of them have been normalized to the same cross section to explore the purely kinematic effects on the shape of the distribution. The change of upper and lower edges of the spectrum after normalization is clearly visible, proving the sensitivity of this method. Assuming that we can generate a sufficient number of templates, the SUSY particle masses can be obtained by

comparing the boson energy spectrum from the "data" with those of various templates.

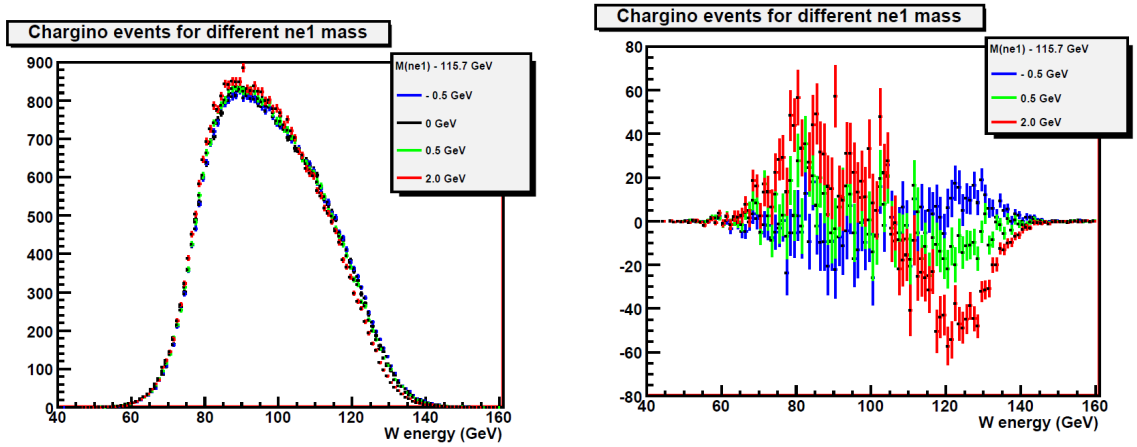

(a) (b)

Figure 4.13: (a)W energy distribution normalized to the same cross-section; (b) Difference of the normalized W energy spectrum with respect to the standard template ($M_{\tilde{\chi}_1^0} = 115.7\text{GeV}$).

In this analysis, one "data" sample is taken from the standard template (as in Table 4.2) without the SM background. The χ^2 of a template with respect to the "data" is defined as following:

$$\chi^2 = \sum_{i=0}^{Nbins} \frac{(y_{template,i} - y_{data,i} + \delta_i)^2}{\sigma^2_{template,i} + \sigma^2_{data,i} + \sigma^2_{SM,i}} \tag{4.18}$$

where $y_{...i}$ denotes the content of the ith bin in the boson energy histogram. The δ_i term is added as a Gaussian smearing of the central value of $y_{template,i} - y_{data,i}$ to take the effect of the SM background into account, with the Gaussian sigma equal to the uncertainty of the ith bin of the SM background.

The χ^2 dependence on the mass is parabolic. By comparing the "data" with various templates a series of χ^2 values can be calculated, and a parabola can be fitted. The minimum position corresponds to the actual mass. The half-width of the $\chi^2 = \chi^2_{min} + 1$ gives one σ uncertainty on the mass [118]. The statistics of the templates are much larger ($\sim$ 10 times) than the "data". It has been checked that the uncertainty results are stable for different binning of the histogram, and the minimum (χ^2_{min}/degree of freedom) is close to one.

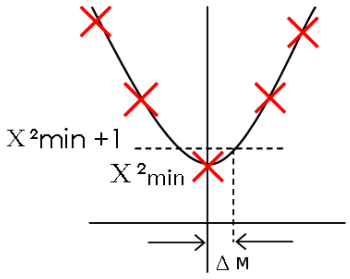

Figure 4.14: Sketch of template fitting method (not to scale).

4.5.2 Toy Monte-Carlo Study

The feasibility of the template fitting method was demonstrated by a toy Monte-Carlo simulation. Here the problem is simplified by replacing the complicated energy distribution with a Gaussian distribution. A Gaussian distribution with mean value 80 and σ 10 is generated as the "data" sample. The σ is taken as known and the mean value M is to be estimated. In order to do so, a series of "template" Monte-Carlos with mean values at 78, 79, 80, 81 and 82 are generated. The χ^2 value between data and each template is calculated as:

$$\chi^2 = \sum_{i=0}^{Nbins} \frac{(y_{template,i} - y_{data,i})^2}{\sigma^2_{template,i} + \sigma^2_{data,i}} \tag{4.19}$$

where $y_{template,i}$ and $y_{data,i}$ denote the content of the ith bin of the histogram. $\sigma^2_{template,i}$ and $\sigma^2_{data,i}$ are estimated for each bin assuming the Poisson distribution. The χ^2 as a function of the m value can be fitted with a parabola as in Figure 4.14. The true value of M can be estimated where the parabola reaches a minimum at χ^2_{min}. Its uncertainty ΔM is estimated as the interval where χ^2_{min} increases to $\chi^2_{min} + 1$.

Such process is repeated 1000 times and the distribution of estimated M and ΔM are shown in Figure 4.15. The central value in Figure 4.15(a) is 80.00 consistent with that used for the Monte-Carlo generation. The Root Mean Square (RMS) of the M distribution is 0.1145, consistent with the central value 0.1135 of ΔM distribution in Figure 4.15(b). This shows the method of estimating the parameter and its uncertainty is valid, and it does not introduce any bias in the measurement.

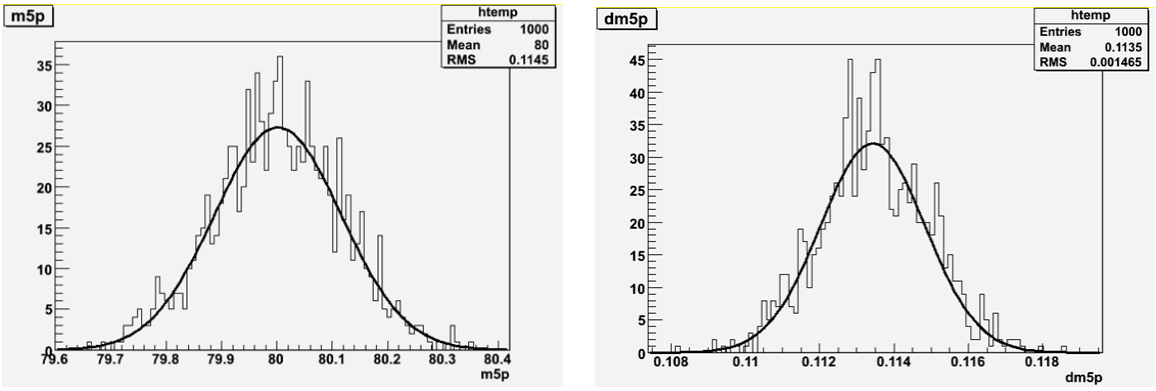

(a) (b)

Figure 4.15: (a) Mean value M given by the minimum position of the χ^2 parabola. (b) ΔM at which $\chi^2 = \chi^2_{min} + 1$.

4.5.3 Mass Uncertainty Result

As shown in Figure 4.16, the edge of the W energy distribution changes with respect to the mass of $\tilde{\chi}_1^{\pm}$ and $\tilde{\chi}_1^0$, therefore their masses can be obtained based on the W energy distribution using the template fitting method. Similarly, the masses of $\tilde{\chi}_2^0$ and $\tilde{\chi}_1^0$ can be obtained from the energy distribution of the Z boson. Note that the lower edge of the distributions is determined by the W or Z boson mass and is not sensitive to the mass of $\tilde{\chi}_1^{\pm}$ or $\tilde{\chi}_1^0$.

Figure 4.17 shows the χ^2 parabola fit obtained from the W energy spectrum, varying the $\tilde{\chi}_1^{\pm}$ and $\tilde{\chi}_1^0$ masses respectively. It should be noted that the point for $\Delta M = 0$ is calculated for an independent template different from the "data" sample. Similarly for the $\tilde{\chi}_2^0\tilde{\chi}_2^0$ events the χ^2 parabola can be obtained from the Z energy spectrum for various $\tilde{\chi}_2^0$ and $\tilde{\chi}_1^0$ masses (Figure 4.18). ΔM has the the value of -0.5, 0, 0.5 and 2 GeV for all masses, and in addition 6 GeV only for $\tilde{\chi}_2^0$. This is because the $\tilde{\chi}_2^0\tilde{\chi}_2^0$ sample has a lower purity and fewer statistics compared to the $\tilde{\chi}_1^+\tilde{\chi}_1^-$ sample due to the small cross-section and a large background of the latter, and therefore the change in the Z energy edge is less sensitive to the $\tilde{\chi}_2^0$ mass. These figures are obtained with an energy bin width of 5 GeV.

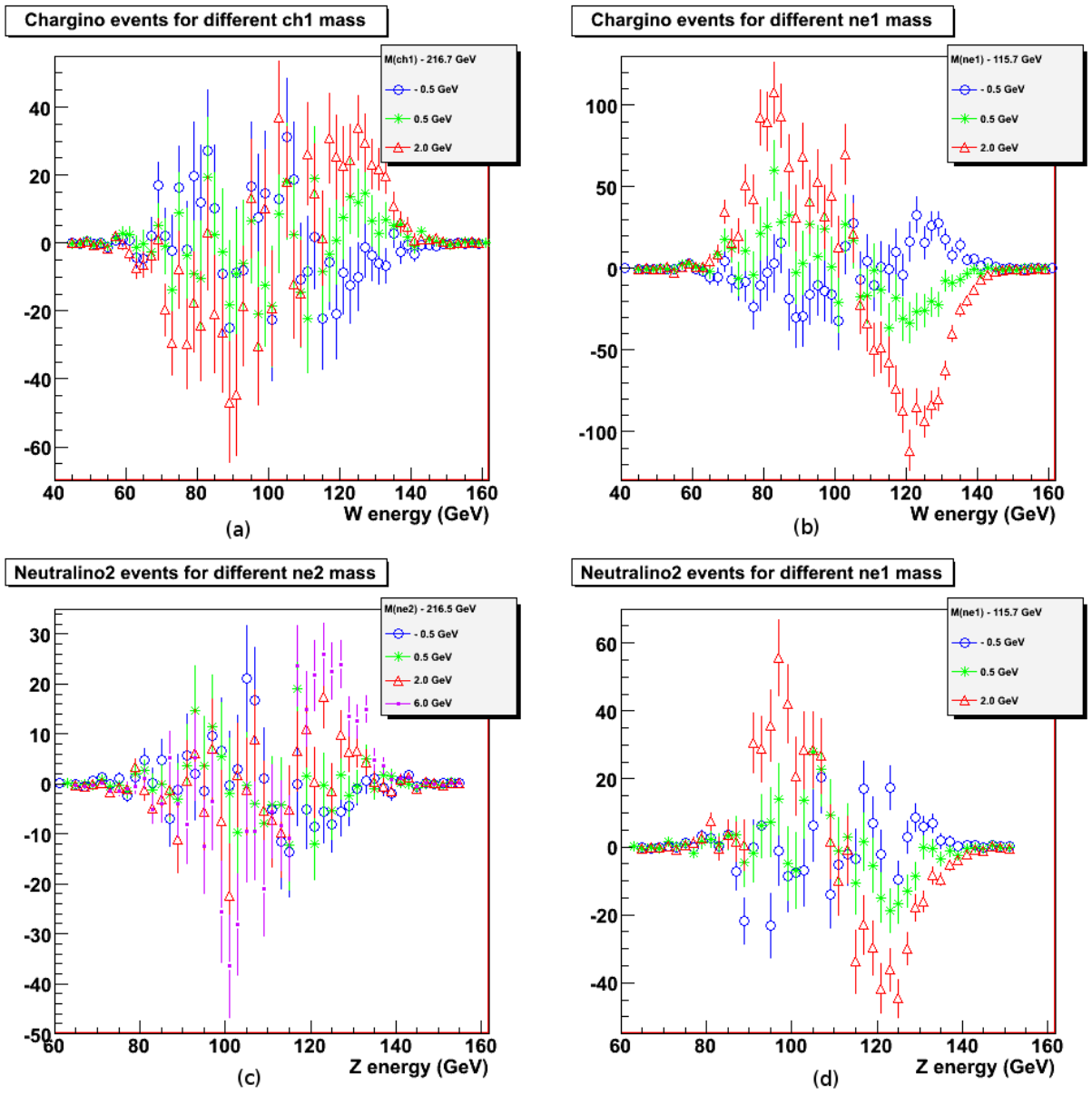

Figure 4.16: Change of the W or Z energy spectrum due to change of the SUSY particle masses. The bin width is 2 GeV. (a) Change of the W energy spectrum for various $\tilde{\chi}_1^{\pm}$ masses; (b) Change of the W energy spectrum for various $\tilde{\chi}_1^0$ masses; (c) Change of the Z energy spectrum for various $\tilde{\chi}_2^0$ masses; (d) Change of the Z energy spectrum for various $\tilde{\chi}_1^0$ masses.

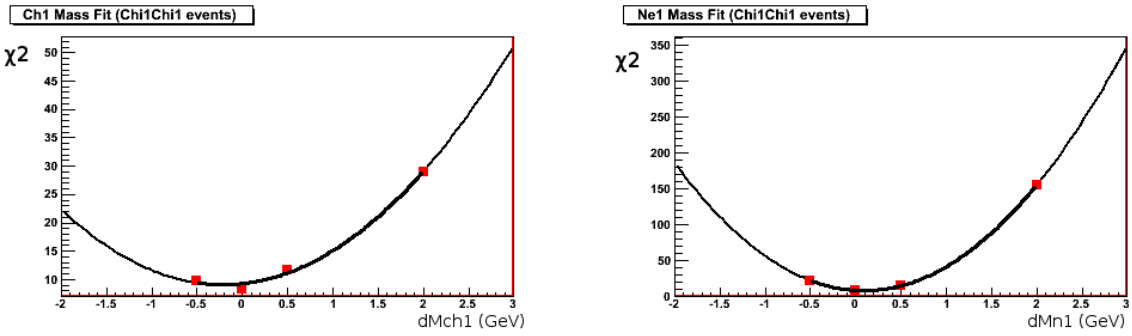

Figure 4.17: The χ^2 dependence on the shifted mass of $\tilde{\chi}_1^{\pm}$ (left) and $\tilde{\chi}_1^0$ (right), calculated for the $\tilde{\chi}_1^+\tilde{\chi}_1^-$ signal.

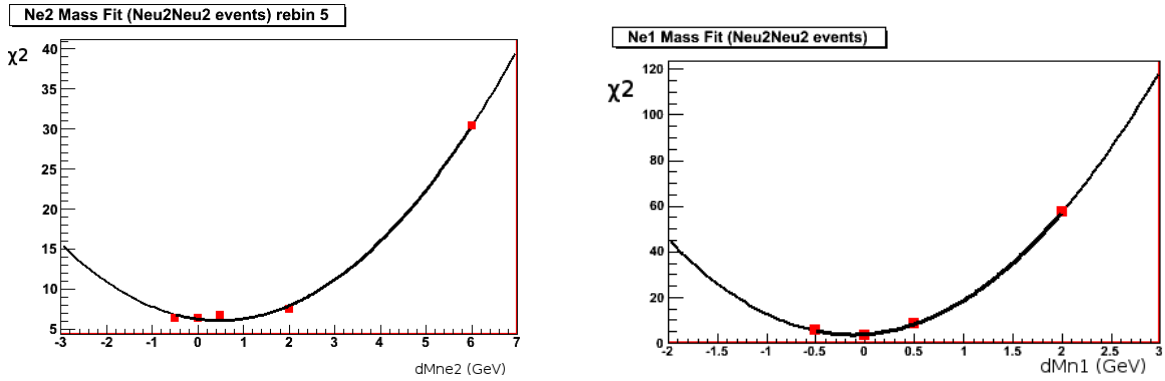

Figure 4.18: The χ^2 dependence on the shifted mass of $\tilde{\chi}_2^0$ (left) and $\tilde{\chi}_1^0$ (right), calculated for the $\tilde{\chi}_2^0\tilde{\chi}_2^0$ signal.

Some uncertainties of SUSY particle masses determined by the template fitting technique are given in Table 4.6. From the $\tilde{\chi}_1^+\tilde{\chi}_1^-$ signal, it is obtained that:

$$M_{\tilde{\chi}_1^{\pm}} = 216.2 \pm 0.5\text{GeV};$$
$$M_{\tilde{\chi}_1^0} = 115.77 \pm 0.16\text{GeV};$$

and from the $\tilde{\chi}_2^0\tilde{\chi}_2^0$ signal it is obtained that:

$$M_{\tilde{\chi}_2^0} = 217.8 \pm 1.0\text{GeV};$$
$$M_{\tilde{\chi}_1^0} = 115.6 \pm 0.3\text{GeV}.$$

These are consistent with the Monte-Carlo values ($M_{\tilde{\chi}_1^{\pm}} = 216.5\text{GeV}$, $M_{\tilde{\chi}_2^0} = 216.7\text{GeV}$, $M_{\tilde{\chi}_2^0} = 115.7\text{GeV}$).

The results are robust against different binning. The uncertainty is taken after averaging over results with different binning of energy histograms with 1 GeV, 2 GeV, 5 GeV or 10 GeV per bin.

$\tilde{\chi}_1^+\tilde{\chi}_1^-$					
$M_{\tilde{\chi}_1^\pm}$			$M_{\tilde{\chi}_1^0}$		
GeV/bin	ΔM/GeV	χ^2_{min} position/GeV	GeV/bin	ΔM/GeV	χ^2_{min} position/GeV
1	0.501	-0.667	1	0.155	0.053
2	0.462	-0.329	2	0.157	0.067
5	0.432	0.117	5	0.155	0.074
10	0.494	-0.208	10	0.157	0.092
Average	**0.472**	-0.271	Average	**0.156**	0.0715
$\tilde{\chi}_2^0\tilde{\chi}_2^0$					
$M_{\tilde{\chi}_2^0}$			$M_{\tilde{\chi}_1^0}$		
GeV/bin	ΔM/GeV	χ^2_{min} position/GeV	GeV/bin	ΔM/GeV	χ^2_{min} position/GeV
1	0.771	1.815	1	0.268	-0.026
2	0.859	1.436	2	0.280	-0.128
5	1.122	0.469	5	0.276	-0.054
10	1.149	0.535	10	0.290	-0.125
Average	**0.975**	1.064	Average	**0.279**	-0.083

Table 4.6: Mass uncertainty results. χ^2_{min} position stands for the distance of the position M where the minimum χ^2 is taken to M value of the standard template.

Each uncertainty was calculated by varying that specific mass alone, assuming other SUSY particle masses are measured perfectly. In order to estimate possible correlations between the mass uncertainties, several templates are needed with masses, e.g. $\tilde{\chi}_1^\pm$ and $\tilde{\chi}_1^0$, or $\tilde{\chi}_2^0$ and $\tilde{\chi}_1^0$, shifted simultaneously. This issue is not addressed in this study.

4.6 Conclusion and Discussion

Chargino and neutralino pair production at the ILC with full SiD detector simulation has been studied. The cross-sections of $\tilde{\chi}_1^+\tilde{\chi}_1^-$ and $\tilde{\chi}_2^0\tilde{\chi}_2^0$ have been determined with relative precision of 0.9% and 4.2%. The template fitting method is applied to determine the chargino

and neutralino masses, and the mass uncertainties obtained for $\tilde{\chi}_1^{\pm}$, $\tilde{\chi}_2^0$ and $\tilde{\chi}_1^0$ are 0.5, 0.16 and 1.0 GeV respectively. This study shows the physics potential of the ILC in understanding SUSY. In addition, the separation of the WW and ZZ final state demonstrates that the precision of the SiD detector with good PFA performance.

A similar analysis of the chargino and neutralino mass measurements was performed based on the ILD detector concept[119]. The masses were determined by fitting the shape of the W or Z energy distributions analytically, with the chargino and neutralino masses as fitting parameters. The masses of $\tilde{\chi}_1^{\pm}$, $\tilde{\chi}_2^0$ and $\tilde{\chi}_1^0$ could be determined with a precision of 2.9 GeV, 1.7 GeV and 1.0 GeV, respectively. It should be mentioned that these results cannot be compared directly with those presented in this chapter, since the correlations between the masses were automatically taken into consideration with the analytical method, while for the template fitting method the uncertainties were quoted as if other masses could be measured perfectly. Introducing the correlations into the template fitting method requires templates in which chargino and neutralino masses are varied simultaneously and this will be a valuable extension of the presented study.

Chapter 5

Summary

The International Linear Collider is a proposed electron-positron collider which enables precision measurements to test the Standard Model and new physics. This thesis presented the determination of the masses of chargino ($\tilde{\chi}_1^{\pm}$) and neutralinos ($\tilde{\chi}_1^0$, $\tilde{\chi}_2^0$) at the ILC based on full SiD detector simulation and realistic event reconstruction. The analysis has been performed using the fully hadronic channel of the processes $e^-e^+ \to \tilde{\chi}_1^+\tilde{\chi}_1^- \to \tilde{\chi}_1^0\tilde{\chi}_1^0 W^+W^-$ and $e^-e^+ \to \tilde{\chi}_2^0\tilde{\chi}_2^0 \to \tilde{\chi}_1^0\tilde{\chi}_1^0 ZZ$ at the centre-of-mass energy of 500 GeV for an integrated luminosity of 500 fb^{-1}. As one of the benchmarking processes, this does not only show the feasibility of measuring SUSY parameters with high precision at the ILC, but also test the overall detector performance. Good separation of the chargino and neutralino signals has been achieved by employing a PFA algorithm.

The template fitting method has been devised to determine the chargino and neutralino masses based on the energy distribution of their decay products, $W^{\pm}$ and Z, respectively. Its principle was proven by a toy Monte-Carlo study. The masses of the chargino and neutralino using the template fitting method are found to be 216.2 ± 0.5 GeV, 115.77 ± 0.16 GeV and 217.8 ± 1.0 GeV for $\tilde{\chi}_1^{\pm}$, $\tilde{\chi}_1^0$ and $\tilde{\chi}_2^0$, respectively, consistent with the Monte-Carlo values at generation.

The thesis has also presented a study of the ISIS2 sensor based on a novel technology developed for the ILC vertex detector. Tests have been performed on the test structure

and pixels in the main array, which demonstrated the sensor's capability of charge storage and transfer. The fringing effect and slow readout have been observed and interpreted. The charge calibration has been performed using a ^{55}Fe source. The well capacity of the summing gate has been measured under various biases. The operation conditions have been optimized and established using charge injection. The charge transfer efficiency in the pixel has been measured with two independent methods, giving consistent values of $98.9 \pm 0.4\%$ and $98.4 \pm 0.3\%$. The ISIS2 testing results show a successful implementation of CCD registers on a CMOS process, and guide the way to a future iteration of ISIS sensors, which could potentially be directly applicable to the ILC vertex detector.

Bibliography

[1] K Nakamura et al. *J. Phys.*, **G37** (2010) 075021.

[2] Steven Weinberg. *Phys. Rev. Lett.*, **19**, 21 (1967) 1264–1266.

[3] Sheldon L. Glashow. *Nuclear Physics*, **22**, 4 (1961) 579 – 588. ISSN 0029-5582.

[4] ALEPH Collaboration, DELPHI Collaboration, L3 Collaboration, OPAL Collaboration & The LEP Working Group for Higgs Boson Searches. *Physics Letters B*, **565** (2003) 61 – 75. ISSN 0370-2693.

[5] Nicola Cabibbo. *Phys. Rev. Lett.*, **10**, 12 (1963) 531–533.

[6] Makoto Kobayashi & Toshihide Maskawa. *Progress of Theoretical Physics*, **49**, 2 (1973) 652–657. `http://ptp.ipap.jp/link?PTP/49/652/`

[7] Steven Weinberg. *Phys. Rev. D*, **13**, 4 (1976) 974–996.

[8] S. Weinberg. *Phys. Rev. D*, **19**, 4 (1979) 1277–1280.

[9] Eldad Gildener. *Phys. Rev. D*, **14**, 6 (1976) 1667–1672.

[10] V. C. Rubin, W. K. J. Ford & N. . Thonnard. *Astrophysical Journal*, **238** (1980) 471–487.

[11] D. Clowe, M. Bradač, A. H. Gonzalez, M. Markevitch, S. W. Randall, C. Jones & D. Zaritsky. *Astrophysical Journal Letters*, **648** (2006) L109–L113.

[12] R. Massey, J. Rhodes, R. Ellis, N. Scoville, A. Leauthaud, A. Finoguenov, P. Capak, D. Bacon, H. Aussel, J.-P. Kneib, A. Koekemoer, H. McCracken, B. Mobasher, S. Pires, A. Refregier, S. Sasaki, J.-L. Starck, Y. Taniguchi, A. Taylor & J. Taylor. *Nature*, **445** (2007) 286–290.

[13] Hironari Miyazawa. *Phys. Rev.*, **170**, 5 (1968) 1586–1590.

[14] Stephen P. Martin. `arXiv:hep-ph/9709356`

[15] Utpal Chattopadhyay, Achille Corsetti & Pran Nath. *Phys. Rev. D*, **68**, 3 (2003) 035005.

[16] F. Gabbiani, E. Gabrielli, A. Masiero & L. Silvestrini. *Nuclear Physics B*, **477**, 2 (1996) 321 – 352. ISSN 0550-3213.

[17] M.J. Ramsey-Musolf & S. Su. *Physics Reports*, **456**, 1-2 (2008) 1 – 88. ISSN 0370-1573.

[18] G. L. Kane, Chris Kolda, Leszek Roszkowski & James D. Wells. *Phys. Rev. D*, **49**, 11 (1994) 6173–6210.

[19] A. H. Chamseddine, R. Arnowitt & Pran Nath. *Phys. Rev. Lett.*, **49**, 14 (1982) 970–974.

[20] R. Barbieri, S. Ferrara & C.A. Savoy. *Physics Letters B*, **119**, 4-6 (1982) 343 – 347. ISSN 0370-2693.

[21] Lawrence Hall, Joe Lykken & Steven Weinberg. *Phys. Rev. D*, **27**, 10 (1983) 2359–2378.

[22] Curtis G. Callan. *Phys. Rev. D*, **2**, 8 (1970) 1541–1547.

[23] K. Symanzik. *Communications in Mathematical Physics*, **18** (1970) 227–246. ISSN 0010-3616. 10.1007/BF01649434. http://dx.doi.org/10.1007/BF01649434

[24] A. De Roeck, J. Ellis, F. Gianotti, F. Moortgat, K.A. Olive & L. Pape. *The European Physical Journal C - Particles and Fields*, **49** (2007) 1041–1066. ISSN 1434-6044. 10.1140/epjc/s10052-006-0182-6. http://dx.doi.org/10.1140/epjc/s10052-006-0182-6

[25] John Ellis, J. S. Hagelin, D. V. Nanopoulos, K. Olive & M. Srednicki. *Nuclear Physics B*, **238**, 2 (1984) 453 – 476. ISSN 0550-3213. http://www.sciencedirect.com/science/article/B6TVC-473DP1S-15R/2/79605887f96af5

[26] M. Battaglia et al. arXiv:hep-ex/0603010.

[27] W. Oller, H. Eberl & W. Majerotto. *Phys. Rev.*, **D71** (2005) 115002.

[28] S.Y. Choi, A. Djouadi, M. Guchait, J. Kalinowski, H.S. Song & P.M. Zerwas. *The European Physical Journal C - Particles and Fields*, **14** (2000) 535–546. ISSN 1434-6044. http://dx.doi.org/10.1007/s100520000365

[29] S. Y. Choi, M. Guchait, J. Kalinowski & P. M. Zerwas. *Physics Letters B*, **479**, 1-3 (2000) 235 – 244. ISSN 0370-2693.

[30] S. Y. Choi, J. Kalinowski, Gudrid A. Moortgat-Pick & P. M. Zerwas. *Eur. Phys. J.*, **C22** (2001) 563–579.

[31] Howard E. Haber & Gordon L. Kane. *Phys. Rept.*, **117** (1985) 75–263.

[32] "LHC experiment". http://lhc.web.cern.ch/lhc/

[33] "LEP experiment". http://delphiwww.cern.ch/offline/lepwgs.html

[34] A. Djouadi, J. Lykken, K. Mönig, Y. Okada, M. Oreglia & S. Yamashita. "International Linear Collider Reference Design Report Volume 2: PHYSICS AT THE ILC" (2007). arXiv:0709.1893

[35] Nima Arkani-Hamed, Savas Dimopoulos & Gia Dvali. *Physics Letters B*, **429**, 3-4 (1998) 263 – 272. ISSN 0370-2693.

[36] H. Davoudiasl, J. L. Hewett & T. G. Rizzo. *Phys. Rev. D*, **63**, 7 (2001) 075004.

[37] "SLAC Linear Collider". http://www2.slac.stanford.edu/vvc/experiments/slc.html

[38] N. Walker et al. J. Brau, Y. Okada. "International Linear Collider Reference Design Report. Volume 1: Executive Summary." arXiv:0712.1950.

[39] R. Alley, H. Aoyagi, J. Clendenin, J. Frisch, C. Garden, E. Hoyt, R. Kirby, L. Klaisner, A. Kulikov, R. Miller, G. Mulhollan, C. Prescott, P. Sáez, D. Schultz, H. Tang, J. Turner, K. Witte, M. Woods, A. D. Yeremian & M. Zolotorev. *Nuclear Instruments and Methods in Physics Research Section A: Accelerators, Spectrometers, Detectors and Associated Equipment*, **365**, 1 (1995) 1 – 27. ISSN 0168-9002.

[40] C. K. Sinclair, P. A. Adderley, B. M. Dunham, J. C. Hansknecht, P. Hartmann, M. Poelker, J. S. Price, P. M. Rutt, W. J. Schneider & M. Steigerwald. *Phys. Rev. ST Accel. Beams*, **10**, 2 (2007) 023501.

[41] Haakon Olsen & L. C. Maximon. *Phys. Rev.*, **114**, 3 (1959) 887–904.

[42] F. Furuta, K. Saito, T. Saeki, H. Inoue, Y. Morozumi, T. Higo, Y. Higashi, H. Matsumoto, S. Kazakov, H. Yamaoka, K. Ueno, Y. Kobayashi, R. S. Orr & J. Sekutowicz. "Experimental Comparison at KEK of High Gradient Performance of Different Single Cell Superconducting Cavity Desings". In "Proceedings of EPAC 2006", (2006).

[43] R. L. Geng, G. V. Eremeev, H. Padamsee & V. D. Shemelin. "High-gradient Activities at Cornell: Re-entrant Cavities". In "Proceedings of PAC07", (2007).

[44] ILC Global Design Effort. "SB2009 Proposal Document". http://ilc-edmsdirect.desy.de/ilc-edmsdirect/file.jsp?edmsid=D00000000900425

[45] James E. Brau, Martin Breidenbach, Charles Baltay, Raymond E. Frey & David M. Strom. *Nucl. Instrum. Meth.*, **A579** (2007) 567–571.

[46] SiD Collaboration. "SiD Detector Outline Document". http://hep.uchicago.edu/∼oreglia/siddod.pdf

[47] M.J. Charles et al. "The SiD Particle Flow Algorithm, SiD Letter of Intent (Appendices)". https://silicondetector.org/display/SiD/LOI.

[48] SiD Collaboration. "SiD Letter of Intent". https://silicondetector.org/display/SiD/LOI.

[49] R. Frey, J. Brau, M. Breidenbach, D. Freytag, G. Haller, R. Herbst, R. Lander, T. Nelson, V. Radeka, D. Strom & M. Tripathi. "A Silicon-Tungsten ECal with Integrated Electronics" (2007). arXiv:0710.2373

[50] N Watson, J Ballin, J Crooks, P Dauncey, A-M Magnan, Y Mikami, O Miller, M Noy, M Stanitzki, K Stefanov, R Turchetta, M Tyndel, V Rajovic, E Villani & J Wilson. *Journal of Physics: Conference Series*, **110**, 9 (2008) 092035. http://stacks.iop.org/1742-6596/110/i=9/a=092035

[51] Jamie Alexander Ballin, Jamie Phillip Crooks, Paul Dominic Dauncey, Anne-Marie Magnan, Yoshiari Mikami, Owen Daniel Miller, Matthew Noy, Vladimir Rajovic, Marcel Stanitzki, Konstantin Stefanov, Renato Turchetta, Mike Tyndel, Enrico Giulio Villani, Nigel Keith Watson & John Allan Wilson. *Sensors*, **8**, 9 (2008) 5336–5351. ISSN 1424-8220. http://www.mdpi.com/1424-8220/8/9/5336/

[52] B Bilki, J Butler, T Cundiff, G Drake, W Haberichter, E Hazen, J Hoff, S Holm, A Kreps, E May, G Mavromanolakis, E Norbeck, D Northacker, Y Onel, J Repond, D Underwood, S Wu & L Xia. *Journal of Instrumentation*, **3**, 05 (2008) P05001. http://stacks.iop.org/1748-0221/3/i=05/a=P05001

[53] Andy White. "Gas Electron Multiplier Technology for Digital Hadron Calorimetry". "www-hep.uta.edu/ white/SiD/LOI/GEM_DHCAL_FNAL_092205.ppt"

[54] Y. Giomataris, Ph. Rebourgeard, J. P. Robert & G. Charpak. *Nuclear Instruments and Methods in Physics Research Section A: Accelerators, Spectrometers, Detectors and Associated Equipment*, **376**, 1 (1996) 29 – 35. ISSN 0168-9002.

[55] P. Buzhan, B. Dolgoshein, L. Filatov, A. Ilyin, V. Kantzerov, V. Kaplin, A. Karakash, F. Kayumov, S. Klemin, E. Popova & S. Smirnov. *Nuclear Instruments and Methods in Physics Research Section A: Accelerators, Spectrometers, Detectors and Associated Equipment*, **504**, 1-3 (2003) 48 – 52. ISSN 0168-9002. Proceedings of the 3rd International Conference on New Developments in Photodetection.

[56] CALICE collaboration. *Nuclear Instruments and Methods in Physics Research Section A: Accelerators, Spectrometers, Detectors and Associated Equipment*, **581**, 1-2 (2007) 451 – 456. ISSN 0168-9002. VCI 2007 - Proceedings of the 11th International Vienna Conference on Instrumentation.

[57] Richard Smith & R. Wands. In the Proceedings of 2005 International Linear Collider Workshop (LCWS 2005), Stanford, California, 18-22 Mar 2005.

[58] A. Yamamoto & Y. Makida. *Nucl. Instrum. Meth.*, **A494** (2002) 255–265.

[59] Brett Parker & Andrei Seryi. *Phys. Rev. ST Accel. Beams*, **8** (2005) 041001.

[60] "BaBar Detector". http://www.slac.stanford.edu/BF/

[61] "BELLE Detector". http://belle.kek.jp/

[62] "ATLAS Detector". http://www.atlas.ch/detector.html

[63] "CMS Detector". http://cms.web.cern.ch/cms/Detector/index.html

[64] H.R. Band. "RPC/KPiX Studies for Use in Linear Collider Detectors". http://silicondetector.org/download/attachments/37323762/RPC_Wisc.pdf

[65] C. Lu, K. McDonald, A. J. S. Smith & J. Zhang. arXiv:1006.1061

[66] "MINOS Experiment". http://www-numi.fnal.gov/

[67] Paul et al Karchin. "Scintillator Based Muon System and Tail-Catcher R&D". http://silicondetector.org/download/attachments/37323762/ILC_Muon_2009_proposal

[68] A. Rosca. *Nuclear Physics B - Proceedings Supplements*, **197**, 1 (2009) 337 – 341. 11th Topical Seminar on Innovative Particle and Radiation Detectors (IPRD08).

[69] The ILD Concept Group. arXiv:1006.3396

[70] B. Parker, A. Mikhailichenko, K. Buesser, J. Hauptman, T. Tauchi, P. Burrows, T. Markiewicz, M. Oriunno & A. Seryi. *ILC-NOTE-2009-050*.

[71] C.J.S. Damerell. "Vertex Detectors: The State of Art and Future Prospects". In "Proceedings of the 1995 SLAC Sumemr Institute on Particle Physics: The Top Quark and the Electroweak Interaction", (1995).

[72] John R. Woodyard. U.S. Patent: 2530110.

[73] H. Spieler. "Semiconductor Detector Systems". Oxford University Press (2005).

[74] W.S. Boyle G.E. Smith. *Bell System Technical Journal*, **49**, 587.

[75] C.J.S. Damerell et al. *Nuclear Instruments and Methods*, **185**, 33.

[76] J. R. Janesick. "Scientific Charge-Coupled Devices". SPIE Press (2000).

[77] "SLAC Large Detector". http://www2.slac.stanford.edu/vvc/detectors/sld.html

[78] Y. Banda, P. Coulter, D. Cussans, C. Damerell, E. Devetak, J. Fopma, B. Foster, R. Frost, R. Gao, J. Goldstein, T. Greenshaw, K. Harder, B. Hawes, S. Hillert, B. Jeffery, J.J. John, N. Kundu, Y. Li, P. Murray, A. Nomerotski, C. Perry, K. Stefanov, S. Thomas, J. Velthuis, T. Wolliscroft, S. Worm, J. Yow & Z. Zhang. *Nuclear Instruments and Methods in Physics Research Section A: Accelerators, Spectrometers, Detectors and Associated Equipment*, **621**, 1-3 (2010) 192 – 204.

[79] K. D. Stefanov. *Nucl. Instrum. Meth.*, **A569** (2006) 48–52.

[80] Erik Devetak. "Measurement of the Top Quark Mass, Cross Section and Anomalous Couplings at the International Linear Collider" (2009). D.Phil. thesis, University of Oxford.

[81] Yambazi Banda. "Determination of the Higgs Boson Branching Ratio at the International Linear Collider" (2010). D.Phil. thesis, University of Oxford.

[82] R. Turchetta et al. *Nucl. Instrum. Meth.*, **A458** (2001) 677–689.

[83] G. Deptuch et al. *IEEE Trans. Nucl. Sci.*, **51** (2004) 2313.

[84] P. Fischer et al. *Nucl. Instrum. Meth.*, **A582** (2007) 843–848.

[85] R. Turchetta, W. Gannon & A. Evans. Presented at the IEEE Workshop on Charge-Coupled Devices and Advanced Image Sensors, Schloss Elmau, Germany, May 2003.

[86] Konstantin D. Stefanov. *Nuclear Instruments and Methods in Physics Research Section A: Accelerators, Spectrometers, Detectors and Associated Equipment*, **569**, 1 (2006) 48 – 52. ISSN 0168-9002. Proceedings of the 14th International Workshop on Vertex Detectors - VERTEX 2005, 14th International Workshop on Vertex Detectors.

[87] "e2v". `http://www.e2v.com.`

[88] J.J. Velthuis et al. *Nuclear Instruments and Methods in Physics Research A*, **599** (2009) 161.

[89] D. Cussans et al. *Nuclear Instruments and Methods in Physics Research A*, **604** (2009) 393.

[90] Z. Zhang et al. *Nuclear Instruments and Methods in Physics Research A*, **607** (2009) 538.

[91] "EUDET". `http://www.eudet.org/.`

[92] R. Turchetta. *Nuclear Instruments and Methods in Physics Research Section A: Accelerators, Spectrometers, Detectors and Associated Equipment*, **335**, 1-2 (1993) 44 – 58. ISSN 0168-9002.

[93] "TowerJazz Company". `http://www.towerjazz.com.`

[94] "ISIS2 Design Documentation". Internal note.

[95] C. Damerell, Z. Zhang, R. Gao, Jaya John John, Y. Li, A. Nomerotski, A. Holland, G. Seabroke, M. Havranek, K. Stefanov, A. Kar-Roy, R. Bell, D. Burt & P. Pool. *Nuclear Instruments and Methods in Physics Research Section A: Accelerators, Spectrometers, Detectors and Associated Equipment*, **624**, 2 (2010) 465 – 469. ISSN 0168-9002. New Developments in Radiation Detectors - Proceedings of the 11th European Symposium on Semiconductor Detectors.

[96] "Linear Collider Flavour Identification". `http://heplocal.rl.ac.uk/lcfi/`

[97] "LabVIEW software". `http://www.ni.com/labview/`

[98] Zhige Zhang et al. "In-situ Storage Image Sensor for a Vertex Detector at the ILC". In "Proceedings of VERTEX 2009", (2009).

[99] "Uniblitz shutters". `http://www.uniblitz.com/`

[100] "SCHOTT light source". `http://www.schott.com/lightingimaging/`

[101] Wolfgang Kilian, Thorsten Ohl & Jurgen Reuter. `arXiv:0708.4233`

[102] Torbjorn Sjostrand, Stephen Mrenna & Peter Z. Skands. *JHEP*, **05** (2006) 026. arXiv:hep-ph/0603175

[103] S. Agostinelli et al. *Nucl. Instrum. Meth.*, **A506** (2003) 250–303.

[104] John Allison et al. *IEEE Trans. Nucl. Sci.*, **53** (2006) 270.

[105] N. Graf & J. McCormick. *AIP Conf. Proc.*, **867** (2006) 503–512.

[106] "sid02". http://lcsim.org/detectors/#sid02

[107] Frank Gaede, Ties Behnke, Norman Graf & Tony Johnson. arXiv:physics/0306114

[108] "lcsim". http://www.lcsim.org/.

[109] O. Wendt, F. Gaede & T. Krämer. *Pramana*, **69**.

[110] M.J. Charles, U. Mallik & T.J. Kim. arXiv:0901.4532

[111] M.J. Charles. arXiv:0901.4670

[112] Yamashita Satoru (1998). OPAL Techinical Note TN579.

[113] S. Catani, Yuri L. Dokshitzer, M. Olsson, G. Turnock & B. R. Webber. *Phys. Lett.*, **B269** (1991) 432–438.

[114] S. Bethke, Z. Kunszt, D. E. Soper & W. J. Stirling. *Nuclear Physics B*, **370**, 2 (1992) 310 – 334. ISSN 0550-3213.

[115] H1 Collaboration. arXiv:hep-ex/9706002

[116] B. List & J. List. "MarlinKinfit: An Object - Oriented Kinematic Fitting Package".

[117] Ron Cassell. arXiv:0902.2694

[118] L. Lyons. "Statistics for Nuclear and Particle Physicists". Cambridge University Press (1989).

[119] T. Suehara & J. List. arXiv:0906.5508